Potent human broadly SARS-CoV-2–neutralizing IgA and IgG antibodies effective against Omicron BA.1 and BA.2

Cyril Planchais, Ignacio Fernández, Timothée Bruel, Guilherme Dias de Melo, Matthieu Prot, Maxime Beretta, Pablo Guardado-Calvo, Jérémy Dufloo, Luis M Molinos-Albert, Marija Backovic, et al.

JEM Journal of Experimental Medicine

ARTICLE

Potent human broadly SARS-CoV-2–neutralizing IgA and IgG antibodies effective against Omicron BA.1 and BA.2

Cyril Planchais[1,2], Ignacio Fernández[3,4], Timothée Bruel[4,5*], Guilherme Dias de Melo[6*], Matthieu Prot[7*], Maxime Beretta[1,2], Pablo Guardado-Calvo[3,4], Jérémy Dufloo[4,5], Luis M. Molinos-Albert[1,2], Marija Backovic[3,4], Jeanne Chiaravalli[8], Emilie Giraud[8], Benjamin Vesin[9,10], Laurine Conquet[11], Ludivine Grzelak[4,5], Delphine Planas[4,5], Isabelle Staropoli[4,5], Florence Guivel-Benhassine[4,5], Thierry Hieu[12], Mikaël Boullé[8], Minerva Cervantes-Gonzalez[13], Marie-Noëlle Ungeheuer[14], Pierre Charneau[9,10], Sylvie van der Werf[4,15,16], Fabrice Agou[8], French COVID Cohort Study Group, CORSER Study Group, Jordan D. Dimitrov[17], Etienne Simon-Lorière[7**], Hervé Bourhy[6**], Xavier Montagutelli[11**], Félix A. Rey[3,4**], Olivier Schwartz[4,5**], and Hugo Mouquet[1,2]

Memory B-cell and antibody responses to the SARS-CoV-2 spike protein contribute to long-term immune protection against severe COVID-19, which can also be prevented by antibody-based interventions. Here, wide SARS-CoV-2 immunoprofiling in Wuhan COVID-19 convalescents combining serological, cellular, and monoclonal antibody explorations revealed humoral immunity coordination. Detailed characterization of a hundred SARS-CoV-2 spike memory B-cell monoclonal antibodies uncovered diversity in their repertoire and antiviral functions. The latter were influenced by the targeted spike region with strong Fc-dependent effectors to the S2 subunit and potent neutralizers to the receptor-binding domain. Amongst those, Cv2.1169 and Cv2.3194 antibodies cross-neutralized SARS-CoV-2 variants of concern, including Omicron BA.1 and BA.2. Cv2.1169, isolated from a mucosa-derived IgA memory B cell demonstrated potency boost as IgA dimers and therapeutic efficacy as IgG antibodies in animal models. Structural data provided mechanistic clues to Cv2.1169 potency and breadth. Thus, potent broadly neutralizing IgA antibodies elicited in mucosal tissues can stem SARS-CoV-2 infection, and Cv2.1169 and Cv2.3194 are prime candidates for COVID-19 prevention and treatment.

Introduction

The coronavirus disease 2019 (COVID-19) is caused by the severe acute respiratory syndrome coronavirus 2 (SARS-CoV-2) and accounts to date for nearly 530 million infection cases and 6.3 million deaths worldwide (WHO, 2022). SARS-CoV-2 infects

[1]Institut Pasteur, Université Paris Cité, Laboratory of Humoral Immunology, Paris, France; [2]INSERM U1222, Paris, France; [3]Institut Pasteur, Université Paris Cité, Structural Virology Unit, Paris, France; [4]CNRS UMR3569, Paris, France; [5]Institut Pasteur, Université Paris Cité, Virus & Immunity Unit, Paris, France; [6]Institut Pasteur, Université Paris Cité, Lyssavirus Epidemiology and Neuropathology Unit, Paris, France; [7]Institut Pasteur, Université Paris Cité, G5 Evolutionary Genomics of RNA Viruses, Paris, France; [8]Institut Pasteur, Université Paris Cité, Chemogenomic and Biological Screening Core Facility, C2RT, Paris, France; [9]Pasteur-TheraVectys, Paris, France; [10]Institut Pasteur, Université Paris Cité, Molecular Virology & Vaccinology Unit, Paris, France; [11]Institut Pasteur, Université Paris Cité, Mouse Genetics Laboratory, Paris, France; [12]Institut Pasteur, Université Paris Cité, Functional Genetics of Infectious Diseases Unit, Paris, France; [13]Department of Epidemiology, Biostatistics and Clinical Research, Assistance Publique-Hôpitaux de Paris, Bichat Claude Bernard University Hospital, INSERM CIC-EC 1425, Paris, France; [14]Institut Pasteur, Université Paris Cité, Investigation Clinique et Accès aux Ressources Biologiques, Center for Translational Research, Paris, France; [15]Institut Pasteur, Université Paris Cité, Molecular Genetics of RNA Viruses, Paris, France; [16]Université de Paris, Paris, France; [17]Centre de Recherche des Cordeliers, INSERM, Sorbonne Université, Université de Paris, Paris, France.

*T. Bruel, G.D. de Melo, and M. Prot contributed equally to this paper; **E. Simon-Lorière, H. Bourhy, X.Montagutelli, F.A. Rey, and O. Schwartz contributed equally to this paper. Correspondence to Hugo Mouquet: hugo.mouquet@pasteur.fr; Félix A. Rey: felix.rey@pasteur.fr

French COVID Cohort Study Group members: M. Bartoli, A. Diallo, S. Le Mestre, C. Paul, V. Petrov-Sanchez, Y. Yazdanpanah, C. Ficko, C. Chirouze, C. Andrejak, D. Malvy, F. Goehringer, P. Rossignol, T. Gigante, M. Gilg, B. Rossignol, M. Etienne, M. Beluze, D. Bachelet, K. Bhavsar, L. Bouadma, M. Cervantes-Gonzalez, A. Chair, C. Charpentier, L. Chenard, C. Couffignal, M.-P. Debray, D. Descamps, X. Duval, P. Eloy, M. Esposito-Farese, A.-M. Florence, J. Ghosn, I. Hoffmann, O. Kafif, A. Khalil, N. Lafhej, C. Laouénan, S. Laribi, M. Le, Q. Le Hingrat, S. Letrou, F. Mentré, G. Peytavin, V. Piquard, C. Roy, M. Schneider, R. Su, C. Tardivon, J.-F. Timsit, S. Tubiana, B. Visseaux, D. Deplanque, J.-S. Hulot, J.-L. Diehl, O. Picone, F. Angoulvant, A. Abrous, S. Couffin-Cadiergues, F.D. Da Silva, H. Esperou, I. Houas, S. Jaafoura, A. Papadopoulos, A. Gaymard, B. Lina, M. Rosa-Calatrava, C. Dorival, J. Guedj, G. Lingas, N. Neant, L. Abel, V. Manda, S. Behillil, V. Enouf, Y. Levy, and A. Wiedemann. Affiliations are listed at the end of the PDF.

CORSER Study Group members: L. Arowas, B.L. Perlaza, L. Perrin de Facci, S. Chaouche, L. Sangari, C. Renaudat, S. Fernandes Pellerin, C. van Platen, N. Jolly, L. Kuhmel, V. Garaud, H. Rafanoson, S. Gardais, N. de Parseval, C. Dugast, C. Jannet, S. Ropars, F. Momboisse, I. Porteret, I. Cailleau, B. Hoen, L. Tondeur, C. Besombes, and A. Fontanet. Affiliations are listed at the end of the PDF.

host cells through interactions of its surface envelope protein, or spike, with the cellular angiotensin-converting enzyme 2 (ACE2) receptor (Hoffmann et al., 2020; Lan et al., 2020). The SARS-CoV-2 spike (S) is a homo-trimeric glycoprotein with each protomer composed of subunits S1 and S2 (Ke et al., 2020; Walls et al., 2020; Wrapp et al., 2020). S1 contains the N-terminal domain (NTD) and the receptor-binding domain (RBD) that interacts with ACE2, while S2 mediates viral fusion (Lan et al., 2020; Yan et al., 2020). Antibodies rapidly develop in response to SARS-CoV-2 infection (Long et al., 2020; Sette and Crotty, 2021), including neutralizing antibodies recognizing distinct S protein regions (Schmidt et al., 2021). The RBD is the primary target of neutralizing antibodies including potent neutralizers, albeit the NTD and S2 stem region also contain neutralizing epitopes (Andreano et al., 2021; Brouwer et al., 2020; Chi et al., 2020; Ju et al., 2020; Liu et al., 2020; Pinto et al., 2021; Rogers et al., 2020; Wec et al., 2020; Zost et al., 2020a). SARS-CoV-2–neutralizing IgA antibodies, detected as early as a week after onset of symptoms, contribute to seroneutralization and can be as potent as IgGs (Isho et al., 2020; Sterlin et al., 2021; Wang et al., 2021b). Neutralizing antibodies are the main correlate of protection for COVID-19 vaccines (Gilbert et al., 2022; Khoury et al., 2021; Krammer, 2021). Still, SARS-CoV-2 spike–specific antibodies, including non-neutralizers, can exert antiviral Fc-dependent effector functions important for in vivo protection, i.e., antibody-dependent cellular cytotoxicity (ADCC), and phagocytosis (ADCP; Chertow et al., 2021; Dufloo et al., 2021; Schäfer et al., 2021). Unprecedented global efforts have been undertaken to develop effective vaccines and prophylactic/therapeutic strategies to fight COVID-19 (Kelley, 2020). Immunotherapies based on SARS-CoV-2–neutralizing antibodies have been rapidly explored, and this led to the clinical use of several mAbs alone or in bi-therapies (Corti et al., 2021). Highly potent human SARS-CoV-2–neutralizing mAbs isolated so far, including those tested or used in clinics, all target the RBD and can prevent infection and/or protect animals from severe disease in preclinical models (Andreano et al., 2021; Cao et al., 2020; Corti et al., 2021; Kreye et al., 2020; Noy-Porat et al., 2021; Rogers et al., 2020; Rosenfeld et al., 2021; Shi et al., 2020; Tortorici et al., 2020; Zost et al., 2020b). However, viral variants with spike mutations conferring resistance to antibody neutralization emerged during the pandemic and annihilated some of these therapies (Kumar et al., 2021; Planas et al., 2021b; Planas et al., 2021a; Radvak et al., 2021). The search for broadly neutralizing mAbs is being pursued. Novel antibodies active against all variants of concern (VOCs), including the currently prevalent Omicron lineage, have been described (Cameroni et al., 2022; Gruell et al., 2022; Westendorf et al., 2022).

Here, we report on the detailed molecular and functional characterization of 102 human SARS-CoV-2 spike mAbs cloned from IgG and IgA memory B cells of 10 convalescent COVID-19 individuals. These antibodies are encoded by a diverse set of immunoglobulin genes, recognize various conformational spike protein epitopes, and predominantly bind the S2 subunit. No anti-S2 mAbs were neutralizing, but many harbored Fc-dependent effector functions. A third of the RBD-targeting antibodies potently neutralized SARS-CoV-2 in vitro. The most potent, Cv2.1169 IgA and Cv2.3194 IgG, were fully active against VOCs Alpha, Beta, Gamma, and Delta, and still strongly blocked Omicron BA.1 and BA.2 infection in vitro. J-chain dimerization of Cv2.1169 IgA greatly improved its neutralization potency against BA.1 and BA.2. Cv2.1169 showed therapeutic efficacy in mouse and hamster SARS-CoV-2 infection models. Structural analyses by cryo-electron microscopy (cryo-EM) and x-ray crystallography revealed the mode of binding of Cv2.1169 and its contacts with the RBD at the atomic level. Collectively, this study allowed gaining insights into fundamental aspects of the SARS-CoV-2–specific humoral response and identified potent and broad neutralizers with prophylactic and therapeutic potentials.

Results

Serological antibody profiling of COVID-19 convalescents

In convalescent COVID-19 individuals, serum antibody levels against the spike and RBD proteins have been correlated to SARS-CoV-2–seroneutralizing activities (Grzelak et al., 2020; Robbiani et al., 2020; Wang et al., 2021b). To select for convalescent donors with high seroneutralization for single B-cell antibody cloning, we first evaluated the IgG and IgA seroreactivity of convalescent individuals infected during the first epidemic wave (n = 42 with bio-banked peripheral blood mononuclear cells [PBMC]) to soluble recombinant Wuhan SARS-CoV-2 trimeric spike (tri-S) and RBD proteins by ELISA. Most of them had high titers of anti–tri-S IgGs, mainly IgG1, including cross-reacting antibodies against the Middle East respiratory syndrome–related coronavirus (MERS-CoV) tri-S protein (Fig. 1, A and B; and Fig. S1, A and B). High levels of serum anti-RBD IgGs were also detected (Fig. 1, A and B; and Fig. S1, A and B) and correlated with anti–tri-S antibody titers (Fig. S1 C). Although the SARS-CoV-2 seroreactivity of IgA antibodies was globally weaker than for IgGs, both were correlated (Fig. 1 B and Fig. S1, B and C). Serum IgA and IgG antibodies from the 10 donors with the highest anti–SARS-CoV-2 tri-S antibody titers (purple dots; Fig. 1 A) were purified and showed strong ELISA binding to Wuhan nucleocapsid (N), tri-S, S1 and S2 subunits, and RBD, and also cross-reacted against recombinant spike proteins from other β-coronaviruses (SARS-CoV-1, MERS-CoV, HKU1, and OC43), as well as α-coronaviruses (229E and NL63; Fig. 1 C and Fig. S1, D and E). The neutralizing activity of purified serum IgA and IgG antibodies against the Wuhan SARS-CoV-2 strain was then determined using an in vitro pseudoneutralization assay (Fig. 1 D). 50% inhibitory concentrations (IC_{50}) of purified IgA antibodies were on average lower as compared to IgGs (70.4 vs. 115.6 µg/ml for IgAs and IgGs, respectively, P = 0.068), ranging from 43 to 133 µg/ml for IgAs, and from 21 to 257 µg/ml for IgGs (Fig. 1 D). IC_{50} values for IgA antibodies were significantly inversely correlated with their respective binding levels to SARS-CoV-2 S1 and RBD proteins (Fig. S2 A).

Human SARS-CoV-2 spike–specific memory B-cell antibodies from COVID-19 convalescents

Next, peripheral blood IgA^+ and IgG^+ memory B cells from the selected convalescent individuals were stained with fluorescently labeled RBD and tri-S, the latter being used as a bait to

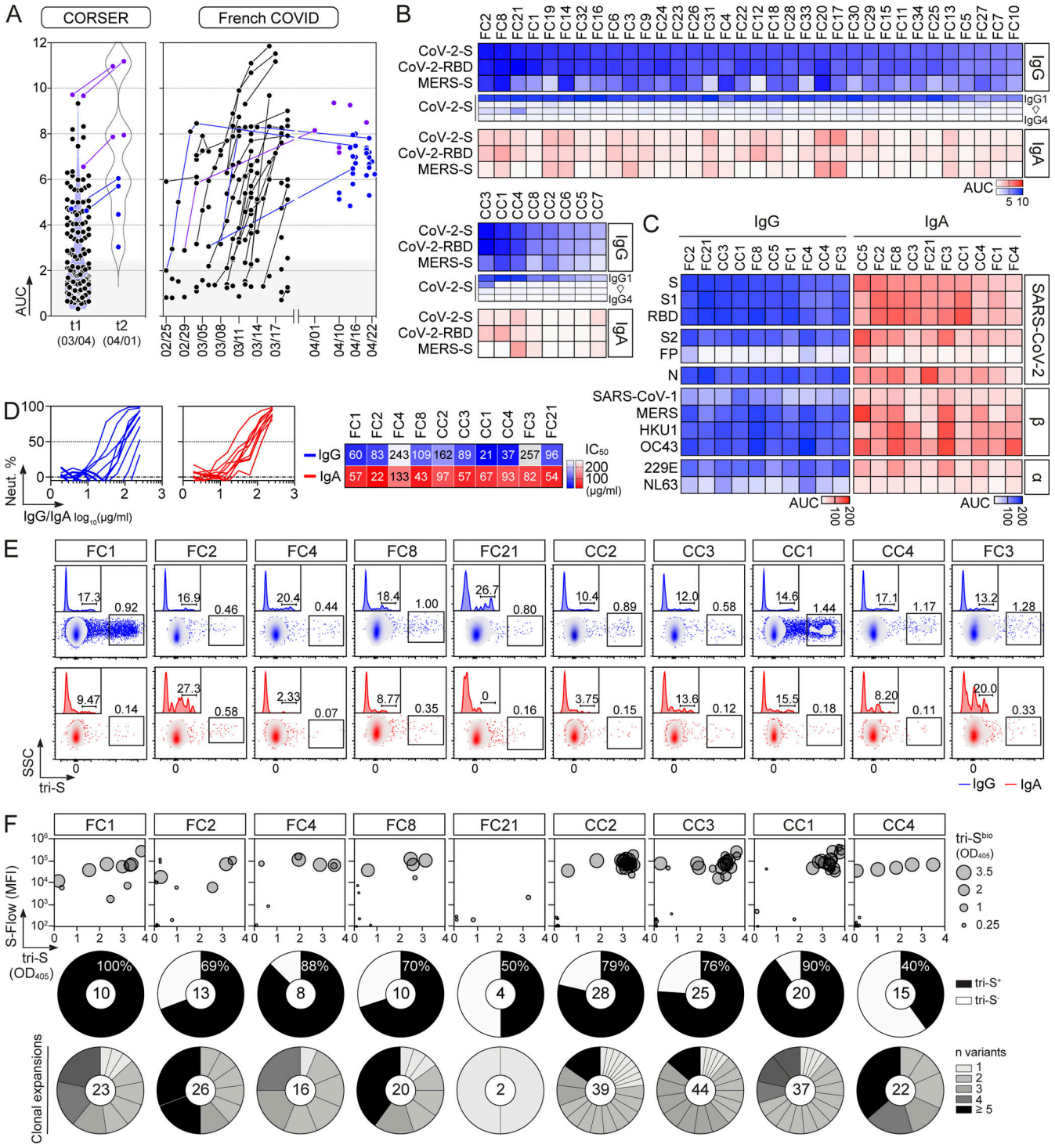

Figure 1. **SARS-CoV-2 spike–specific memory B-cell antibodies cloned from convalescent COVID-19 individuals. (A)** Dot plots showing the IgG antibody binding to SARS-CoV-2 tri-S as the area under the curve (AUC) values determined by ELISA with serially diluted sera from convalescent COVID-19 individuals in the CORSER (n = 212; two time-points, t1 and t2) and French COVID cohorts (n = 159; with a follow-up overtime for some samples). Colored dots (blue and purple) show selected samples tested in B. Purple dots indicate samples tested in C. **(B)** Heatmap showing the IgG, IgG subclass, and IgA seroreactivity of selected convalescent COVID-19 individuals from the CORSER (n = 8) and French COVID (n = 34) cohorts against SARS-CoV-2 tri-S and RBD proteins as measured in Fig. S1 B. Samples were also tested against MERS-CoV tri-S to assay for cross-reactivity against another β-coronavirus. Cells are color-coded according to AUC values with darker colors indicating high binding while light colors show moderate binding (white = no binding). **(C)** Heatmap showing the antibody binding of serum IgG and IgA antibodies purified from selected convalescent donors (n = 10) against SARS-CoV-2 antigens and tri-S proteins from other coronaviruses (α, α-coronaviruses; β, β-coronaviruses) as measured in Fig. S1, D and E. Cells are color-coded according to AUC values. FP, fusion peptide. **(D)** Graph showing the in vitro SARS-CoV-2–neutralizing activity (Neut. %) of purified serum IgG and IgA antibodies from selected COVID-19 convalescents (n = 10) measured by pseudoneutralization assay (left). Calculated IC_{50} values are presented in the heatmap on the right. **(E)** Flow-cytometric plots showing the

SARS-CoV-2 S–binding IgG⁺ and IgA⁺ memory B cells (gated on alive CD19⁺ IgG⁺ or IgA⁺ lymphocyte singlets) in the blood of convalescent donors. Flow-cytometric histograms in the upper left-hand corner show the proportion of RBD⁺ cells among SARS-CoV-2 S–binding IgG⁺ and IgA⁺ memory B lymphocytes. **(F)** Bubble plots showing the reactivity of human IgG mAbs cloned from SARS-CoV-2 S–binding IgG⁺ and IgA⁺ memory B cells of convalescent donors against SARS-CoV-2 S protein as measured by S-Flow (y axis), tri-S ELISA (x axis) and tri-S-capture ELISA (bubble size). Values are presented in Table S1. For each donor (n = 10 total), the pie chart shows the proportion of SARS-CoV-2 S–specific mAbs from total cloned antibodies (top; total number indicated in the pie chart center) and the number (n) of variants in each SARS-CoV-2 S–specific B-cell clonal family.

capture single SARS-CoV-2–reactive B cells by flow cytometric sorting (Fig. 1 E). From the 2,870 SARS-CoV-2 tri-S⁺ IgA⁺/G⁺ memory B cells isolated, we produced by expression cloning (Tiller et al., 2008), a total of 133 unique human mAbs as recombinant IgG1 antibodies from selected B cells (11 IgA⁺ and 122 IgG⁺ [85% IgG1]), with most of them being part of B-cell clonal expansions (Fig. 1 F). ELISA and flow cytometry–based (S-Flow) binding analyses showed that 101 purified mAbs specifically bind to SARS-CoV-2 S protein (76% [40–100%]; Fig. 1 F and Fig. S1 F). RBD-binding cells represented 11 and 17% of the tri-S⁺ IgA⁺ and IgG⁺ B cells, respectively (Fig. 2 A). Anti-RBD IgA titers were correlated with blood RBD⁺ IgA⁺ B-cell frequencies and inversely correlated with neutralization IC_{50} values of IgAs (Fig. S2 A). Both total and SARS-CoV-2 tri-S–specific class-switched memory B cells mainly showed a resting memory B-cell phenotype (RM, CD19⁺CD27⁺CD21⁺; Fig. 2, B–D). The frequency of circulating blood follicular helper T (cTfh) cell subsets was also determined. We found that cTfh2 cells (CD4⁺CXCR5⁺CCR6⁻CXCR3⁻), with a high proportion being activated (PD1$^{+/high}$ and/or ICOS⁺), were predominant (Fig. 2, E and F) and correlated with tri-S⁺ IgG⁺ RM B cells (r = 0.83; P = 0.0098; Fig. 2 G and Fig. S2 B), illustrating their capacity to promote class switching and affinity maturation of B cells, as previously shown (Locci et al., 2013; Morita et al., 2011). Comparison of immunoglobulin gene features with IgG⁺ memory B cells from healthy controls (Prigent et al., 2016) revealed an increased usage in the SARS-CoV-2 spike–specific B-cell repertoire of rearranged $V_H3V_\lambda3$ (P = 0.0047) and $V_\lambda3/J_\lambda2$ (P = 0.0019), J_H4 (P = 0.0312) and $J_\kappa4$ (P = 0.0387) genes, as well as IgG1 subclass (P = 0.0001; Fig. 2 H, Fig. S2, and Table S1). Anti-spike antibodies were also enriched in V_H1-24/-69 and V_H3-30/-33 genes (Fig. S2 J), as previously observed (Brouwer et al., 2020; Kreer et al., 2020; Vanshylla et al., 2022), and had reduced CDR_H3-positive charges (P = 0.0001) and somatic mutations in IgH (9.5 vs. 19.2, P < 0.0001) and Igλ (6.8 vs. 12.4, P < 0.0001; Fig. 2, H and I; Fig. S2, D and H; and Table S1). Certain antibody clones were shared among several of the COVID-19 convalescents (Fig. 2 J), demonstrating further the inter-individual convergence of antibody responses to SARS-CoV-2, as observed by others (Brouwer et al., 2020; Chen et al., 2021; Galson et al., 2020; Kreye et al., 2020; Nielsen et al., 2020; Robbiani et al., 2020; Vanshylla et al., 2022).

Binding and antiviral properties of human anti–SARS-CoV-2 spike antibodies

Epitope mapping analyses by ELISA using recombinant proteins showed that 59% of the anti-S mAbs (n = 101) bind to the S2 subunit, 16% to the RBD, 17% to the NTD, 1% to the S1 connecting domain (CD), and 7% to other regions of the SARS-CoV-2 spike (Fig. 3, A and B; and Table S1). Only one anti-S antibody (0.99% of the total) targeting S2 recognized the denatured tri-S protein by immunoblotting but did not bind S-covering linear peptides (Fig. S3, A–C), indicating that most SARS-CoV-2-S memory B-cell antibodies target conformational epitopes. To determine whether anti-spike antibodies neutralize the Wuhan strain, we measured their inhibitory activity using three different in vitro functional assays: a competition ELISA measuring the blockage of soluble tri-S or RBD binding to ACE2 ectodomain, a pseudo-neutralization assay, and a neutralizing assay using the live virus called S-Fuse (Sterlin et al., 2021; Fig. 3 C). Overall, ∼15% of the anti-S mAbs showed inhibitory activities >50% in the S-Fuse assay, many of which also neutralized pseudotyped SARS-CoV-2 virions and blocked tri-S-ACE2 interactions (Fig. 3 C and Table S1). Potent neutralizers targeted the RBD (Table S1), but only 50% of all anti-RBD mAbs blocked SARS-CoV-2 infection with IC_{50} values <10 µg/ml (Fig. 3, C, F and G; and Table S1).

SARS-CoV-2 antibodies can be armed with Fc-dependent effector functions allowing the elimination of virions and infected cells (Dufloo et al., 2021), which can alter the course of infection in vivo (Schäfer et al., 2021; Winkler et al., 2021). We evaluated the in vitro capacity of anti-S IgG1 mAbs to promote ADCC, ADCP, and complement-dependent cytotoxicity (CDC). On average, 41.6%, 74.2%, and 42.6% of the IgG antibodies displayed ADCC, ADCP, and CDC activities, respectively (Fig. 3 D). Effector activities of SARS-CoV-2 antibodies were globally correlated (Fig. 3 E). ADCC- and ADCP-inducing antibodies were directed principally against S2 (50% and 85%, respectively) and the NTD (53% and 76%, respectively; Fig. 3 F and Table S1). Conversely, anti-RBD antibodies as a group were less efficient at performing ADCC, and to a lesser extent ADCP (Fig. 3 F and Table S1). SARS-CoV-2 mAbs with CDC potential targeted mainly the NTD (59% of anti-NTD) and the RBD (56% of anti-RBD; Fig. 3 F and Table S1). Accordingly, CDC and tri-S-ACE2 blocking activities were correlated (Fig. 3 E). Principal component analyses (PCA) showed that neutralizing and Fc-dependent effector functions segregated into two separate clusters in the PCA of antiviral functions, with 77% of the variance reached when combining the two first principal components (Fig. 3 G). The "neutralization" cluster included mainly anti-RBD antibodies, while the "effector" cluster comprised both NTD- and S2-specific IgGs (Fig. 3 G).

Antibody features of potent SARS-CoV-2 neutralizers

In the collection of 101 anti-S mAbs, five potent SARS-CoV-2 neutralizing antibodies were identified (Table S1). They bound to the recombinant tri-S, S1, and RBD proteins with high affinity, as measured by surface plasmon resonance (Fig. 4 A and Table S2). They targeted similar or spatially close epitopes on the RBD as shown by their cross-competition for ligand binding by ELISA (Fig. 4 B and Fig. S3 D). They efficiently blocked the interaction of tri-S to the soluble ACE2 ectodomain (Fig. 4 C), suggesting

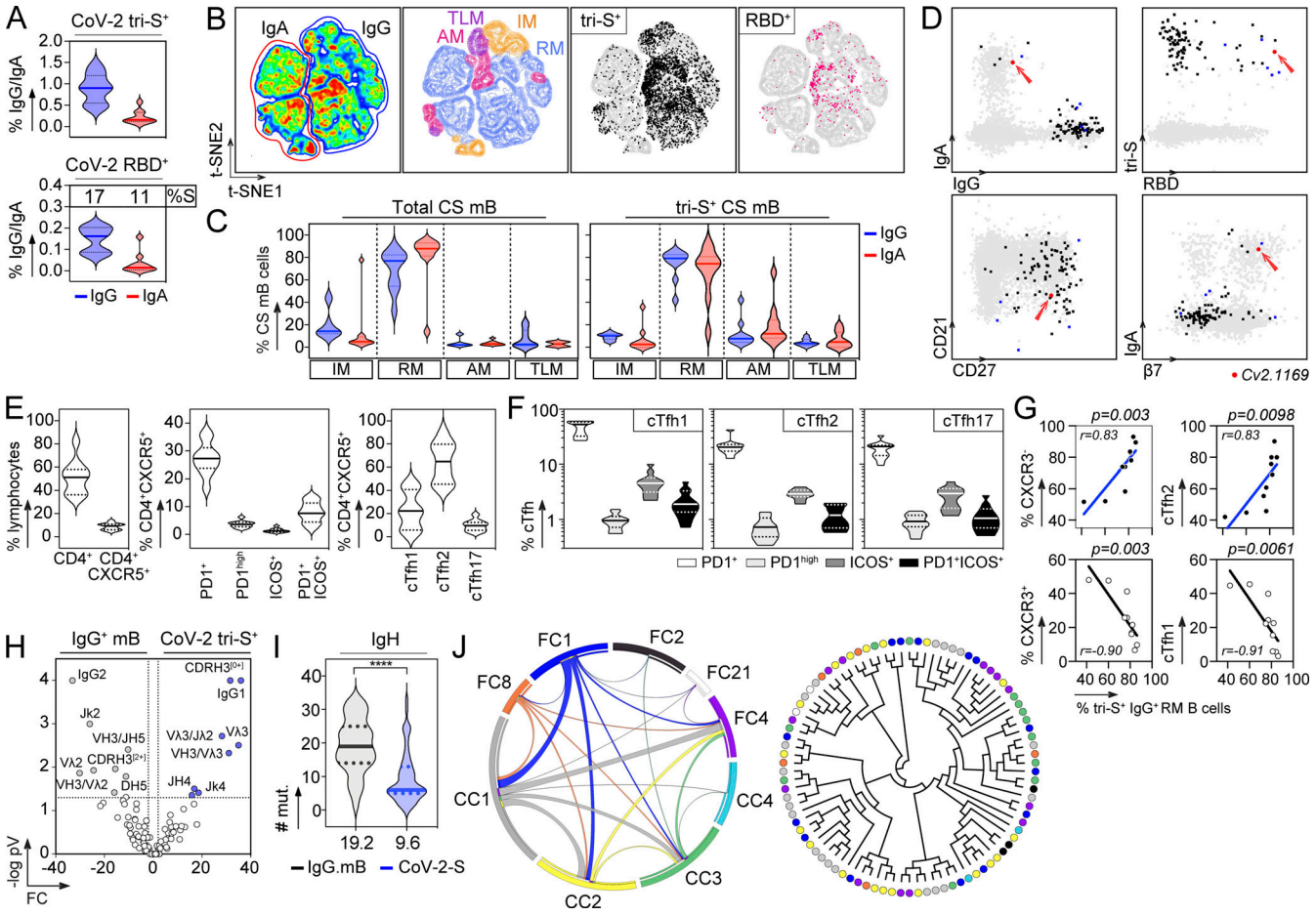

Figure 2. **Immunophenotyping and antibody gene repertoire of SARS-CoV-2 spike–specific memory B cells. (A)** Violin plots showing the percentage of SARS-CoV-2 tri-S$^+$ cells among total IgG$^+$ and IgA$^+$ memory B cells (top) and of SARS-CoV-2 RBD$^+$ cells among tri-S$^+$ IgG$^+$ and IgA$^+$ memory B cells (bottom) in the blood of convalescent COVID-19 individuals (n = 10). **(B)** Pseudocolor plots showing the t-SNE analysis of concatenated Vivid$^-$CD19$^+$CD10$^-$ B cells in convalescent COVID-19 individuals (n = 10). Density maps presenting the staining intensity of CD27 and CD21 markers used to define memory B-cell subsets. IM (intermediate memory, CD27$^-$CD21$^+$), RM (resting memory CD27$^+$CD21$^+$), AM (activated memory, CD27$^+$CD21$^-$), and TLM (tissue-like memory CD27$^-$CD21$^-$). Black and pink dots indicate tri-S$^+$ and RBD$^+$ IgG$^+$ and IgA$^+$ B memory cells in the density maps. **(C)** Violin plots showing the distribution of total and SARS-CoV-2 tri-S$^+$ IgG$^+$ and IgA$^+$ memory B-cell subset frequencies as depicted in B. CS mB, class-switched memory B cells in convalescent COVID-19 individuals (n = 10). **(D)** Immunophenotyping flow cytometric plots showing the expression of B-cell surface markers on sorted SARS-CoV-2 tri-S–specific B cells (n = 101, black, blue, and red dots). Blue dots indicate potent neutralizing antibodies while the red dot is the ultra-potent neutralizer Cv2.1169 (red arrow). **(E)** Violin plots showing the frequency of total CD4$^+$, CD4$^+$CXCR5$^+$ lymphocytes, and cTfh cell subsets in the blood of convalescent COVID-19 individuals (n = 10). **(F)** Violin plots comparing the frequency of PD1$^+$, PD1^{hi}, ICOS$^+$, and ICOS$^+$PD1$^+$ cells among cTh1, cTfh2, and cTh17 cell subsets in the blood of convalescent COVID-19 individuals (n = 10). **(G)** Correlation plots showing the frequency of SARS-CoV-2 tri-S$^+$ IgG$^+$ RM B cells vs. CXCR3$^+$ cTfh, CXCR3$^-$ cTfh, cTfh1, and cTfh2 cells. Spearman correlation coefficients with the corresponding P values are indicated. **(H)** Volcano plot analysis comparing the immunoglobulin gene repertoire of SARS-CoV-2 S–specific IgG$^+$/IgA$^+$ B cells from convalescent donors and IgG$^+$ memory B cells from healthy individuals (IgG.mB, unexposed to SARS-CoV-2; Prigent et al., 2016). Gray and blue dots indicate statistically significant differences between both Ig gene repertoires. pV, P value; FC, fold changes. **(I)** Violin plots comparing the number of mutations in V_H genes of SARS-CoV-2 S–specific (n = 101) and control IgG$^+$ memory B cells from unexposed healthy individuals (n = 72; Prigent et al., 2016). The average number of mutations is indicated below. Numbers of mutations were compared across groups of antibodies using unpaired student t test with Welch's correction. ****, P < 0.0001. **(J)** Circos plot (left) showing the clonal variants shared between distinct donors with the size of the links proportional to the number of clones sharing 75% CDR_H3 amino acid identity. Cladogram (right) showing the distribution of individual shared clones between donors (n = 9).

that they recognize the receptor-binding motif (RBM). IC_{50} values for SARS-CoV-2 neutralization, determined using the pseudoneutralization and S-Fuse assays, ranged from 3 to 37 ng/ml and from 0.95 to 11.5 ng/ml, respectively (Fig. 4 D). The most potent antibody, Cv2.1169, was encoded by V_H1-58/D_H2-15/J_H3 and Vκ3-20/Jκ1 immunoglobulin gene rearrangements and exhibited low levels of somatic mutation (3.1% V_H and 2.1% V_K at the amino acid level; Table S1). The potential of the SARS-CoV-2 neutralizers to bind with low-affinity unrelated ligands (polyreactivity) and to cross-react with self-antigens was then evaluated in different complementary binding assays (Fig. 5, A–F). None of the antibodies displayed self-reactivity, while only Cv2.3235 and Cv2.3194 showed polyreactivity (Fig. 5, A–F). None of the potent neutralizers had ADCC potential but showed moderate CDC and robust ADCP activities (Fig. 5, G–I; and Table S1). Remarkably, Cv2.1169, expressed as IgG1 antibodies, was one of the strongest ADCP-inducer among all the SARS-CoV-2 Spike mAbs (top 2%; Fig. 5 I and Table S1).

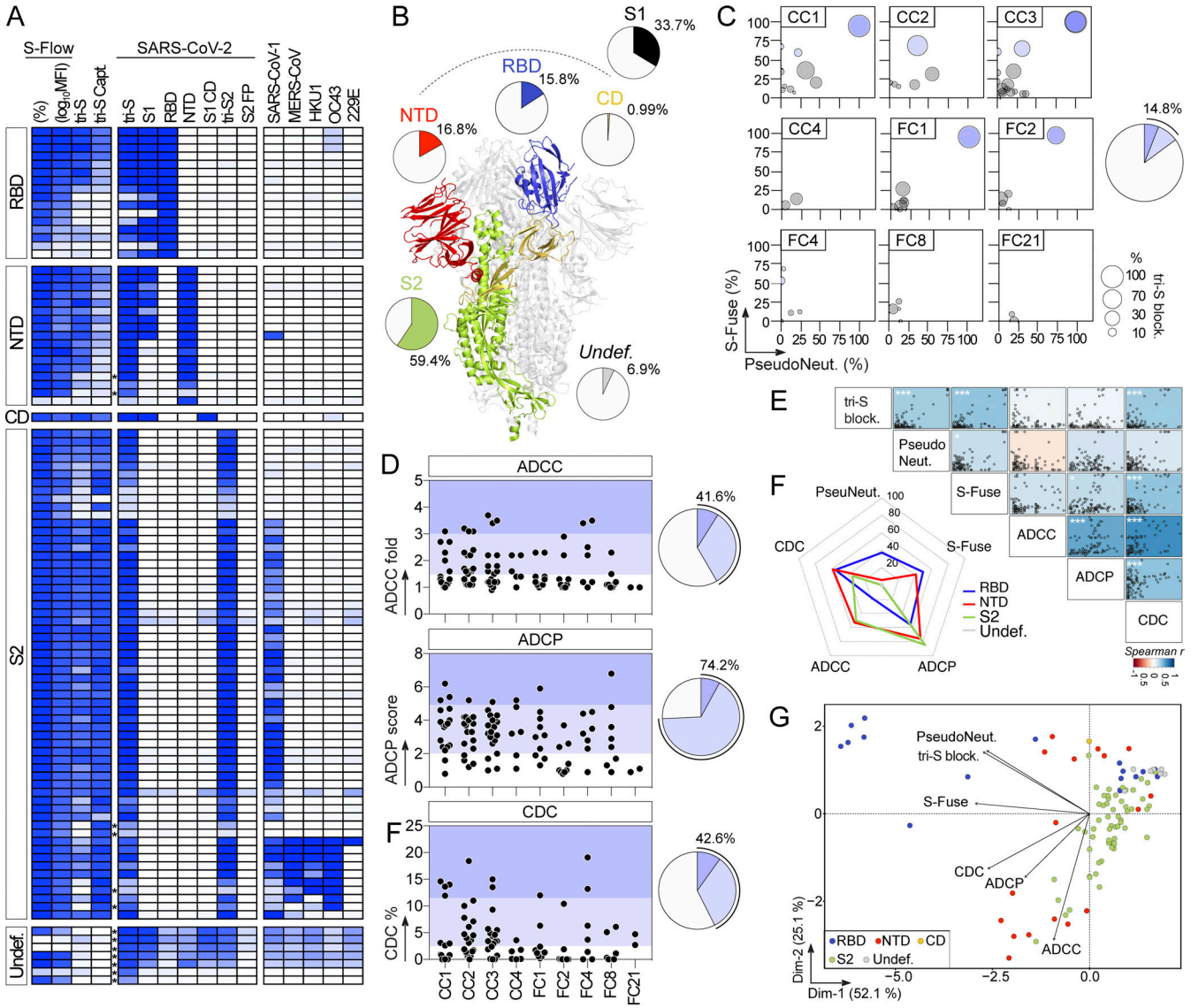

Figure 3. **Reactivity and antiviral properties of SARS-CoV-2 S–specific memory B-cell antibodies. (A)** Heatmap showing the ELISA reactivity of human anti-S mAbs (*n* = 101) against purified recombinant SARS-CoV-2 antigens and tri-S proteins from other coronaviruses (α-coronaviruses: SARS-CoV-1, MERS-CoV, HKU1; and β-coronaviruses: OC43, 229E). FP, fusion peptide. Cells are color-coded according to the binding values presented in Table S1 with darker colors indicating strong reactivities (white = no binding). Asterisks indicate the antibodies tested at a higher IgG concentration. Undef., undefined region. **(B)** Schematic diagram showing the distribution of specificities of anti-S antibodies (*n* = 101) on the highlighted regions of the SARS-CoV-2 spike as determined in A (ribbon representation of the PDB ID: 6VXX structure). **(C)** Bubble plots showing the neutralization activity of human SARS-CoV-2 S–specific antibodies (*n* = 101) tested at a concentration of 10 µg/ml in the S-Fuse (y axis), and pseudoneutralization (x axis, PseudoNeut.) assays against SARS-CoV-2. The bubble size corresponds to the blocking capacity of SARS-CoV-2 S-ACE2 interactions by the antibodies as measured by ELISA. Corresponding values are presented in Table S1. Pie chart (right) shows the distribution of non-active (white) vs. neutralizing (shades of blue) antibodies according to neutralization percentage measured with the S-Fuse assay. **(D)** Dot plot showing the in vitro Fc-dependent effector activities of anti-S IgG antibodies (*n* = 101). Pie charts (right) show for each measured effector function the distribution of non-active (white) vs. active (shades of blue) antibodies. **(E)** Matrix showing the correlation analyses between neutralization activities and Fc-dependent effector functions measured for SARS-CoV-2 S–specific IgG antibodies (*n* = 101). Spearman correlation coefficients (color coded) with their corresponding P values are shown. ***, P < 0.001; *, P < 0.05. **(F)** Radar plots comparing the in vitro neutralizing and Fc-dependent effector activities of anti-S IgG antibodies (*n* = 101) according to the targeted spike regions. Percent of antibodies per specificity group mediating a given antiviral activity as determined in D is shown. **(G)** PCA 2D-plot showing the antiviral-related variables discriminating anti-S mAbs (*n* = 101) color-coded by specificities. The two dimensions account for 77.2% of the variability. The location of the variables is associated with the distribution of the antibodies.

Neutralization spectrum of potent SARS-CoV-2 neutralizers

Several SARS-CoV-2 VOCs, i.e., Alpha (α, B.1.1.7), Beta (β, B.1.351), Gamma (γ, P.1), and Delta (δ, B.1.617.2), and variants of interest (VOIs) have emerged during the pandemic (WHO, 2022). We next evaluated the cross-reactive potential of the 16 anti-RBD antibodies against VOCs and VOIs. Binding analyses by flow cytometry showed that three out of the five potent neutralizers bound to cells expressing the spike proteins from VOCs (α, β, γ, δ) and VOIs (ε, ι, κ, λ, μ), while most non-neutralizing antibodies had narrowed cross-reactivity spectra

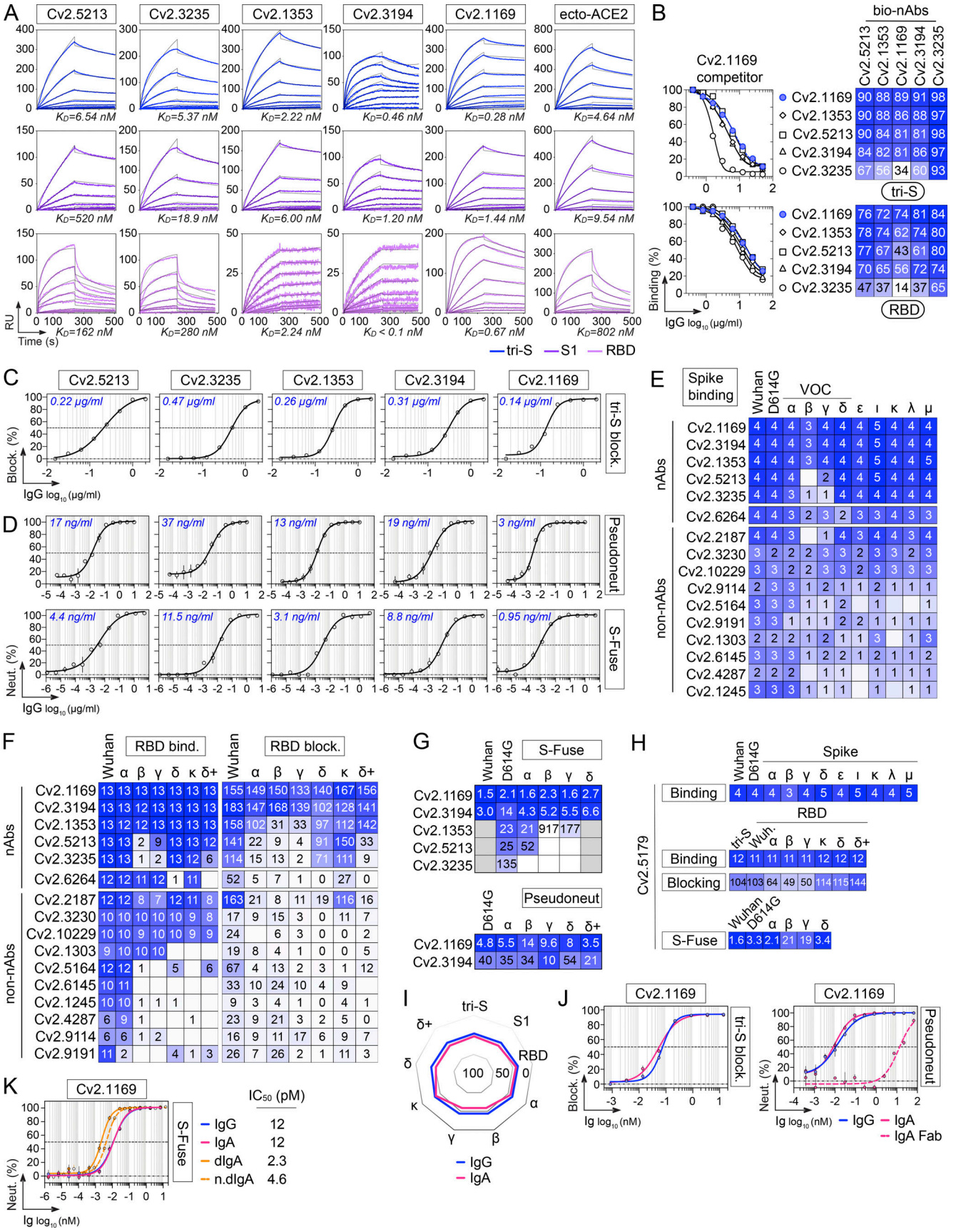

Figure 4. **Binding and neutralizing activities of potent anti-RBD neutralizers. (A)** SPR sensorgrams comparing the relative affinity of purified neutralizing anti-RBD IgG mAbs (n = 5) for the binding to trimeric SARS-CoV-2 S (tri-S; blue), S1 (purple) and RBD (pink) proteins. Calculated K_D values are indicated at the

bottom. ecto-ACE2, purified recombinant ACE2 ectodomain. **(B)** Representative competition ELISA graphs (left) comparing the IgG binding to SARS-CoV-2 tri-S (top) and RBD (bottom) of selected biotinylated anti-RBD antibodies (n = 5) in presence of Cv2.1169 as a potential competitor. Means ± SD of duplicate values are shown. Heatmaps (right) showing the competition of selected anti-RBD nAbs (n = 5) for tri-S and RBD binding as measured in Fig. S3 D. Dark blue indicates stronger inhibition; lighter colors indicate weaker competition, and white indicates no competition. **(C)** Competition ELISA graphs showing the binding of biotinylated SARS-CoV-2 tri-S protein to the immobilized soluble ACE2 ectodomain in presence of anti-RBD antibodies used as competitors. Means ± SD of duplicate values are shown. **(D)** Graphs showing the neutralization curves of Wuhan SARS-CoV-2 by selected anti-RBD IgG antibodies (n = 5) as determined with the pseudo-neutralization (top) and S-Fuse neutralization (bottom) assays. Error bars indicate the SD of assay triplicates. IC_{50} values are indicated in the top left-hand corner (in blue). **(E)** Heatmap comparing the binding of RBD-specific IgG antibodies to the cell-expressed spike proteins of SARS-CoV-2 and selected viral variants as measured by flow cytometry. Geometric means of duplicate log_{10} ΔMFI values are shown in each cell. **(F)** Heatmaps comparing the binding (left) and RBD-ACE2 blocking capacity (right) of RBD-specific IgG antibodies for the RBD proteins of SARS-CoV-2 and selected viral variants as measured in Fig. S3, E and H. Darker blue colors indicate high binding or competition while light colors show moderate binding or competition (white = no binding or competition). AUC values are shown in each cell. **(G)** Heatmaps comparing the IC_{50} neutralizing values of the selected anti-RBD antibodies against SARS-CoV-2 and selected VOCs with the pseudo-neutralization (top) and S-Fuse neutralization (bottom) assays as measured in Fig. S4, A and B. **(H)** Heatmap showing the binding to spike and RBD proteins (top), RBD-ACE2 blocking capacity (middle), and neutralizing activity (bottom) for Cv2.5179 antibody as measured in Fig. S4, D–G. **(I)** Radar plot comparing the binding of monomeric Cv2.1169 IgG and IgA antibodies to SARS-CoV-2 tri-S, S1, and RBD proteins, and to RBD from selected viral variants as measured in Fig. S4 I. **(J)** Competition ELISA graphs (left) comparing the binding of biotinylated SARS-CoV-2 tri-S protein to the immobilized soluble ACE2 ectodomain in presence of Cv2.1169 IgG or IgA as a competitor. Means ± SD of duplicate values are shown. Graphs (right) comparing the SARS-CoV-2–neutralizing activity of Cv2.1169 IgG, IgA, and IgA Fab as determined with the pseudo-neutralization assay. Error bars indicate the SD of duplicate values. **(K)** Graphs comparing the SARS-CoV-2–neutralizing activity of monomeric and dimeric IgA (dIgA) Cv2.1169 antibodies as determined with the S-Fuse neutralization assay. Error bars indicate the SD of triplicate values. n.dIgA, normalized values according to the number of binding sites.

(Fig. 4 E). Only neutralizers Cv2.1169, Cv2.3194, and Cv2.1353, as well as a third of the non-neutralizing antibodies displayed unaltered ELISA binding to RBD proteins from the VOCs α, β, γ, δ, and VOIs κ, $δ^+$ (Fig. 4 F; and Fig. S3, E and G). Cv2.1169 and Cv2.3194 were the sole anti-RBD antibodies uniformly blocking the interaction of the ACE2 ectodomain with RBD proteins from the viral variants tested (Fig. 4 F; Fig. S3, F and H; and Table S2). Three potent neutralizers encoded by V_H3-53/-66 immunoglobulin genes (Cv2.1353, Cv2.5213, and Cv2.3235) were sensitive to RBD mutations at positions 417 and 501 (Dejnirattisai et al., 2021a; Wibmer et al., 2021) and lost binding and/or blocking activity against SARS-CoV-2 variants α, β, γ, and δ (Fig. 4 F and Fig. S3, E–H). Both S-Fuse and pseudo-neutralization assays showed that Cv2.1169 and Cv2.3194 neutralized SARS-CoV-2 VOCs α, β, γ, and δ (Fig. 4 G; and Fig. S4, A and B). V_H3-53 gene-expressing antibody Cv2.3194 efficiently bound and neutralized all the variants, most likely due to the usage of rearranged Vκ3-20/Jκ4 light chain genes, as previously reported (Dejnirattisai et al., 2021a). Among these cross-neutralizers, Cv2.1169 was the most potent with IC_{50} values ranging from 1.5 to 2.7 ng/ml against Wuhan, D614G variant, α, β, γ, and δ strains in the S-Fuse assay, and from 3.5 to 14 ng/ml against D614G variant, α, β, γ, δ, and $δ^+$ strains in the pseudo-neutralization assay (Fig. 4, D and G; Fig. S4, A and B; and Table S2). Cv2.1169 ranked among the strongest crossneutralizers when compared to the parental versions of benchmarked antibodies used in clinics or development (Fig. 6, A–C). In addition, we produced a Cv2.1169 IgG homolog (V_H1-58/D_H2/J_H3 and Vκ3-20/Jκ1), from a different convalescent donor based on interindividual clonal convergence analyses (Fig. S4, C and D), Cv2.5179, which also exhibited a potent and broad SARS-CoV-2–neutralizing activity (Fig. 4 H and Fig. S4, E–G).

Immunophenotyping of sorted B cells indicated that Cv2.1169 was originally produced by a $Spike^+RBD^+$ IgA^+ B cell with an activated memory phenotype ($CD27^+CD21^-$) and a surface-expression of the mucosa-homing integrin β7 (Fig. 2 D). We thus also expressed Cv2.1169 as a monomeric IgA antibody, which showed equivalent binding and neutralization activities compared to its IgG counterpart (Fig. 4, I and J; and Fig. S3 I). In contrast, purified J-chain containing IgA dimers demonstrated a higher neutralizing capacity against the Wuhan strain (Fig. 4 K), suggesting an enhanced neutralization by binding avidity effects, as previously reported (Barnes et al., 2020a; Rujas et al., 2021). Accordingly, the neutralizing activity of Cv2.1169 IgA Fab against SARS-CoV-2 was strongly impaired as compared to the bivalent immunoglobulins (Fig. 4 J).

SARS-CoV-2 Omicron variant B.1.1.529 or BA.1 became dominant worldwide in January 2021, followed by Omicron BA.2 in March 2022 (WHO, 2022). Omicron BA.1 contains 15 RBD-amino acid substitutions, which conferred resistance to numerous potent anti-RBD neutralizers including those in clinical use (Cameroni et al., 2022; Cao et al., 2022a; Planas et al., 2022). BA.2 has seven amino acids differing from BA.1 in the RBD and is also less sensitive to antibody neutralization (Bruel et al., 2022). Cv2.1169 and Cv2.3194, but not the other anti-RBD antibodies, bound well to cell-expressed and soluble BA.1 spike proteins as well as to the BA.1 RBD (Fig. 7 A). Both antibodies blocked BA.1 tri-S binding to ACE2, although less efficiently than for the Wuhan viral spike (Fig. 7 B). Cv2.1169 and Cv2.3194 also had the highest binding and spike-ACE2–blocking capacity to BA.1 viral proteins by ELISA as compared to benchmarked antibodies (Fig. 7, C and D). Cv2.1169 and Cv2.3194, but not Cv2.5179, neutralized BA.1 in the S-Fuse assay with IC_{50} of 253 and 24.2 ng/ml, respectively (Fig. 7 E and Table S2). Thus, Cv2.1169 and Cv2.3194 presented, respectively, a 79- and 2.2-fold decreased neutralization efficacy on Omicron BA.1 as compared to Delta (Fig. 7 E). In contrast, Cv2.1169 and Cv2.3194 showed a slightly stronger RBD-binding against Omicron BA.2 as compared to BA.1 (Fig. 7 D). Consistently, both antibodies blocked more efficiently the binding of the RBD BA.2 to soluble ACE2 (Fig. 7 F). Nonetheless, Cv2.1169 and Cv2.3194 showed comparable neutralizing activities against BA.1 and BA.2 in the S-Fuse assay (Fig. 7 G). As compared to their monomeric counterpart, dimeric Cv2.1169 IgA antibodies had enhanced RBD-binding and spike-ACE2 blocking activities to Omicron variants, especially BA.1 (Fig. 7, H and I). This translated into an increased neutralizing potency of Cv2.1169 IgA

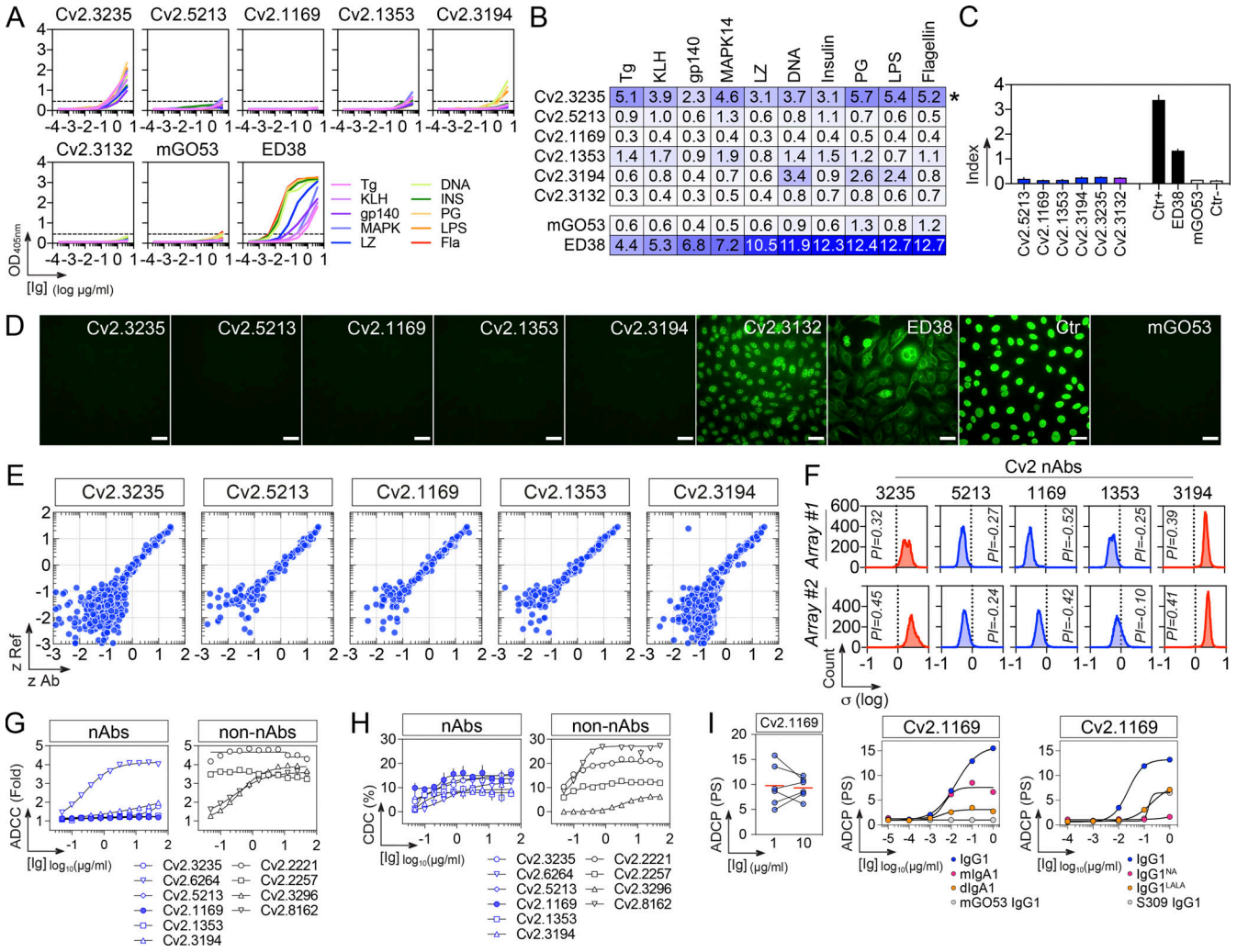

Figure 5. **Off-target binding and Fc-effector functions of potent SARS-CoV-2–neutralizing antibodies. (A)** Representative ELISA graphs showing the reactivity of selected SARS-CoV-2–neutralizing antibodies (n = 5) against double-stranded DNA (DNA), flagellin (Fla), YU2 HIV-1 Env (gp140), insulin (INS), keyhole limpet hemocyanin (KLH), lipopolysaccharide (LPS), lysozyme (LZ), MAPK-14 (MAPK), proteoglycan (PG), and thyroglobulin (Tg). mGO53 (Wardemann, 2003) and ED38 (Meffre et al., 2004) are negative and positive control antibodies, respectively. Anti–SARS-CoV-2 S antibody Cv2.3132 showing HEp-2 reactivity in C was included for comparison. The mean of duplicate values are shown. **(B)** Heatmap comparing the AUC values determined from the ELISA binding analyses shown in A. Darker blue colors indicate high binding while light colors show moderate binding (white = no binding). **(C)** Bar graph showing the HEp-2 reactivity of selected SARS-CoV-2 antibodies as measured by ELISA. Means ± SD of duplicate values are shown. Ctr+ and Ctr− are the positive and negative control of the kit, respectively. **(D)** Microscopic images showing the reactivity of selected SARS-CoV-2–neutralizing mAbs (n = 5) to HEp2-expressing self-antigens assayed by indirect immunofluorescence assay. The negative (mGO53), low-positive (ED38), and kit's positive (Ctr+) controls were included in the experiment. HEp-2–reactive anti–SARS-CoV-2 S antibody Cv2.3132 was also included for comparison. The scale bars represent 40 µm. **(E)** Representative microarray plots showing the z-scores given on a single human protein by the reference (Ref: mGO53, y axis) and test antibody (x axis). Each dot represents the average of duplicate array proteins. **(F)** Frequency histograms showing the $\log_{10}$ protein displacement (σ) of the MFI signals for the selected SARS-CoV-2 antibodies compared to non-reactive antibody mGO53 obtained from two independent experiments (array #1 and #2). The PI corresponds to the Gaussian mean of all microarray protein displacements. Blue and red histograms indicate non-polyreactive and polyreactive mAbs, respectively. **(G)** Graphs comparing the natural killer cell–mediated ADCC activity of selected neutralizing (nAbs) and non-neutralizing (non-nAbs) SARS-CoV-2 S–specific antibodies (n = 10). Means ± SD of duplicate values are shown. **(H)** Same as in G but for the CDC activity. **(I)** ADCP activity of Cv2.1169. The dot plot (left) shows the monocyte-mediated ADCP activity of Cv2.1169 IgG at a concentration of 1 and 10 µg/ml. Each dot corresponds to a donor of primary monocytes (n = 6). Graph comparing the ADCP activity of Cv2.1169 expressed as recombinant IgG1, $IgG1^{NA}$, $IgG1^{LALA}$, monomeric IgA1 (mIgA1), and dimeric IgA1 (dIgA1) antibodies. mGO53 is the negative isotype control, and ADCP-inducing IgG1 antibody S309 was included for comparison. PS, phagocytic score. Means of duplicate values are shown.

dimers against BA.1 and BA.2 by a 13- and 20-fold, respectively when normalized for the number of binding sites (Fig. 7 J).

Structural characterization of the epitopes

To define the epitopes and neutralization mechanisms of selected anti-RBD mAbs, we co-crystallized the corresponding Fab in complex with the Wuhan RBD. The structures of the Cv2.3235 Fab/RBD and the Cv2.6264 Fab/RBD complexes were determined to 2.3 and 2.8 Å resolution, respectively (Fig. 8 and Table S3). The Cv2.1169 Fab/RBD binary complex did not crystallize, but the Cv2.1169 IgA Fab/CR3022 IgG1 Fab/RBD ternary complex produced crystals that allowed us to determine the x-ray

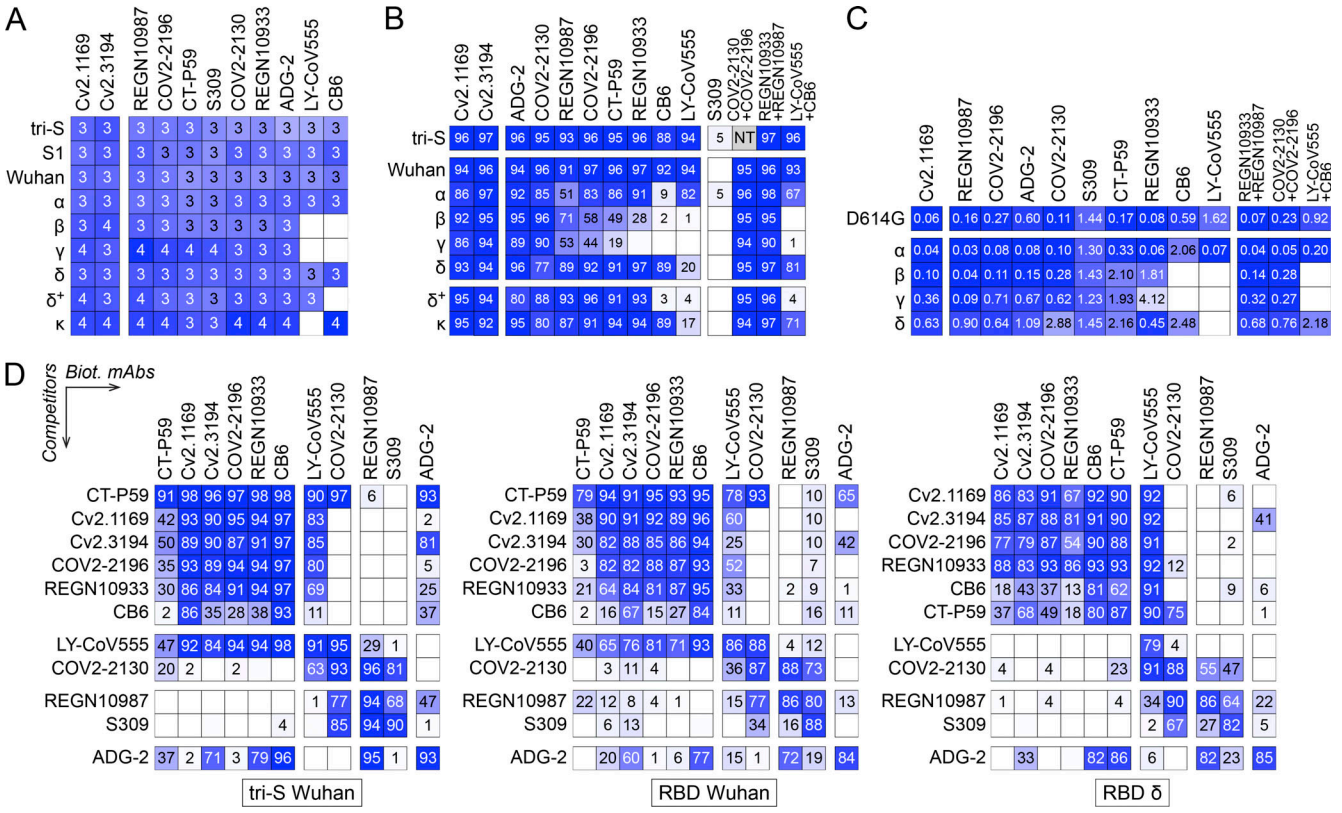

Figure 6. **Comparative analyses of Cv2.1169 and Cv2.3194 with benchmarked antibodies. (A)** Heatmap comparing the ELISA binding to the selected SARS-CoV-2 proteins of Cv2.1169, Cv2.3194, and benchmarked neutralizing antibodies in clinical use or in development. Darker blue colors indicate high binding while light colors show moderate binding or competition (white = 0, no binding). Means of duplicate AUC values are shown in each cell. **(B)** Heatmap comparing the tri-S- and RBD-ACE2 blocking capacity of Cv2.1169, Cv2.3194 and benchmarked neutralizing antibodies. Darker blue colors indicate high competition while light colors show moderate competition (white = 0, no competition). Means of duplicate values (% binding inhibition) are shown in each cell. NT, not tested. **(C)** Heatmap comparing the in vitro neutralizing activity of Cv2.1169 and benchmarked neutralizing antibodies against the selected SARS-CoV-2 viral variants. Means of triplicate IC_{50} values in pM are shown in each cell. White color indicates that 50% neutralization was not reached at the maximum antibody concentration of 25 nM. **(D)** Heatmaps showing the competition potential of Cv2.1169, Cv2.3194, and benchmarked neutralizing antibodies for the ELISA binding to tri-S and RBD proteins. Darker blue colors indicate high competition while light colors show moderate competition (white = 0, no competition). Means of duplicate values (% binding inhibition) are shown in each cell.

structure to 2.9 Å. The electron density maps for the ternary complex were of poor quality and uninterpretable for the constant domain of Cv2.1169 Fab, indicating their intrinsic mobility. The Cv2.1169 variable domains and the paratope/epitope region were however well resolved (Table S3). The structure revealed that Cv2.1169 binds the RBM and straddles the RBD ridge leaning toward the face that is occluded in the "down" conformation of the RBD on a "closed" spike (Fig. 9 A). This binding mode is similar to other V_H1-58/V_K3-20–derived neutralizing antibodies (Dejnirattisai et al., 2021b; Starr et al., 2021; Tortorici et al., 2020; Wang et al., 2021a), as shown in the superposition of the RBD complexed with A23-58.1, COVOX-253, and S2E12 mAbs (Fig. 9 B). Superposing the structures of the RBD/Cv2.1169 and RBD/ACE2 complexes showed extensive clashes between the antibody and the ACE2 receptor (Fig. 9 C), providing the structural basis for its neutralization mechanism and agreeing with its RBD-ACE2 blocking capacity (Fig. 4, C and F; and Fig. S3, F and H). Cv2.1169, Cv2.3235, and Cv2.6264 bound differently to the RBD, with Cv2.1169 having the lowest total buried surface area (BSA; ∼1,400, ∼2,620, and ∼1,610 Å^2, for Cv2.1169, Cv2.3235, and Cv2.6264, respectively; Table S4), despite being the only mAb that contacts the RBD with all its CDRs. Cv2.1169 also has the highest heavy chain contribution to the interaction surface (∼80% of the paratope's BSA), mainly through the CDR_H3 (Table S4). The Cv2.1169 CDR_H3 (14 amino acid length by Kabat definition) bends at P99 and F110, delimiting a tongue-like loop that is stabilized by a disulfide bond between $C101^{CDRH3}$ and $C106^{CDRH3}$ (Fig. 9 D). This particular shape allows residues between G103 and F110, which are on one side of the CDR_H3 tongue, to recognize the RBD tip and form hydrogen bonds through their main-chain atoms (Fig. 9 D and Table S5). The interface is further stabilized by polar interactions between the side chains of D108 in the CDR_H3 and Y33 in the CDR_L1 (Fig. 9 D and Table S5).

Cv2.1169 epitope comprises the RBD segments 417–421, 455–458, 473–478, and 484–493 (Fig. 9, A and D; and Table S5). Apart from T478, all the mutated RBD residues present in the SARS-CoV-2 VOCs prior to Omicron are at the rim of the contact area (K417, E484) or outside (L452, N501; Fig. 9, A and D). Conversely, Cv2.3235 interacts with several residues mutated in several VOCs, e.g., K417 and N501 (Fig. 8, A and C), explaining its reduced capacity to bind and neutralize α, β, γ, and δ+ variants

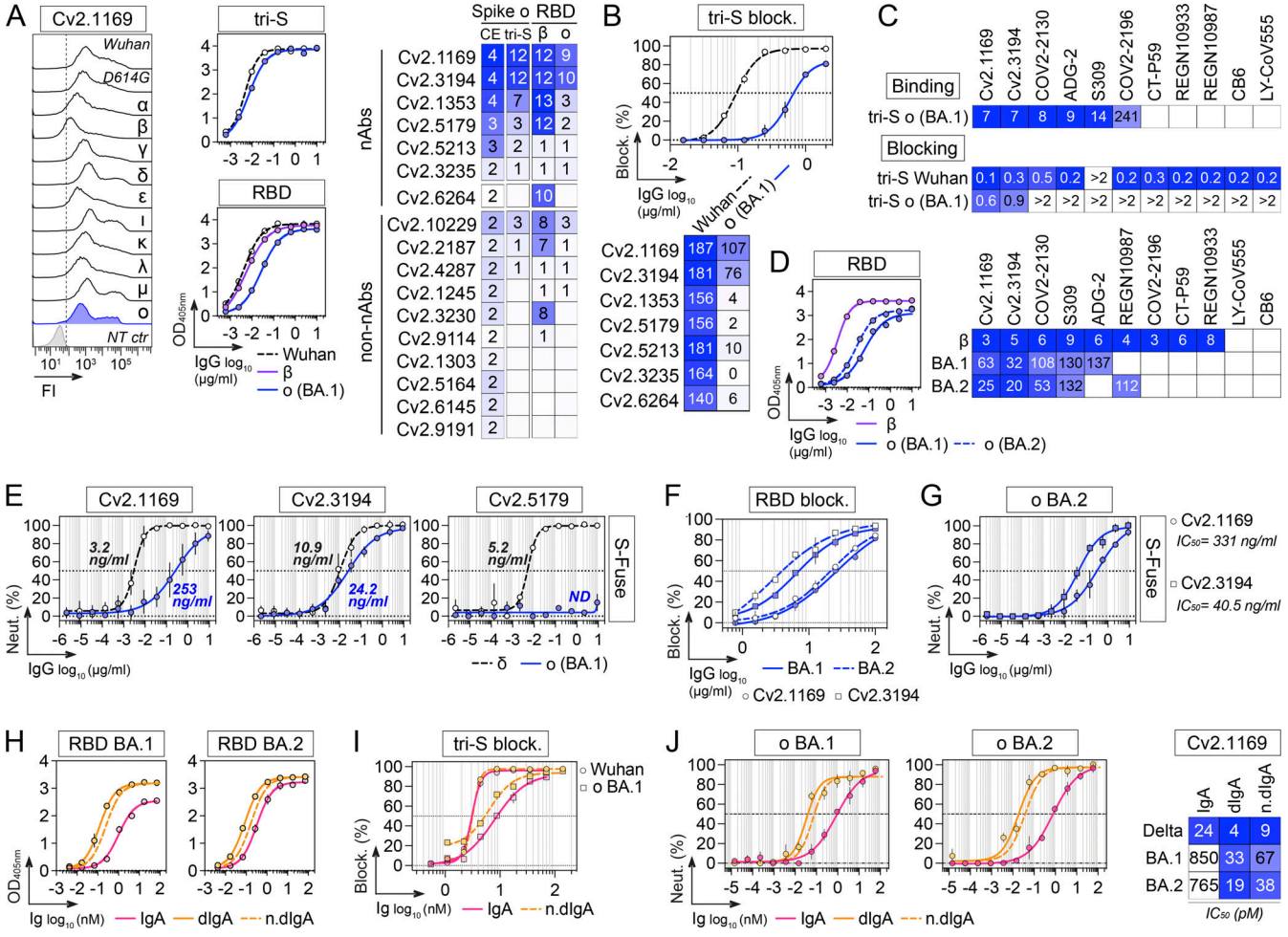

Figure 7. **Activity of Cv2.1169 and Cv2.3194 against SARS-CoV-2 Omicron variants. (A)** Heatmap (right) comparing the binding of RBD-specific IgG antibodies (n = 17) to the cell-expressed (CE) and soluble (tri-S) Omicron (o) SARS-CoV-2 spike proteins as measured by flow cytometry (mean $\log_{10}$ ΔMFI from duplicate values) and ELISA (mean AUC from duplicate values), respectively, as shown on the left for Cv2.1169. NT ctr, non-transfected cell control. The heatmap also presents the comparative antibody reactivity (AUC values) against β and o RBD proteins. White indicates no binding. **(B)** Heatmap (bottom) comparing the RBD-ACE2 blocking capacity of neutralizing anti-RBD antibodies (n = 7) for the RBD proteins of SARS-CoV-2 and o variant BA.1 as shown for Cv2.1169 (top; means ± SD of duplicate values are shown). Darker blue colors indicate high competition while light colors show moderate competition (white = no binding or competition). Mean AUC from duplicate values are shown in each cell. **(C)** Heatmaps comparing the tri-S binding (top) and tri-S-ACE2 blocking capacity (bottom) of Cv2.1169 and Cv2.3194 with benchmarked RBD-specific SARS-CoV-2 IgG neutralizers (n = 9) to the SARS-CoV-2 proteins of the o variant BA.1. Darker blue colors indicate high binding or competition while light colors show moderate binding or competition (white = no binding or competition). Mean EC_{50} from duplicate values are shown in each cell. **(D)** Heatmap (right) comparing the binding of Cv2.1169 and Cv2.3194 with benchmarked SARS-CoV-2 neutralizers for the RBD proteins of the o variant BA.1 and BA.2 as measured by ELISA (means of duplicate AUC values) as shown on the left for Cv2.1169. Darker blue colors indicate high binding while light colors show moderate binding (white = no binding). Mean EC_{50} from duplicate values are shown in each cell. **(E)** Graphs showing the neutralization curves of SARS-CoV-2 δ and o BA.1 by potent anti-RBD IgG antibodies as determined with the S-Fuse neutralization assay. Error bars indicate the SD of duplicate values from 2 (Cv2.5179) or 5 (Cv2.1169 and Cv2.3194) independent experiments. IC_{50} values are indicated (in blue for o BA.1). **(F)** Competition ELISA graphs showing the binding of biotinylated RBD proteins from SARS-CoV-2 o BA.1 and BA.2 variants to soluble ACE2 ectodomain in presence of Cv2.1169 and Cv2.3194 antibodies as competitors. Means ± SD of duplicate values are shown. **(G)** Same as in E but for Cv2.1169 and Cv2.3194 against BA.2. Error bars indicate the SD of duplicate values. **(H)** Graphs comparing the ELISA binding of monomeric and dimeric Cv2.1169 IgA antibodies to the RBD proteins of SARS-CoV-2 o BA.1 and BA.2 variants. Means ± SD of duplicate values are shown. n.dIgA, normalized values according to the number of binding sites. **(I)** Same as in F but for Wuhan and o BA.1 tri-S proteins with monomeric and dimeric Cv2.1169 IgA antibodies. Means ± SD of duplicate values are shown. n.dIgA, normalized values according to the number of binding sites. **(J)** Same as in G but for Cv2.1169 IgA monomers and J-chain dimers (dIgA) against BA.1 and BA.2. Error bars indicate the SD of duplicate values. Heatmap (right) presents the IC_{50} values calculated from the curves (left). n.dIgA, normalized values according to the number of binding sites.

(Fig. 4, E–G; and Fig. S4 A). The RBD residue T478 forms hydrogen bonds with Cv2.1169 heavy and light chains and is mutated in the δ and δ+ variants (T478K; Fig. 9 D and Table S5). Despite this substitution, Cv2.1169 is still able to efficiently bind and neutralize both variants (Fig. 4, E–G; Fig. 6 C; and Fig. S4, A and B). This indicates that the interface integrity does not depend on the hydrogen bonds formed with the T478 side chain and that there is enough space for the lysine residue to adopt a rotamer with reduced clashes with the antibody. Unlike the Cv2.6264 antibody, which also straddles the RBD ridge but lost

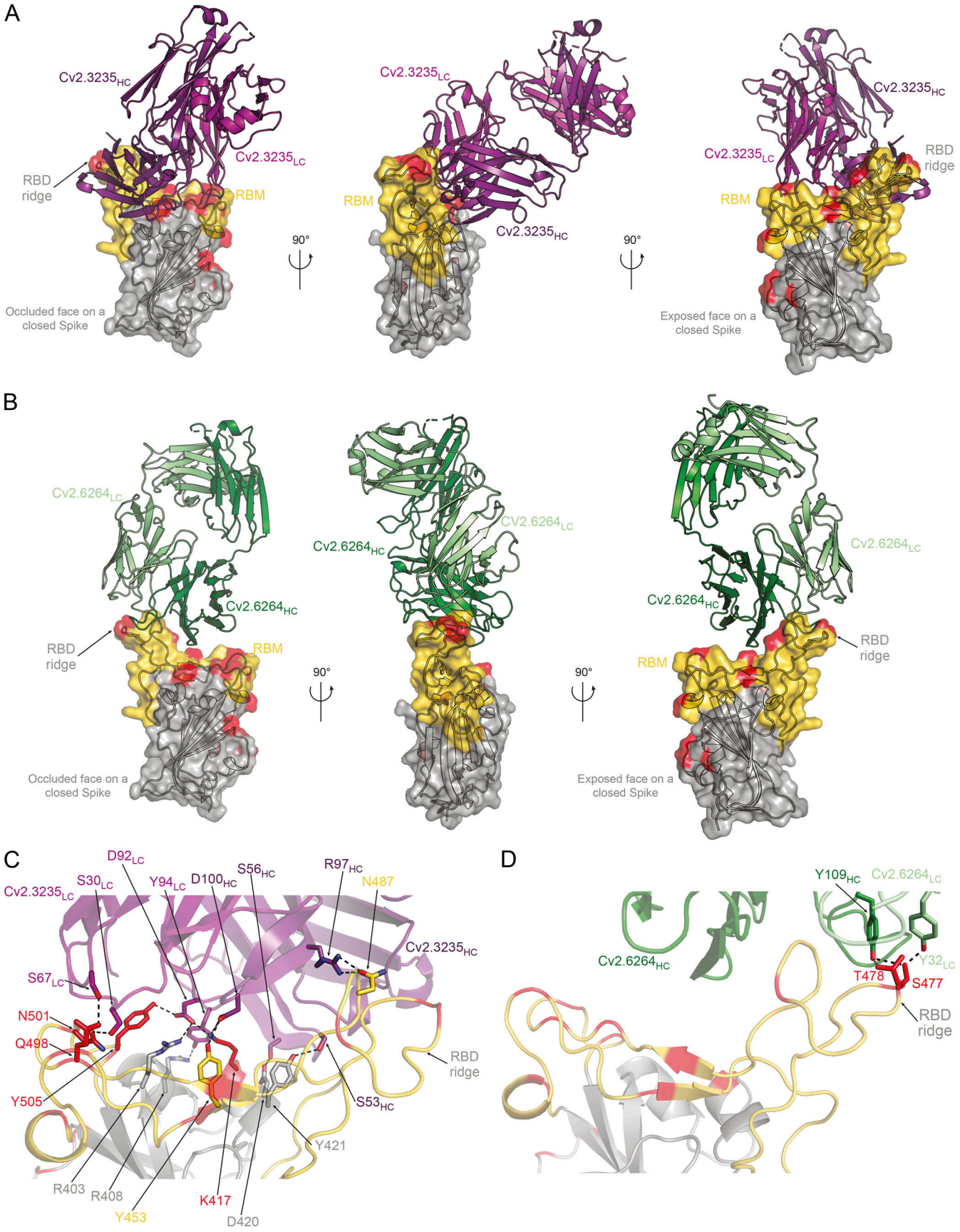

Figure 8. **Structural analyses of the RBD-Cv2.3235 and RBD-Cv2.6264 complexes. (A)** Crystal structure of the complex formed by the RBD and Cv2.3235 Fab (PDB ID: 7QF0). The RBD is represented in cartoon with a transparent gray surface, highlighting the RBM (yellow), and residues that are mutated in the

VOCs (red). **(B)** Same as in A but for the RBD-Cv2.6264 complex (PDB ID: 7QF1). **(C)** Polar interactions (dashed lines) formed at the interface of the RBD-Cv2.3235 complex. For simplicity, only the interactions that involve side chains on both proteins are represented. **(D)** Same as in C but for the RBD-Cv2.6264 complex.

reactivity against the δ and δ⁺ variants (Fig. 4, E–G; and Fig. 8, B and D), Cv2.1169 buries the RBD F486 within a hydrophobic cavity. This pocket is formed by aromatic residues of the FWR_H2 (W50), the CDR_H3 (F110), the CDR_L1 (Y33), and the CDR_L3 (Y92 and W97; Fig. 9 D), and mimics the environment encountered when interacting with ACE2 (Lan et al., 2020). Thus, the F486 residue likely acts as an anchor for Cv2.1169, strengthening its interaction with the RBM and allowing it to tolerate the T478K mutation in the δ and δ⁺ variants. Four of the Cv2.1169-RBD contacting residues are mutated in BA.1 and BA.2 variants, including the substitution K417N already present in β and γ, and T478K in δ, as well as two Omicron-specific mutations S477N and Q493R (Table S5). Although all of them are at the periphery of the Cv2.1169-binding site (Fig. 9, A, C, and D), their combination explains the decreased binding and neutralization of SARS-CoV-2 BA.1 and BA.2 compared with the other VOCs (Fig. 7).

As aforementioned, Cv2.1169 leans toward the RBD's occluded face, making the epitope inaccessible on the "down" conformation (Fig. 9 E), which implies that the antibody binds only to the RBD in its "up" conformation. This was confirmed by the 2.8 Å cryo-EM reconstruction of the SARS-CoV-2 S_6P protein trimer in a complex with Cv2.1169 IgA Fab (See Data S1 for the cryo-EM processing strategy). The map showed that the spike is in the open form with each protomer bound by a Cv2.1169 Fab (Fig. 9 F). Considering that Cv2.1169 blocked SARS-CoV-2 tri-S binding to soluble ACE2 receptor and that its binding site is only accessible in the up-RBD conformation, our data suggest that the antibody belongs to the class 1 category (or Ia; Barnes et al., 2020b), with an epitope in the RBD-B group (Yuan et al., 2021). Accordingly, Cv2.1169 cross-competed for binding to spike and RBD proteins with class 1 benchmarked SARS-CoV-2 neutralizers (CT-P59, COV2-2196, REGN10933, and CB6), but also moderately with class 2 antibody LY-CoV555 (Fig. 6 D).

In vivo therapeutic activity of Cv2.1169 against SARS-CoV-2 infection

We evaluated the in vivo therapeutic potential of neutralizing antibody Cv2.1169 using first the K18-hACE2 transgenic mouse model for SARS-CoV-2 (D614G strain) infection. Mice infected i.n. with 10^4 PFU of SARS-CoV-2 were treated 6 h later with a single i.p. injection of Cv2.1169 IgG antibody (0.25 mg, ∼10 mg/kg and 0.5 mg, ∼20 mg/kg) or control IgG antibody (0.5 mg, ∼20 mg/kg; Fig. 10 A). Infected mice from the control group lost up to 25% of their body weight within the first 6 d post-infection (dpi) before reaching humane endpoints at 7–8 dpi (Fig. 10 A). In contrast, all animals treated with Cv2.1169 IgG survived and recovered their initial body weight after experiencing a transient loss during the first week (Fig. 10 A). Even when infected with a higher viral inoculum (10^5 PFU SARS-CoV-2) and treated 22 h after infection with Cv2.1169 IgG (∼40 mg/kg i.p. plus i.n.), half of the mice survived compared with those in the control group (P = 0.029; Fig. 10 B). Next, to evaluate the in vivo efficacy of Cv2.1169 IgA antibodies, a single low dose of either Cv2.1169 IgA or IgG antibodies (0.125 mg i.p., ∼5 mg/kg) was administered to SARS-CoV-2–infected mice (10^4 PFU challenge dose). Despite a significant and comparable reduction of viral loads in the oral swabs of Cv2.1169 IgA- and IgG-treated mice compared with control animals at 4 dpi (2.6×10^4 equivalent PFU [eqPFU]/ml vs. 5.7×10^3 eqPFU/ml for Cv2.1169 IgA [P = 0.008], and 4.7×10^3 eqPFU/ml for Cv2.1169 IgG [P = 0.029]; Fig. S5 A), all mice treated with the SARS-CoV-2 IgAs were euthanized at 7–8 dpi, whereas 75% of the Cv2-1169 IgG-treated mice lost weight and developed symptoms but recovered their initial body weight after 2 wk (Fig. 10 C). This can be explained by the rapid decay of circulating human IgA as compared with IgG antibodies in mice (Fig. S5 C).

SARS-CoV-2–related pathogenesis in infected Golden Syrian hamsters resembles mild-to-moderate COVID-19 disease in humans (Imai et al., 2020; Sia et al., 2020). To further evaluate the in vivo efficacy of Cv2.1169 IgG neutralizer, hamsters infected i.n. with 6.10^4 PFU of SARS-CoV-2 were treated 24 h later with a single injection of Cv2.1169 IgG or control antibodies (1 mg i.p., ∼10 mg/kg; Fig. 10 D). Lung weight to body weight (LW/BW) ratio, intra-lung viral infectivity, and RNA load were measured at 5 dpi. Both pulmonary viral infectivity and RNA levels in hamsters treated with Cv2.1169 were significantly reduced compared with the control animals (2.44×10^3 vs. 10×10^5 PFU/lung, P = 0.0005 and 4.3×10^7 vs. 3.4×10^8 copies/µg RNA, P = 0.013, respectively; Fig. 10 D). We next compared the in vivo activity of Cv2.1169 IgG and IgA antibodies at a dose ∼5 mg/kg in hamsters 4 h after infection. IgA- and IgG-treated hamsters showed a reduction in LW/BW ratio compared with the control animals (1.64 vs. 1.4 for IgA [P = 0.03] and 1.32 for IgG [P = 0.004]; Fig. 10 E). As expected from the rapid disappearance of circulating human IgA antibodies in treated animals (Fig. S5 E), the intra-lung viral infectivity and RNA loads were comparable between SARS-CoV-2–neutralizing IgA–treated and control hamsters (Fig. 10 E). In contrast, the administration of Cv2.1169 IgG antibodies reduced both SARS-CoV-2 infectivity and RNA levels in the lungs of treated hamsters (1.39×10^6 vs. 80 PFU/lung, P = 0.0002; 6.14×10^8 vs. 1.51×10^8 copies/µg RNA, P = 0.028; Fig. 10 E). Cv2.1169 IgA and IgG-treated animals showed similar endogenous anti-spike IgG titers, which were reduced as compared to the control group (P < 0.0001 and P = 0.0003, respectively), suggesting potential early antiviral effects of Cv2.1169 IgA antibodies against SARS-CoV-2 infection (Fig. S5 F).

To determine whether Cv2.1169 is active in vivo against infection with SARS-CoV-2 VOCs, we tested the prophylactic activity of Cv2.1169 IgA antibodies and the therapeutic activity of Cv2.1169 IgG antibodies against SARS-CoV-2 VOC Beta in K18-hACE2 transgenic mice. A single administration of Cv2.1169 IgA antibodies at ∼10 mg/kg (0.25 mg i.p.) 6 h prior to infection with

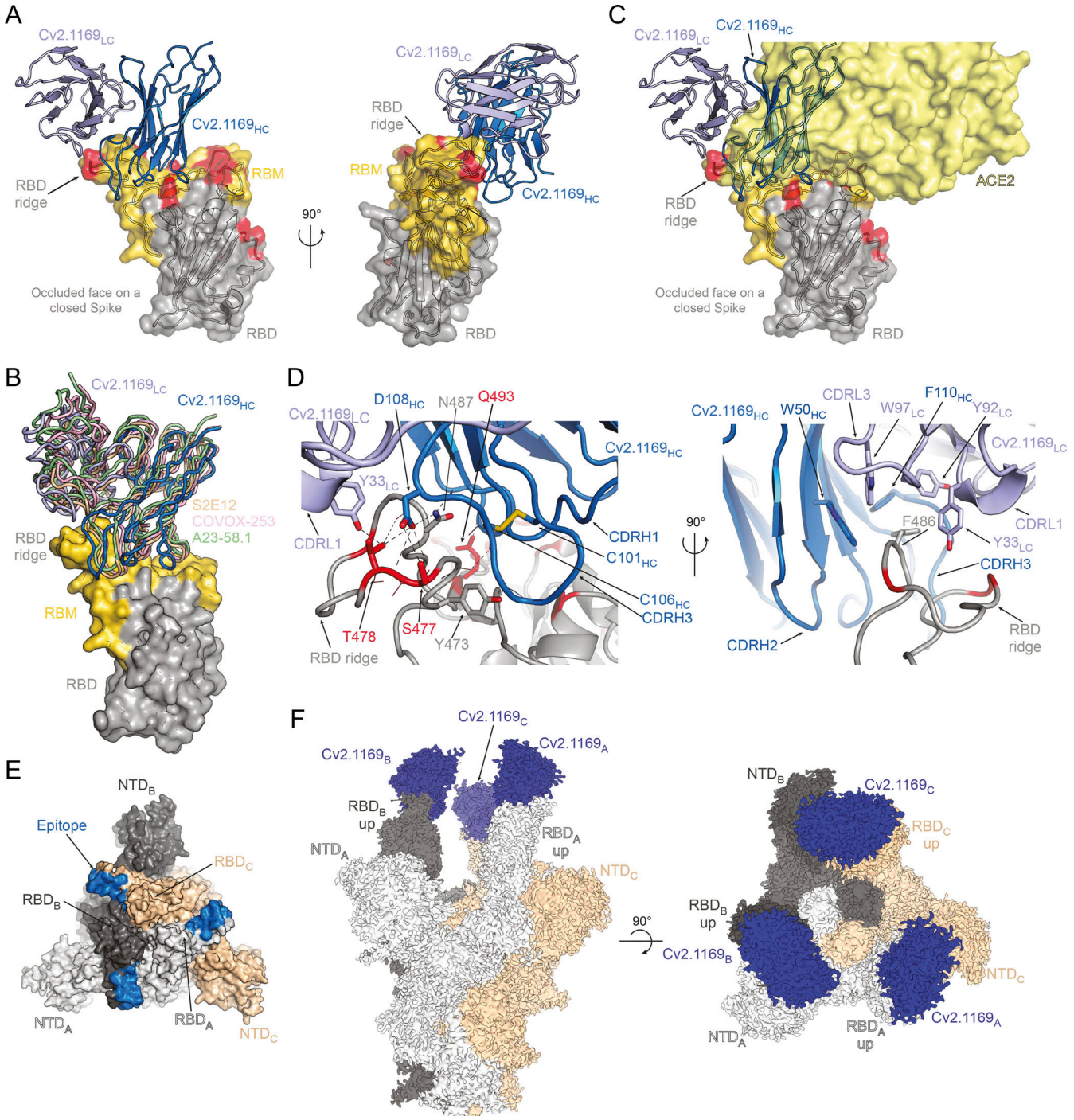

Figure 9. **Structural analyses of the Cv2.1169 epitope. (A)** Crystal structure of the complex formed by the RBD and Cv2.1169 (PDB ID: 7QEV). The RBD is represented in cartoon with a transparent surface, highlighting the RBM (yellow) and residues that are mutated in the VOCs (red). The constant domain from Cv2.1169 could not be built on the residual electron density and the variable domains are indicated in different shades of blue (IgH, dark blue; IgL, light blue). **(B)** Superposition of the RBD-Cv2.1169 crystal structure with the complexes formed by other V_H1-58-encoded antibodies (S2E12 [PDB ID: 7R6X], COVOX-253 [PDB ID: 7BEN] and A23-58.1 [PDB ID: 7LRS]). **(C)** Superposition of the RBD-Cv2.1169 and RBD-ACE2 (PDB ID: 6M0J) structures, showing the ACE2 receptor on surface representation (light yellow) and its clashes with the antibody. **(D)** Close-up at the RBD-Cv2.1169 interface. For clarity, only the side chains from residues forming hydrogen bonds (dashed lines) are shown as sticks. Residues mutated in the VOCs are in red and the CDR_H3 disulfide bond is indicated with yellow sticks (left). Details of the hydrophobic residues that anchor F486 at the interface between the light and heavy chains of Cv2.1169 (right). **(E)** Identification of the Cv2.1169 epitope (blue) on the structure of a closed spike (PDB ID: 6VXX). The different protomers are identified with a subscript letter and colored in light gray (protomer A), dark gray (protomer B), and wheat (protomer C). **(F)** Cryo-EM map from the tri-S ectodomain in complex with Cv2.1169 (EMDB ID: EMD-14853).

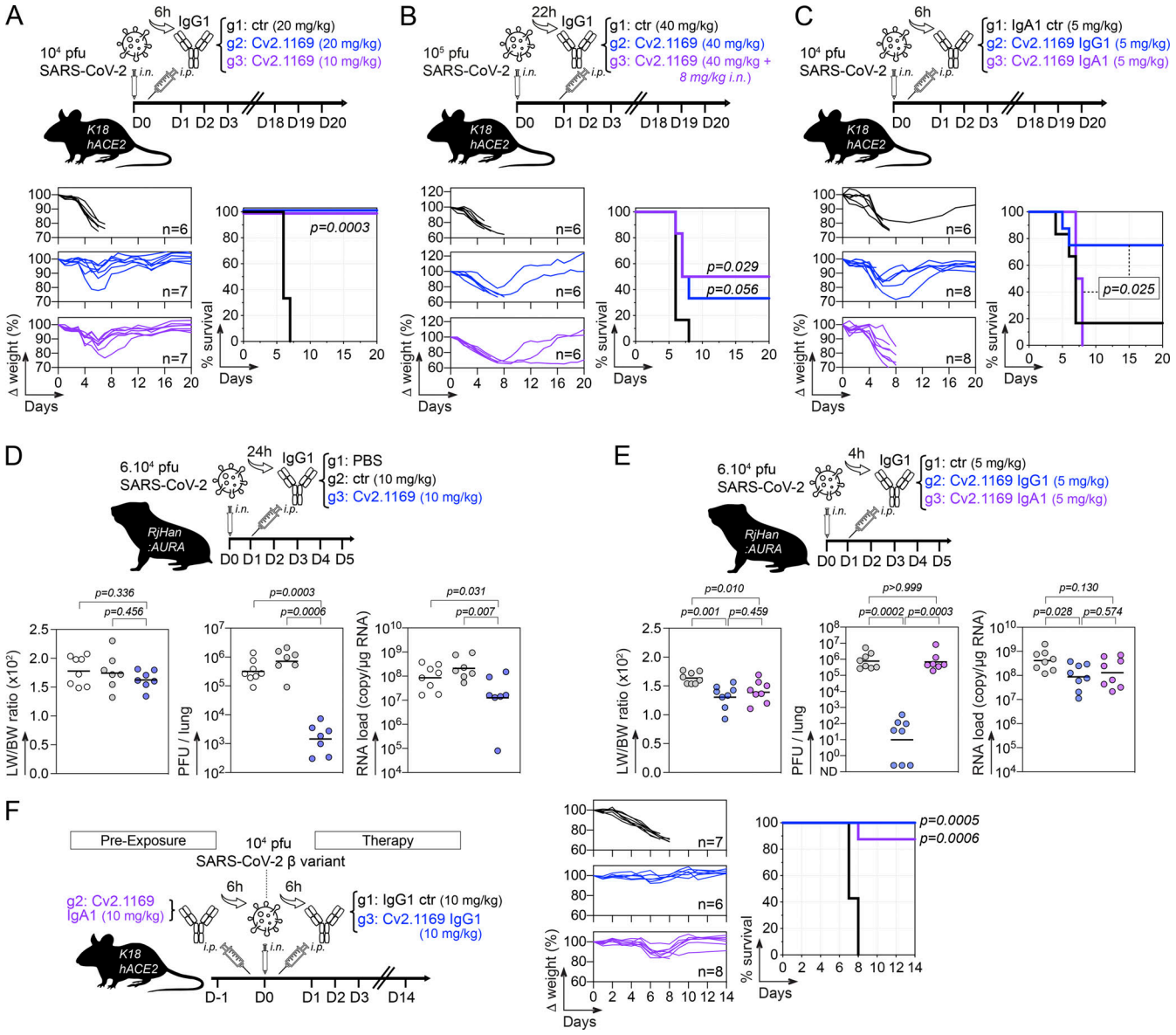

Figure 10. **In vivo therapeutic activity of potent SARS-CoV-2 neutralizer Cv2.1169. (A)** Schematic diagram showing the experimental design of Cv2.1169 antibody therapy in SARS-CoV-2–infected K18-hACE2 mice (top). Animals were infected i.n. with 10^4 PFU of SARS-CoV-2 and 6 h later received an i.p. injection of Cv2.1169 or isotypic control IgG antibody at ∼10 mg/kg (0.25 mg) and ∼20 mg/kg (0.5 mg). Graphs showing the evolution of initial body weight (% Δ weight, bottom left) and survival rate (bottom right) in animal groups. Groups of mice were compared in the Kaplan-Meier analysis using log-rank Mantel-Cox test. **(B)** Same as in A but with K18-hACE2 mice infected with 10^5 PFU and treated 22 h later with 1 mg i.p. of Cv2.1169 IgG antibody (∼40 mg/kg). **(C)** Same as in A but with infected mice treated with Cv2.1169 IgG and IgA antibodies at ∼5 mg/kg (0.125 mg). **(D)** Schematic diagram shows the experimental design of Cv2.1169 antibody therapy in SARS-CoV-2–infected golden Syrian hamsters (top). Animals (seven or eight per group) were infected i.n. with 6 × 10^4 PFU of SARS-CoV-2 and 24 h later received an i.p. injection of PBS, Cv2.1169 or isotypic control IgG antibody at ∼10 mg/kg (1 mg). Dot plots showing LW/BW ratio × 100 (left), infectivity (center), and RNA load (right) measured in animal groups at 5 dpi. Groups of hamsters were compared using two-tailed Mann-Whitney test. **(E)** Same as in D but with infected animals treated 4 h later with Cv2.1169 IgG and IgA antibodies at ∼5 mg/kg (0.5 mg). **(F)** Same as in A but with K18-hACE2 mice infected with 10^4 PFU of the SARS-CoV-2 variant β (B.1.351), and either pre-treated 6 h before infection with ∼10 mg/kg (0.25 mg) of Cv2.1169 IgA or treated 6 h after infection with ∼10 mg/kg (0.25 mg) of Cv2.1169 IgG or isotype control (ctr).

10^4 PFU of SARS-CoV-2 Beta protected 87.5% of the animals from death (Fig. 10 F). Despite the fact that human SARS-CoV-2 IgA antibodies did not persist in the mouse circulation (Fig. S5 C), Cv2.1169 IgA-treated mice also recovered their initial body weight during the follow-up (Fig. 10 F). Likewise, treating once SARS-CoV-2 Beta–infected mice with Cv2.1169 IgG antibodies (0.25 mg i.p., ∼10 mg/kg) 6 h after infection led to 100% survival, while all animals receiving the control antibodies were euthanized at 7–8 dpi (Fig. 10 F). Of note, human Cv2.1169 IgG antibodies were still detectable in mouse sera at the end of the follow-up (Fig. S5, B and C). In addition, mice pre-treated with Cv2.1169 IgAs developed higher anti-spike IgG antibody titers as compared to those treated with Cv2.1169 IgG antibodies, suggesting a weaker viral control in the former group (Fig. S5 D).

Discussion

SARS-CoV-2 infection triggers the production of high-affinity IgGs and IgAs to the viral spike, including neutralizing antibodies, released in mucosal secretions and circulating in the blood (Smith et al., 2021; Sterlin et al., 2021). Class-switched IgG and IgA memory B cells are also elicited during COVID-19, persist for months after infection, and can continue to mature and expand upon antigenic challenges (Gaebler et al., 2021; Sokal et al., 2021; Wang et al., 2021c). In line with previous reports (Sterlin et al., 2021; Zhou et al., 2021b), we found that serum IgA antibodies from COVID-19 convalescents neutralize SARS-CoV-2, often more efficiently than their IgG counterparts despite their lower representativeness in the blood. IgA-neutralizing titers were correlated to anti-S1/-RBD antibody levels and spike$^+$ memory IgA B-cell frequencies, suggesting coordinated serological and cellular humoral responses in these individuals as previously reported (Juno et al., 2020). We also document an association between spike-reactive resting memory IgG B cells and Th2-like cTfh cells, which likely encompass spike-specific cTfh2 cells (Juno et al., 2020). In this study, we characterized SARS-CoV-2 spike–specific IgG$^+$ and IgA$^+$ memory B-cell antibodies from COVID-19 convalescent individuals with high seroneutralization titers. Surprisingly, only a minority (~7%) of the antibodies—all targeting the RBD—efficiently neutralized SARS-CoV-2 in vitro. Other less potent anti-RBD and several anti-NTD antibodies neutralizing SARS-CoV-2 were also isolated, as previously reported (Andreano et al., 2021; Brouwer et al., 2020; Chi et al., 2020; Liu et al., 2020; Robbiani et al., 2020; Wec et al., 2020; Zost et al., 2020b).

Besides neutralization, SARS-CoV-2 IgGs can exert antiviral effector functions dependent or not on their binding to FcγR (i.e., ADCC/ADCP and CDC, respectively), playing a role in the therapeutic protection against SARS-CoV-2 infection in vivo (Schäfer et al., 2021; Winkler et al., 2021). Here, we found that despite lacking high neutralization potential, anti-S2 and anti-NTD IgGs harbor strong Fc-dependent effector functions less frequently observed with anti-RBD antibodies. This tendency suggests a dichotomy of antiviral functions based on epitope specificity, with antibodies to the spike head (RBD) being neutralizers and those to the stalk (S2) being effectors, while anti-NTD displayed mixed activities. Of note, one neutralizing antibody termed S2P6 targeting the S2 stem helix peptide also mediates a strong ADCC activity (Pinto et al., 2021).

Among the 102 SARS-CoV-2 antibodies described in this study, Cv2.1169 and Cv2.3194 were the sole potent neutralizers with a sustained activity against all SARS-CoV-2 variants, including Omicron BA.1 and BA.2 subtypes. Comparably to typical class 1 anti-RBD antibodies, Cv2.3194 uses V_H3-53 variable genes and displays a short CDR_H3 (Yuan et al., 2020, 2021), but differs from the others by its resistance to escape mutations in the VOCs. Indeed, V_H3-53–encoded anti-RBD antibodies usually lose their capacity to neutralize SARS-CoV-2 viruses with mutations in positions K417 and N501, including the VOCs α, β, γ, and ο (Yuan et al., 2021; Zhou et al., 2021a). A rare mutation in the CDRκ1 of Vκ3-20–expressing class 1 anti-RBD antibodies (P30S) has been proposed to rescue VOC neutralization (Dejnirattisai et al., 2021a), but is absent in Cv2.3194. As the Cv2.3194 Fab/RBD complex did not crystallize, the molecular basis for its unaltered potent cross-neutralizing capacity against all VOCs remain to be solved. The other potent SARS-CoV-2–cross-neutralizing antibody, Cv2.1169, is a class 1 neutralizer binding to RBD with a modest total buried surface area. Except for Omicron BA.1 and BA.2, all mutated RBD residues in the SARS-CoV-2 VOCs had a negligible impact on the SARS-CoV-2 binding and neutralizing capacity of Cv2.1169. Based on structural data analysis, we identified the RBM residues in positions F486 and N487 as critical for Cv2.1169 binding, acting as anchors that can accommodate the T478K mutation present in several VOCs. Importantly, as previously shown for V_H1-58-class antibody S2E12, substitutions in positions F486 and N487 are unlikely to occur in potential future VOCs because of their deleterious effects in reducing RBD-binding to ACE2 and viral replicative fitness (Starr et al., 2021). Hence, Cv2.1169 belongs to a class of broad SARS-CoV-2 neutralizers (i.e., S2E12, A23.58.1, AZD8895 [COV2-2196]) with a high barrier to viral escape and one of the lowest escapability (Dong et al., 2021; Greaney et al., 2021; Han et al., 2021; Starr et al., 2021; Wang et al., 2021a). Also, the diminished potency of Cv2.1169 against SARS-CoV-2 Omicron appears moderate when compared to other neutralizing antibodies to the RBD "V_H1-58 supersite" that have drastically reduced or lost their activity against BA.1 and BA.2 (Cameroni et al., 2022; Cao et al., 2022a; Cao et al., 2022b *Preprint*). Yet, the F486V mutation presents in the novel Omicron variants BA.4 and B4.5, recently identified in South Africa (Tegally et al., 2022 *Preprint*), may confer an extra viral resistance to neutralization by V_H1-58-class of SARS-CoV-2 bNAbs, including Cv2.1169 (Cao et al., 2022b *Preprint*).

SARS-CoV-2 animal models using rodents and non-human primates have been pivotal in demonstrating the in vivo prophylactic and therapeutic capacity of human neutralizing anti-spike antibodies (Noy-Porat et al., 2021; Rogers et al., 2020; Rosenfeld et al., 2021). We show that Cv2.1169 IgG efficiently prevents and/or protects animals from infection with SARS-CoV-2 and its VOC Beta. Cv2.1169 was originally expressed by circulating blood IgA-expressing activated memory B cells, likely developing in mucosal tissues, and we established that Cv2.1169 IgA antibodies can protect mice from SARS-CoV-2 VOC Beta. Hence, one can assume that such antibodies if locally present at mucosal surfaces, particularly as dimeric IgAs, could efficiently neutralize and/or eliminate virions and therefore, potentially diminish the risk of infection by SARS-CoV-2 variants. In this regard, a longer hinge region and multivalency of IgA1 antibody dimers allow enhancing SARS-CoV-2 neutralization in vitro as compared with their IgG1 counterparts (Sun et al., 2021; Wang et al., 2021b). In line with this, we found that the loss of neutralization activity of Cv2.1169 against BA.1 and BA.2 was greatly rescued by the avidity effects of the antibody produced in its dimeric IgA form.

Several escape mutations in the spike of SARS-CoV-2 variants caused resistance to antibody neutralization, compromising vaccine and therapeutic antibody efficacy (Cameroni et al., 2022; Pinto et al., 2021; Planas et al., 2021b, Planas et al., 2021a). Remarkably, Cv2.1169 and Cv2.3194 demonstrated a broad activity, neutralizing not only VOCs Alpha, Beta, Gamma, Delta,

and Delta+, but also BA.1 and BA.2, and ranked as the most potent cross-neutralizer when compared with benchmarked antibodies used in clinics. Adjunct to its neutralizing activity, the strong ADCP potential of Cv2.1169 IgG antibodies could contribute to eliminating cell-free and cell-associated virions and stimulating adaptive immunity via vaccinal effects (Corti et al., 2021). Taking into account the healthcare benefits afforded by antibody therapies to fight COVID-19 (Corti et al., 2021; Singh et al., 2022) and considering the excellent antiviral attributes of Cv2.1169 and Cv2.3194, these two antibodies represent promising candidates for prophylactic and/or therapeutic strategies against COVID-19. Long-acting versions of these broadly SARS-CoV-2–neutralizing antibodies with extended half-life could be used to provide protective immunity in immunocompromised populations (Gentile and Schiano Moriello, 2022).

Materials and methods

Human samples

Blood samples from Wuhan COVID-19 convalescent donors were obtained as part of the CORSER and French COVID cohorts in accordance with and after ethical approval from all the French legislation and regulation authorities. The CORSER study was registered with ClinicalTrials.gov (NCT04325646) and received ethical approval from the Comité de Protection des Personnes Ile de France III. The French COVID study was approved by the regional investigational review board (Comité de Protection des Personnes Ile-de-France VII, Paris, France) and performed according to the European guidelines and the Declaration of Helsinki. All participants gave written consent to participate in this study, and data were collected under pseudo-anonymized conditions using subject coding.

Serum IgG and IgA purification

All human sera were heat-inactivated at 56°C for 60 min. Human IgG and IgA antibodies were purified from donors' sera by affinity chromatography using Protein G Sepharose 4 Fast Flow (GE Healthcare) and peptide M-coupled agarose beads (Invivogen), respectively. Purified serum antibodies were dialyzed against PBS using Slide-A-Lyzer Cassettes (10K MWCO; Thermo Fisher Scientific).

Viruses

SARS-CoV-2 BetaCoV/France/IDF0372/2020 (GISAID ID: EPI_ISL_406596) and D614G (hCoV-19/France/GE1973/2020; GISAID ID: EPI_ISL_414631) strains were supplied by the National Reference Centre for Respiratory Viruses (Institut Pasteur; Grzelak et al., 2020; Planas et al., 2021a). α (B.1.1.7; GISAID ID: EPI_ISL_735391), β (B.1.351; GISAID ID: EPI_ISL_964916), δ (B.1.617.2; GISAID ID: EPI_ISL_2029113), o BA.1 (GISAID ID: EPI_ISL_6794907) and BA.2 strains were provided by the Virus and Immunity Unit (Institut Pasteur; Planas et al., 2021a, 2021b, 2022; Bruel et al., 2022). The γ variant (P.1.; hCoV-19/Japan/TY7-501/2021; GISAID ID: EPI_ISL_833366) was obtained from Global Health security action group Laboratory Network (Betton et al., 2021). The Beta strain (β, B.1.351; hcoV-19/France/IDF-IPP00078/2021) used for mouse experiments was supplied by the National Reference Centre for Respiratory Viruses (Institut Pasteur). Hamsters were infected with the BetaCoV/France/IDF00372/2020 strain (EVAg collection, Ref-SKU: 014V-03890). Viruses were amplified by one or two passages in Vero E6 cell cultures and titrated. The sequence of the viral stocks was verified by RNAseq. All work with infectious virus was performed in biosafety level 3 containment laboratories at Institut Pasteur.

Expression and purification of viral proteins

Codon-optimized nucleotide fragments encoding stabilized versions of SARS-CoV-2, SARS-CoV-1, MERS-CoV, OC43-CoV, HKU1-CoV, 229E-CoV, NL63-CoV (2P), and BA.1 spike (HexaPro; S_6P; S) ectodomains, and SARS-CoV-2 S2 domain, followed by a Foldon trimerization motif and C-terminal tags (8xHis-tag, Strep-tag, and AviTag) were synthesized and cloned into pcDNA3.1/Zeo(+) expression vector (Thermo Fisher Scientific). For competition ELISA experiments, a SARS-CoV-2 S ectodomain DNA sequence without the StrepTag was also cloned into pcDNA3.1/Zeo(+) vector. Synthetic nucleotide fragments coding for Wuhan SARS-CoV-2 RBD, S1 subunit, S1 NTD, S1 CD, nucleocapsid protein (N), BA.1 and BA.2 RBDs followed by C-terminal tags (8xHis-tag, Strep-tag, and AviTag), as well as human ACE2 (plus 8xHis- and Strep-tags) were cloned into the pcDNA3.1/Zeo(+) vector. For SARS-CoV-2 RBD variant proteins, mutations (N501Y for the α variant; K417N, E484K, and N501Y for the β variant; K471T, E484K, and N501Y for the γ variant; L452R and T478K for the δ variant, K417N, L452R, and T478K for the δ+ variant; L452R and E484Q for the κ variant) were introduced using the QuickChange Site-Directed Mutagenesis kit (Agilent Technologies) following the manufacturer's instructions. Glycoproteins were produced by transient transfection of exponentially growing Freestyle 293-F suspension cells (Thermo Fisher Scientific) using polyethylenimine (PEI) precipitation method, as previously described (Lorin and Mouquet, 2015). Proteins were purified from culture supernatants by high-performance chromatography using the Ni Sepharose Excel Resin according to the manufacturer's instructions (GE Healthcare), dialyzed against PBS using Slide-A-Lyzer dialysis cassettes (Thermo Fisher Scientific), quantified using NanoDrop 2000 instrument (Thermo Fisher Scientific), and controlled for purity by SDS-PAGE using NuPAGE 3–8% Tris-acetate gels (Life Technologies), as previously described (Lorin and Mouquet, 2015). AviTagged tri-S and RBD proteins were biotinylated using BirA biotin–protein ligase bulk reaction kit (Avidity) or Enzymatic Protein Biotinylation Kit (Sigma-Aldrich). Wuhan SARS-CoV-2 RDB protein was also coupled to DyLight 650 using the DyLight Amine-Reactive Dyes kit (Thermo Fisher Scientific).

For crystallographic experiments, a codon-optimized nucleotide fragment encoding the SARS-CoV-2 RBD protein (residues 331–528), followed by an enterokinase cleavage site and a C-terminal double strep-tag was cloned into a modified pMT/BiP expression vector (pT350; Invitrogen). Drosophila S2 cells were stably co-transfected with pT350 and pCoPuro (for puromycin selection) plasmids. The cell line was selected and maintained in serum-free insect cell medium (HyClone; Cytiva) supplemented with 7 µg/ml puromycin and 1% penicillin/streptomycin antibiotics. Cells were grown to reach a density of 1×10^7 cells/ml,

and protein expression was then induced with 4 µM $CdCl_2$. After 6 d of culture, the supernatant was collected, concentrated, and the proteins were purified by high-performance chromatography using a Streptactin column (IBA). The eluate was buffer-exchanged into 10 mM Tris-HCl (pH 8.0), 100 mM NaCl, and 2 mM $CaCl_2$ using a HiPrep 26/10 Desalting column (GE Healthcare) and subsequently treated with enterokinase overnight at room temperature to remove the strep-tag. Undigested tagged proteins were removed using a Streptactin column, and monomeric untagged protein was purified by size-exclusion chromatography (SEC) using a Superdex 75 column (Cytiva) equilibrated with 10 mM Tris-HCl (pH 8.0), 100 mM NaCl. Purified monomeric untagged protein was concentrated and stored at −80°C until used.

For Cryo-EM experiments, a codon-optimized nucleotide fragment encoding the SARS-CoV-2 spike (S) protein (residues 1–1208) was cloned with its endogenous signal peptide in pcDNA3.1(+) vector and expressed as a stabilized trimeric prefusion construct with six proline substitutions (F817P, A892P, A899P, A942P, K986P, V987P), along with a GSAS substitution at the furin cleavage site (residues 682–685), followed by a Foldon trimerization motif (Hsieh et al., 2020), and C-terminal tags (8xHis-tag, Strep-tag, and AviTag). The recombinant protein, S_6P, was produced by transient transfection of Expi293F cells (Thermo Fisher Scientific) using FectroPRO DNA transfection reagent (Polyplus), according to the manufacturer's instructions. After 5 d of culture, recombinant proteins were purified from the concentrated supernatant by affinity chromatography using a SrepTactin column (IBA), followed by SEC using a Superose 6 10/300 column (Cytiva) equilibrated in 10 mM Tris-HCl and 100 mM NaCl (pH 8.0). The peak corresponding to the trimeric protein was concentrated and stored at −80°C until used.

Flow cytometry immunophenotyping

PBMCs were isolated from donors' blood using Ficoll Plaque Plus (GE Healthcare). Human blood B cells and cTfh were analyzed using two different fluorescently labeled antibody cocktails. For B-cell phenotyping, B cells were first isolated from donors' PBMCs by MACS using human CD19 MicroBeads (Miltenyi Biotec). $CD19^+$ B cells were then stained using LIVE/DEAD aqua fixable dead cell stain kit (Molecular Probes; Thermo Fisher Scientific) to exclude dead cells. B cells were incubated for 30 min at 4°C with biotinylated tri-S and DyLight 650–coupled RBD, washed once with 1% FBS-PBS (FACS buffer), and incubated for 30 min at 4°C with a cocktail of mouse anti-human antibodies: CD19 Alexa 700 (HIB19; BD Biosciences), CD21 BV421 (B-ly4; BD Biosciences), CD27 PE-CF594 (M-T271; BD Biosciences), IgG BV786 (G18-145; BD Biosciences), IgA FITC (IS11-8E10; Miltenyi Biotec), Integrin β7 BUV395 (FIB504; BD Biosciences), and streptavidin R-PE conjugate (Invitrogen; Thermo Fisher Scientific). Cells were then washed and resuspended in FACS buffer. Following a lymphocyte and single-cell gating, live cells were gated on $CD19^+$ B cells. FACS analyses were performed using a FACS Aria Fusion Cell Sorter (Becton Dickinson) and FlowJo software (v10.3; FlowJo LLC). Immunophenotyping of cTfh cell subsets was performed on negative fractions from the CD19 MACS. The cTfh antibody panel included: CD3 BV605 (SK7), CD4 PE-CF594 (RPA-T4), CD185/CXCR5 AF-488 (RF8B2), CD183/CXCR3 PE-Cy5 (1C6/CXCR3), CD196/CCR6 PE-Cy7 (11A9), CD197/CCR7 AF647 (3D12; BD Biosciences), CD279/PD1 BV421 (EH12.2H7; BioLegend), and CD278/ICOS PE (ISA-3; Thermo Fisher Scientific). Cells were stained as described above, washed, and fixed in 1% paraformaldehyde-PBS. Following a lymphocyte and single-cell gating, dead cells were excluded. Flow cytometric analyses of stained cells were performed using a BD LSR Fortessa instrument (BD Biosciences), and the FlowJo software (v10.6; FlowJo LLC).

Single B-cell FACS sorting and expression-cloning of antibodies

Peripheral blood human B cells were isolated and stained as described above. Single SARS-CoV-2 S^+ IgG^+ and IgA^+ B cells were sorted into 96-well PCR plates using a FACS Aria Fusion Cell Sorter (Becton Dickinson), as previously described (Tiller et al., 2008). Single-cell cDNA synthesis using SuperScript IV reverse transcriptase (Thermo Fisher Scientific) followed by nested-PCR amplifications of IgH, Igκ, and Igλ genes, and sequences analyses for Ig gene features were performed as previously described (Prigent et al., 2016; Tiller et al., 2008). Purified digested PCR products were cloned into human Igγ1-, Igκ-, or Igλ-expressing vectors (GenBank# LT615368.1, LT615369.1, and LT615370.1, respectively), as previously described (Tiller et al., 2008). Cv2.1169 were also cloned into human $Igγ1^{NA}$, $Igγ1^{LALA}$ (N297A and L234A/L235A mutations introduced by site-directed mutagenesis [QuickChange; Agilent Technologies]), Igα1 and Fab-Igα1-expressing vectors (Lorin and Mouquet, 2015; Lorin et al., 2022). Cv2.3235 and Cv2.6264 IgH were also cloned into a human Fab-Igγ1–expressing vector (Mouquet et al., 2012). Recombinant antibodies were produced by transient co-transfection of Freestyle 293-F suspension cells (Thermo Fisher Scientific) using the PEI precipitation method, as previously described (Lorin and Mouquet, 2015). The dimeric form of Cv2.1169 IgA1 was produced by co-transfection of Freestyle 293-F cells with a human J chain pcDNA3.1/Zeo(+) vector as previously described (Lorin and Mouquet, 2015). Recombinant human IgG, IgA antibodies, and Fab were purified by affinity chromatography using Protein G Sepharose 4 Fast Flow (GE Healthcare), peptide M-coupled agarose beads (Invivogen), and Ni Sepharose Excel Resin (GE Healthcare), respectively. Monomeric and dimeric Cv2.1169 IgA1 antibodies were separated by SEC using a Superose 6 Increase 10/300 column (Cytiva). After equilibration of the column with PBS, purified IgA antibodies were injected into the column at a flow rate of 0.3 ml/min. Monomers, dimers, and multimers were separated upon an isocratic elution with 1.2 column volume of PBS. The quality/purity of the different purified fractions was evaluated by SDS-PAGE using 3–8% Tris–Acetate gels (Life Technologies) under non-reducing conditions followed by silver staining (Silver Stain kit; Thermo Fisher Scientific). Purified antibodies were dialyzed against PBS. The purified parental IgG1 antibody versions of benchmarked mAbs (REGN10933, REGN10987 [Hansen et al., 2020], CB6 [Shi et al., 2020], LY-CoV555 [Jones et al., 2021], CT-P59 [Kim et al., 2021], COV2-2196, COV2-2130 [Zost et al., 2020b], ADG-2 [Garrett Rappazzo et al., 2021], and S309 [Pinto et al., 2020]) were prepared as described above after cloning of synthetic DNA fragments (GeneArt; Thermo Fisher Scientific)

coding for the immunoglobulin variable domains. Antibody preparations for in vivo infusions were micro-filtered (Ultrafree-CL devices –0.1 µm PVDF membrane; Merck-Millipore), and checked for endotoxins levels using the ToxinSensor Chromogenic LAL Endotoxin Assay Kit (GenScript).

ELISAs

ELISAs were performed as previously described (Mouquet et al., 2011, 2012). Briefly, high-binding 96-well ELISA plates (Costar; Corning) were coated overnight with 250 ng/well of purified recombinant Coronavirus proteins and 500 ng/well of a SARS-CoV-2 fusion sequence-containing peptide (KRSFIEDLLFNKVTLADAGFIK; GenScript Biotech). After washings with 0.05% Tween 20-PBS (washing buffer), the plates were blocked for 2 h with 2% BSA, 1 mM EDTA, 0.05% Tween 20-PBS (Blocking buffer), washed, and incubated with serially diluted human and rodent sera, purified serum IgA/IgG, or recombinant mAbs in PBS. Total sera were diluted 1:100 (for humans and golden hamsters) or 1:10 (for K18-hACE2 mice) followed by seven consecutive 1:4 dilutions in PBS. Purified serum IgG and IgA antibodies were tested at 50 µg/ml and seven consecutive 1:3 dilutions in PBS. Recombinant IgG1 mAbs were tested at 4 or 10 µg/ml and four to seven consecutive 1:4 dilutions in PBS. Comparative ELISA binding of Cv2.1169 IgG1 and IgA1 antibodies was performed at a concentration of 70 nM and seven consecutive dilutions in PBS. To quantify blood-circulating human Cv2.1169 IgA1 and IgG1 in treated K18-hACE2 mice and golden hamsters, high-binding 96-well ELISA plates (Costar; Corning) were coated overnight with 250 ng/well of purified goat anti-human IgA or IgG antibody (Jackson ImmunoResearch; 0.8 µg/ml final). After washings, plates were blocked, washed, and incubated for 2 h with 1:100 diluted sera from K18-hACE2 mice and golden hamster and seven consecutive 1:3 dilutions in PBS. Cv2.1169 IgA1 or IgG1 antibody at 12 µg/ml and seven consecutive 1:3 dilutions in PBS were used as standards. After washings, the plates were revealed by incubation for 1 h with goat HRP-conjugated anti-mice IgG, anti-golden hamster IgG, anti-human IgG, or anti-human IgA antibodies (Jackson ImmunoResearch; 0.8 µg/ml final) and by adding 100 µl of HRP chromogenic substrate (ABTS solution; Euromedex). Optical densities were measured at 405 nm (OD_{405nm}) and background values given by incubation of PBS alone in coated wells were subtracted. Experiments were performed using HydroSpeed microplate washer and Sunrise microplate absorbance reader (Tecan). For peptide-ELISA, binding of SARS-CoV-2 and control IgG antibodies (at 1 µg/ml) to 5 amino acid–overlapping 15-mer peptides (n = 52; GenScript Biotech, 500 ng/well) was tested using the same procedure as previously described (Mouquet et al., 2011). For competition ELISAs, 250 ng/well of StrepTag-free tri-S and RBD proteins were coated on ELISA plates (Costar; Corning), which were then blocked, washed, and incubated for 2 h with biotinylated antibodies (at a concentration of 100 ng/ml for tri-S competition and 25 ng/ml for RBD competition) in 1:2 serially diluted solutions of antibody competitors in PBS (IgG concentration ranging from 0.39 to 50 µg/ml). Plates were developed using HRP-conjugated streptavidin (BD Biosciences) as described above. For the competition experiments of tri-S- and RBD-binding to ACE2, ELISA plates (Costar; Corning) were coated overnight with 250 ng/well of purified ACE2 ectodomain. After washings, plates were blocked for 2 h with Blocking buffer, PBST-washed, and incubated with recombinant IgG1 mAbs at 2 µg/ml and seven consecutive 1:2 dilutions in presence of biotinylated tri-S protein at 1 µg/ml in PBS, and at 10 or 100 µg/ml and seven consecutive 1:2 dilutions in PBS in the presence of biotinylated RBD at 0.5 µg/ml. After washings, the plates were revealed by incubation for 30 min with streptavidin HRP-conjugated (BD Biosciences) as described above.

Polyreactivity ELISA was performed as previously described (Planchais et al., 2019). Briefly, high-binding 96-well ELISA plates were coated overnight with 500 ng/well of purified double-stranded DNA, KLH, LPS, Lysozyme, Thyroglobulin, Peptidoglycan from *Bacillus subtilis*, 250 ng/well of insulin (Sigma-Aldrich), flagellin from *B. subtilis* (Invivogen), MAPK14 (Planchais et al., 2019), and 125 ng/well of YU2 HIV-1 Env gp140 protein in PBS. After blocking and washing steps, recombinant IgG mAbs were tested at 4 µg/ml and seven consecutive 1:4 dilutions in PBS. Control antibodies, mGO53 (negative; Wardemann, 2003), and ED38 (high positive; Meffre et al., 2004) were included in each experiment. ELISA binding was developed as described above. HEp-2 ELISA was performed with IgG antibodies at a concentration of 100 µg/ml using the QUANTA Lite ANA ELISA Kit (Inova Diagnostics) following the manufacturer's instructions.

Serum levels of human IL6, IP10, CXCL13, and BAFF were measured using DuoSet ELISA kits (R&D Systems) with undiluted plasma samples.

Flow cytometry binding assays

SARS-CoV-2 specificity validation of cloned human IgG antibodies was performed using the S-Flow assay as previously described (Grzelak et al., 2020). To evaluate spike cross-reactivity, Freestyle 293-F were transfected with pUNO1-Spike-dfur expression vectors (Spike and SpikeV1 to V11 plasmids; Invivogen; 1.2 µg plasmid DNA per 10^6 cells) using PEI-precipitation method. 48 h after transfection, 0.5 × 10^6 transfected and non-transfected control cells were incubated with IgG antibodies for 30 min at 4°C (1 µg/ml). After washings, cells were incubated for 20 min at 4°C with AF647-conjugated goat anti-human IgG antibodies (1:1,000 dilution; Thermo Fisher Scientific) and LIVE/DEAD Fixable Viability dye Aqua (1:1,000 dilution; Thermo Fisher Scientific), washed and resuspended in PBS–paraformaldehyde 1% (Electron Microscopy Sciences). Data were acquired using a CytoFLEX flow cytometer (Beckman Coulter) and analyzed using FlowJo software (v10.7.1; FlowJo LLC). Antibodies were tested in duplicate.

HEp-2 immunofluorescence assay

Recombinant SARS-CoV-2 S-specific and control IgG antibodies (mGO53 and ED38) at 100 µg/ml were analyzed by indirect immunofluorescence assay on HEp-2 cells sections (ANA HEp-2 AeskuSlides; Aesku.Diagnostics) using the kit's controls and FITC-conjugated anti-human IgG antibodies as the tracer according to the manufacturer's instructions. HEp-2 sections were examined using the fluorescence microscope Axio Imager 2 (Zeiss), and pictures were taken at a magnification ×40 with 5,000 ms-acquisition using ZEN imaging software (Zen 2.0 blue version; Zeiss) at the Imagopole platform (Institut Pasteur).

Infrared immunoblotting

Recombinant tri-S protein was heat-denatured at 100°C for 3 min in loading buffer (Invitrogen) containing 1× sample reducing agent (Invitrogen). Denatured tri-S protein (50 µg total) was separated by SDS-PAGE with a NuPAGE 4–12% Bis-Tris Gel (1-well; Invitrogen), electro-transferred onto nitrocellulose membranes, and saturated in PBS-0.05% Tween 20 (PBST)-5% dry milk overnight at 4°C. Membranes were inserted into a Miniblot apparatus (Immunetics) and then incubated with human mAbs (at a concentration of 1 µg/ml) and mouse anti-6xHis antibody (1 µg/ml; BD Biosciences) in PBS-T 5% dry milk in each channel for 2 h. For dot blotting experiments, denatured tri-S (ranging from 0.125 to 2 µg) was immobilized on dry nitrocellulose membranes for 2 h at room temperature and saturated in PBS-0.05% Tween 20 (PBST)-5% dry milk overnight at 4°C. The membranes were then incubated with human mAbs (at a concentration of 1 µg/ml) and mouse anti-6xHis antibody (1 µg/ml; BD Biosciences) in PBS-T 5% dry milk for 2 h. After washing with PBST, membranes were incubated for 1 h with 1/25,000-diluted Alexa Fluor 680-conjugated donkey anti-human IgG (Jackson ImmunoResearch) and 1/25,000-diluted IR Dye 800CW-conjugated goat anti-mouse IgG (LI-COR Biosciences) in PBST-5% dry milk. Finally, membranes were washed and examined with the Odyssey Infrared Imaging system (LI-COR Biosciences).

Protein microarray binding analyses

All experiments were performed at 4°C using ProtoArray Human Protein Microarrays (Thermo Fisher Scientific). Microarrays were blocked for 1 h in blocking solution (Thermo Fisher Scientific), washed, and incubated for 1 h 30 min with IgG antibodies at 2.5 µg/ml as previously described (Planchais et al., 2019). After washings, arrays were incubated for 1 h 30 min with AF647-conjugated goat anti-human IgG antibodies (at 1 µg/ml in PBS; Thermo Fisher Scientific) and revealed using GenePix 4000B microarray scanner (Molecular Devices) and GenePix Pro 6.0 software (Molecular Devices) as previously described (Planchais et al., 2019). Fluorescence intensities were quantified using Spotxel software (SICASYS Software GmbH), and the mean fluorescence intensity (MFI) signals for each antibody (from duplicate protein spots) were plotted against the reference antibody mGO53 (non-polyreactive isotype control) using GraphPad Prism software (v8.1.2; GraphPad Prism Inc.). For each antibody, Z-scores were calculated using ProtoArray Prospector software (v5.2.3; Thermo Fisher Scientific), and deviation (σ) to the diagonal and polyreactivity index (PI) values were calculated as previously described (Planchais et al., 2019). Antibodies were defined as polyreactive when PI >0.21.

Surface plasmon resonance (SPR)

SPR-based technology (Biacore 2000; Biacore) was used to assess the kinetics of interaction of mAbs with SARS-CoV-2 proteins—trimer S, S1, and RBD. Antibodies (Cv2.1169, Cv2.1353, Cv2.3194, Cv2.3235, and Cv2.5213) and ACE2 ectodomain were covalently coupled to CM5 sensor chips (Biacore) using amino-coupling kit (Biacore) according to the manufacturer's procedure. In brief, IgG antibodies and ACE2 protein were diluted in 5 mM maleic acid solution, pH 4 to a final concentration of 10 µg/ml, and injected over sensor surfaces preactivated by a mixture of 1-ethyl-3-(3-dimethylaminopropyl) carbodiimide and N-hydroxysuccinimide. Uncoupled carboxyl groups were blocked by exposure to 1 M solution of ethanolamine.HCl (Biacore). Immobilization densities were 500 RU and 1000 RU for IgG antibodies and ACE2, respectively. All analyses were performed using HBS–EP buffer (10 mM HEPES pH 7.2; 150 mM NaCl; 3 mM EDTA, and 0.005% Tween 20). The flow rate of the buffer during all real-time interaction measurements was set at 30 µl/min. All interactions were performed at a temperature of 25°C. SARS-CoV-2 tri-S and S1 proteins were serially diluted (twofold step) in HBS-EP in the range of 40–0.156 nM. The same range of concentrations was used for RBD with the exception of low-affinity interactions where the concentration range 1,280–10 nM was applied. The association and dissociation phases of the binding of viral proteins to the immobilized antibodies and ACE2 were monitored for 3 and 4 min, respectively. The binding of the proteins to the reference channel containing carboxymethylated dextran only was used as negative control and was subtracted from the binding during data processing. The sensor chip surfaces were regenerated by a 30-s exposure to 4 M solution of guanidine-HCl (Sigma-Aldrich). The evaluation kinetic parameters of the studied interactions were performed by using BIAevaluation version 4.1.1 Software (Biacore).

SARS-CoV-2 S-Fuse neutralization assay

S-Fuse cells (U2OS-ACE2 GFP1-10 or GFP 11 cells) were mixed (ratio 1:1) and plated at a density of 8×10^3 per well in a µClear 96-well plate (Greiner Bio-One) as previously described (Buchrieser et al., 2020). SARS-CoV-2 and VOC viruses (multiplicity of infection, 0.1) were incubated with recombinant IgG1, monomeric, and dimeric IgA1 mAbs at 35 or 7 nM, and 11 consecutive 1:4 dilutions in a culture medium for 30 min at room temperature were added to S-Fuse cells. The cells were fixed 18 h later in 2% paraformaldehyde, washed, and stained with Hoechst stain (dilution 1:1,000; Invitrogen). Images were acquired with an Opera Phenix high-content confocal microscope (Perkin-Elmer). The area displaying GFP expression and the number of nuclei were quantified with Harmony software 4.8 (Perkin-Elmer). The percentage neutralization was calculated from the GFP-positive area as follows: 100 × [1 – (value with IgA/IgG – value in "non-infected")/(value in "no IgA/IgG" – value in "non-infected")]. IC_{50} values were calculated using Prism software (v.9.3.1; GraphPad Prism Inc.) by fitting replicate values using the four-parameter dose–response model (variable slope).

In vitro SARS-CoV-2 pseudoneutralization assay

The SARS-CoV-2 pseudoneutralization assay was performed as previously described (Anna et al., 2021; Grzelak et al., 2020). Briefly, 2×10^4 293T-ACE2-TMPRSS2 were plated in 96-well plates. Purified serum IgA and IgG antibodies were tested at 250 µg/ml and seven consecutive 1:2 dilutions in PBS (or in Penicillin/Streptomycin-containing 10%-FCS DMEM) and then incubated with spike-pseudotyped lentiviral particles for 15–30 min at room temperature before adding to the cells.

Recombinant IgG1, IgA1, or Fab-IgA mAbs were tested at 70 or 350 nM and 11 consecutive 1:3 dilutions in PBS. After a 48 h incubation at 37°C in 5% CO_2, the revelation was performed using the ONE-Glo Luciferase Assay System (Promega), and the luciferase signal was measured with EnSpire Multimode Plate Reader (PerkinElmer). The percentage of neutralization was calculated as follows: 100 × [1 – mean (luciferase signal in sample duplicate)/mean (luciferase signal in virus alone)]. Individual experiments were standardized using Cv2.3235 antibody. IC_{50} values were calculated as described above.

ADCP assay

PBMCs were isolated from healthy donors' blood (Etablissement Français du Sang) using Ficoll Plaque Plus (GE Healthcare). Primary human monocytes were purified from PBMCs by MACS using Whole Blood CD14 MicroBeads (Miltenyi Biotech). Biotinylated-SARS-CoV-2 tri-S proteins were mixed with FITC-labeled NeutrAvidin beads (1 µm; Thermo Fisher Scientific; 1 µg of tri-S for 1 µl of beads) and incubated for 30 min at room temperature. After PBS washings, tri-S coupled-beads 1:500-diluted in DMEM were incubated for 1 h at 37°C with human IgG1 mAbs (at 3 µg/ml). The tri-S-bead-antibody mixtures were then incubated with 7.5 × 10^4 human monocytes for 2 h at 37°C. Following washings with 0.5% BSA and 2 mM EDTA–PBS, cells were fixed with 4% PFA–PBS and analyzed using a CytoFLEX flow cytometer (Beckman Coulter). ADCP assays were performed in two independent experiments and analyzed using the FlowJo software (v10.6; FlowJo LLC). Phagocytic scores were calculated by dividing the fluorescence signals (% FITC-positive cells × geometric MFI FITC-positive cells) given by anti–SARS-CoV-2 spike antibodies by the one of the negative control antibody, mGO53.

ADCC assay

The ADCC activity of anti–SARS-CoV-2 S IgG antibodies was determined using the ADCC Reporter Bioassay (Promega) as previously described (Dufloo et al., 2021). Briefly, 5 × 10^4 Raji-Spike cells were co-cultured with 5 × 10^4 Jurkat-CD16-NFAT-rLuc cells in the presence or absence of SARS-CoV-2 S–specific or control mGO53 IgG antibody at 10 or 50 µg/ml and 10 consecutive 1:2 dilutions in PBS. Luciferase was measured after 18 h of incubation using an EnSpire plate reader (PerkinElmer). ADCC was measured as the fold induction of luciferase activity compared with the control antibody. Experiments were performed in duplicate in two independent experiments.

CDC assay

The CDC activity of anti-SARS-CoV-2 S IgG antibodies was measured using SARS-CoV-2 spike–expressing Raji cells as previously described (Dufloo et al., 2021). Briefly, 5 × 10^4 Raji-Spike cells were cultivated in the presence of 50% normal or heat-inactivated human serum, and with or without IgG antibodies (at 10 or 50 µg/ml and 10 consecutive 1:2 dilutions in PBS). After 24 h, the cells were washed with PBS and incubated for 30 min at 4°C with the live/dead fixable aqua dead cell marker (1:1,000 in PBS; Life Technologies) before fixation. Data were acquired on an Attune NxT instrument (Life Technologies). CDC was calculated using the following formula: 100 × (% of dead cells with serum – % of dead cells without serum)/(100 – % of dead cells without serum). Experiments were performed in duplicate in two independent experiments.

Crystallization and structure determinations

The Fab of anti-SARS-CoV-2 S antibody CR3022 (Ter Meulen et al., 2006) served as a crystallization chaperone molecule and was produced and purified as described above (Single B-cell FACS sorting and expression-cloning of antibodies; Koide, 2009). The purified RBD protein was incubated overnight at 4°C with the Fabs at a RBD–Fab molar ratio of 2:1 (2:1:1 for the ternary complex RBD-Cv2.1169-CR3022). Each binding reaction was loaded onto a Superdex200 column (Cytiva) equilibrated in 10 mM Tris-HCl (pH 8.0) and 100 mM NaCl. The fractions corresponding to the complexes were pooled, concentrated to 9–10 mg/ml, and used in crystallization trials at 18°C using the sitting-drop vapor diffusion method. The RBD-Cv2.2325 Fab complex crystallized with 0.1 M ammonium citrate (pH 7.0) and 12% PEG 3350, while crystals for RBD-Cv2.6264 Fab were obtained with 0.1 M NaAc, 7% PEG 6000, and 30% ethanol. The RBD-Cv2.1169-CR3022 crystals grew in the presence of 6% PEG 8000 and 0.5 M Li_2SO4. Crystals were flash-frozen by immersion into a cryo-protectant containing the crystallization solution supplemented with 30% (vol/vol) glycerol (RBD-Cv2.2325; RBD-Cv2.1169-CR3022) or 30% (vol/vol) ethylenglycol (RBD-Cv2.6264), followed by flash-freezing in liquid nitrogen. Data collection was carried out at SOLEIL synchrotron. Data were processed, scaled, and reduced with XDS and AIMLESS, and the structures were determined by molecular replacement using Phaser from the suite PHENIX (Liebschner et al., 2019) and search ensembles obtained from the PBDs 6M0J (RBD), 5I1E (Cv2.2325), 5VAG (Cv2.6264), 7K3Q (Cv2.1169), and 6YLA (CR3022). The final models were built by combining real-space model building in Coot (Emsley et al., 2010) with reciprocal space refinement using phenix.refine. The final models were validated with Molprobity (Williams et al., 2018). Epitope and paratope residues, as well as their interactions, were identified by accessing PISA at the European Bioinformatics Institute (http://www.ebi.ac.uk/pdbe/prot_int/pistart.html; Krissinel and Henrick, 2007). Superpositions and figures were rendered using Pymol and UCSF Chimera (Pettersen et al., 2004).

Cryo-EM

The S_6P protein was incubated with the Cv2.1169 IgA Fab at a 1:3.6 (trimer:Fab) ratio and a final trimer concentration of 0.8 µM for 1 h at room temperature. Then 3 µl aliquots of the sample were applied to freshly glow-discharged R 1.2/1.3 Quantifoil grids prior to plunge-freezing using a Vitrobot Mk IV (Thermo Fischer Scientific) at 8°C and 100% humidity (blot 4 s, blot force 0). Data for the complex were acquired on a Titan Krios transmission electron microscope (Thermo Fisher Scientific) operating at 300 kV, using the EPU automated image acquisition software (Thermo Fisher Scientific). Movies were collected on a Gatan K3 direct electron detector operating in counting mode at a nominal magnification of 105,000× (0.85 Å/pixel) using defocus range of –1.0 to –3.0 µm. Movies were collected over a 2-s exposure and a total dose of ∼45 e-/Å^2.

Image processing

All movies were motion-corrected and dose-weighted with MotionCorr2 (Zheng et al., 2017), and the aligned micrographs were used to estimate the defocus values with patchCTF within cryosparc (Punjani et al., 2017). CryoSPARC blob picker was used for automated particle picking, and the resulting particles were used to obtain initial 2D references, which were then used to auto-pick the micrographs. An initial 3D model was obtained in cryosparc and used to perform a 3D classification without imposing any symmetry in Relion (Zivanov et al., 2018). The best class was selected and subjected to 3D, non-uniform refinement in cryosparc (Punjani et al., 2020).

SARS-CoV-2 infection and treatment in K18-hACE2 mice

B6.Cg-Tg(K18-ACE2)2Prlmn/J mice (stock #034860) were imported from The Jackson Laboratory and bred at the Institut Pasteur under strict specific pathogen–free conditions. Infection studies were performed on 6 to 16 wk-old male and female mice, in animal biosafety level 3 (BSL-3) facilities at the Institut Pasteur. All animals were handled in strict accordance with good animal practice. Animal work was approved by the Animal Experimentation Ethics Committee (CETEA 89) of the Institut Pasteur (project dap 200008 and 200023), and authorized by the French legislation (under project 24613) in compliance with the European Communities Council Directives (2010/63/UE, French Law 2013-118, February 6, 2013) and according to the regulations of Pasteur Institute Animal Care Committees before the experiments were initiated. Anesthetized (ketamine/xylazine) mice were inoculated i.n. with 1×10^4 or 1×10^5 PFU of SARS-CoV-2 D614G (20 µl/nostril). 6 or 22 h after inoculation, mice received an i.p. injection of 5, 10, 20, or 40 mg/kg of Cv2.1169 IgG or IgA antibody, and of mGO53 control IgG or IgA antibody. Clinical signs of disease (ruffled fur, hunched posture, reduced mobility, and breathing difficulties) and weight loss were monitored daily for 20 d. Mice were euthanized when they reached pre-defined end-point criteria. Sera were extracted from blood collected by puncture of the retromandibular vein.

SARS-CoV-2 infection and treatment in golden hamsters

Golden Syrian hamsters (*Mesocricetus auratus;* RjHan:AURA) of 5–6 wk of age (average weight 60–80 g) were purchased from Janvier Laboratories and handled under specific pathogen–free conditions. Golden hamsters were housed and manipulated in class III safety cabinets in the Pasteur Institute animal facilities accredited by the French Ministry of Agriculture for performing experiments on live rodents with ad libitum access to water and food. Animal work was approved by the Animal Experimentation Ethics Committee (CETEA 89) of the Institut Pasteur (project dap 200023) and authorized by the French legislation (project #25326) in compliance with the European Communities Council Directives (2010/63/UE, French Law 2013-118, February 6, 2013) and according to the regulations of Pasteur Institute Animal Care Committees before the experiments were initiated. Animal infection was performed as previously described (de Melo et al., 2021). Briefly, anesthetized animals were infected i.n. with 6×10^4 PFU of SARS-CoV-2 (BetaCoV/France/IDF00372/2020; 50 µl/nostril). Mock-infected animals received the physiological solution only. 4 or 24 h after i.n. inoculation, hamsters received an i.p. injection of 10 or 5 mg/kg of Cv2.1169 IgG or IgA antibody, as well as the mGO53 control antibody or PBS. All hamsters were followed-up daily when the body weight and the clinical score were noted. At day 5 after inoculation, animals were euthanized with an excess of anesthetics (ketamine and xylazine) and exsanguination (AVMA Guidelines 2020). Blood samples were collected by cardiac puncture; after coagulation, tubes were centrifuged at 1,500 *g* during 10 min at 4°C, and sera were collected and frozen at −80°C until further analyses. The lungs were weighed and frozen at −80°C until further analyses. Frozen lungs fragments were weighed and homogenized with 1 ml of ice-cold DMEM (Gibco) supplemented with 1% penicillin/streptomycin (15140148; Thermo Fisher Scientific) in Lysing Matrix M 2 ml tubes (MP Biomedicals) using the FastPrep-24 system (MP Biomedicals), and the following scheme: homogenization at 4.0 m/s during 20 s, incubation at 4°C during 2 min, and new homogenization at 4.0 m/s during 20 s. The tubes were centrifuged at 10,000 *g* during 1 min at 4°C. The supernatants were titrated on Vero-E6 cells by classical plaque assays using semisolid overlays (Avicel, RC581-NFDR080I; DuPont) and expressed and PFU/100 mg of tissue (Baer and Kehn-Hall, 2014). Frozen lungs fragments were homogenized with Trizol (Invitrogen) in Lysing Matrix D 2 ml tubes (MP Biomedicals) using the FastPrep-24 system (MP Biomedicals), and the following scheme: homogenization at 6.5 m/s during 60 s, and centrifugation at 12,000 *g* during 2 min at 4°C. The supernatants were collected and the total RNA was then extracted using the Direct-zol RNA MiniPrep Kit (Zymo Research) and quantified using NanoDrop 2000. The presence of genomic SARS-CoV-2 RNA in these samples was evaluated by one-step RT-qPCR in a final volume of 25 µl per reaction in 96-well PCR plates using a thermocycler (7500t Real-time PCR system; Applied Biosystems) as previously described (de Melo et al., 2021). Viral load quantification (expressed as RNA copy number/µg of RNA) was assessed by linear regression using a standard curve of six known quantities of RNA transcripts containing the *RdRp* sequence (ranging from 10^7 to 10^2 copies).

Quantification and statistical analysis

The numbers of V_H, Vκ, and Vλ mutations were compared across groups of antibodies using unpaired Student's *t* test with Welch's correction. Bivariate correlations were assayed using two-tailed Pearson correlation test. Statistical analyses were performed using GraphPad Prism software (v.8.2; GraphPad Prism Inc.). Volcano plot comparing gene features (n = 206 parameters) of tri-S^+ B cells and normal memory B-cells (mB) was also performed using GraphPad Prism software (v.8.4; GraphPad Prism Inc.). The y axis indicates the statistics expressed as $-\log_{10}$ (P values) and the x axis represents the differences between the group means for each parameter. The Barnes-Hut implementation of *t*-distributed stochastic neighbor embedding (t-SNE) was computed using FlowJo software (v.10.3; FlowJo LLC) with 2,000 iterations and a perplexity parameter of 200. Colors represent the density of surface expression markers or cell populations varying from low (blue) to high (red). Circos plot linking antibody sequences with at least 75% identity within

their CDR_H3 was performed using online software at http://mkweb.bcgsc.ca/circos. The phylogenetic tree was built using CLC Main Workbench (Qiagen) on aligned V_H sequences using the neighbor-joining method with a bootstrap analysis on 100 replicates. Mouse survival was compared across groups using a Kaplan–Meier analysis and Log-rank Mantel-Cox test (GraphPad Prism, v8.2; GraphPad Prism Inc.). Groups of golden Syrian hamsters were compared across analyses using two-tailed Mann–Whitney test (GraphPad Prism, v.8.2; GraphPad Prism Inc.). PCA was performed using the prcomp() function in R Studio Server (v1.4.1103). PCA plots of individuals [fviz_pca_ind()], variables [fviz_pca_var()], and biplots [fviz_pca_biplot()] were generated using the factoextra package (v1.0.7, https://CRAN.R-project.org/package=factoextra). Spearman rank correlations were used to establish multiparameter associations. All correlograms and scatterplots were created using the corrplot and plot R functions, respectively. Correlation plots were generated using GraphPad Prism (v6.4; GraphPad Prism Inc.).

Online supplemental material

Fig. S1 shows the SARS-CoV-2 reactivity of sera, purified polyclonal, and mAbs from COVID-19 convalescents. Fig. S2 presents the humoral immune features of COVID-19 convalescents and SARS-CoV-2 S–specific memory B cells. Fig. S3 presents the binding characteristics of potent anti-RBD antibody neutralizers. Fig. S4 shows the cross-neutralizing activity of potent SARS-CoV-2 neutralizers. Fig. S5 presents the Cv2.1169 antibody treatment in SARS-CoV-2–infected mice and hamsters. Table S1 provides details on the immunoglobulin gene repertoire, reactivity and antiviral functions of human SARS-CoV-2 spike memory B-cell antibodies cloned from Wuhan SARS-CoV-2 convalescents. Table S2 provides the affinity and neutralization activity values for Cv2.1169 and Cv2.3194 antibodies. Table S3 presents the data collection and refinement statistics of the RBD–Fab crystallized complexes. Table S4 provides the buried surface area at the RBD–antibody interface. Table S5 presents the polar contacts at the RBD–Fab interface for the different crystallized complexes. Data S1 shows the cryo-EM data collection and processing of the Cv2.1169-SARS-CoV-2 S_6P complex.

Data availability

Atomic coordinates for the RBD-Cv2.1169, -Cv2.3235, and -Cv2.6264 complexes were deposited in the Protein Data Bank (PDB) with the numbers 7QEZ, 7QF0, and 7QF1 respectively. The cryo-EM density map for the SARS-CoV-2 S_6P-Cv2.1169 complex was deposited in the Electron Microscopy Data Bank with the accession number EMD-14853.

Acknowledgments

We are grateful to all convalescent donors who consented to be part of this study, as well as all investigators, clinicians, medical staff members, and participants involved in the study. We thank the members of the Crystallography core facility (Institut Pasteur) for carrying out robot-driven crystallization screenings and of the beamlines Proxima 1 and Proxima 2 at the French national synchrotron facility (SOLEIL, St Aubin, France). We also thank the NanoImaging core facility (Institut Pasteur) for support with sample preparation and image acquisition. We thank the members of the direction des applications de la recherche et des relations industrielles (DARRI, Institut Pasteur) involved in the project, particularly Hélène Chommy from the patent office. We thank the members of the SpikImm team for their support and helpful discussions.

The NanoImaging Core was created with the help of a grant from the French Government's Investissements d'Avenir program (EQUIPEX CACSICE, ANR-11-EQPX-0008). The French COVID Cohort, sponsored by the Institut national de la santé et de la recherche médicale (INSERM), is funded through the REACTing (REsearch & ACtion emergING infectious diseases) consortium, the Ministry of Health and Social Affairs, the Ministry of Higher Education and Research dedicated COVID-19 fund and Programme hospitalier de recherche clinique no. 20-0424. Funding sources are not involved in the study design, data acquisition, data analysis, data interpretation or manuscript writing. This work was supported by grants from the Agence Nationale de la Recherche REACTing Covid19 (#20RR028-00), the European Commission Horizon 2020 program (RECoVER project, #101003589), the Institut Pasteur Task Force COVID-19 (2019-NCOV THERAMAB project), the Fondation de France (#00106077), and partly by a SpikImm-Institut Pasteur R&D program. H. Mouquet also received core funding from the Institut Pasteur and INSERM. M. Backovic (2020-TooLab project) received support from the "URGENCE COVID-19" fundraising campaign (Institut Pasteur). I. Fernández was a recipient of an Agence Nationale de Recherches sur le Sida et les Hépatites Virales post-doctoral fellowship.

Author contributions: H. Mouquet conceived and supervised the study. J.D. de Melo, F. Agou, H. Bourhy, E. Simon-Lorière, X. Montagutelli, F.A. Rey, O. Schwartz, and H. Mouquet supervised the experiments. C. Planchais, I. Fernández, T. Bruel, G.D. de Melo, M. Prot, M. Beretta, J. Dufloo, L.M. Molinos-Albert, J. Chiaravalli, E. Giraud, B. Vesin, L. Conquet, L. Grzelak, D. Planas, I. Staropoli, F. Guivel-Benhassine, and H. Mouquet designed, performed, and analyzed the experiments. M. Backovic and P. Guardado-Calvo collected and/or processed x-ray crystallography and cryo-EM data. T. Hieu performed bioinformatic analyses. French COVID and CORSER Cohort Study Groups, M. Cervantes-Gonzalez, and M-N. Ungeheuer organized the collect of human samples. M. Boullé, P. Charneau, and S. van der Werf contributed with key reagents/assays and expertise. C. Planchais and H. Mouquet wrote the manuscript with contributions from all the authors.

Disclosures: C. Planchais reported a patent to PCT/EP2022/058777 licensed (SpikImm). I. Fernández reported a patent to PCT/EP2022/058777 licensed (SpikImm). T. Bruel reported a patent to PCT/EP2022/058777 licensed (SpikImm). G.D. de Melo reported a patent to PCT/EP2022/058777 licensed (SpikImm). P. Charneau reported personal fees from TheraVectys outside the submitted work; in addition, P. Charneau had a patent for seroneutralization pending. S. van der Werf reported a patent for the use of proteins and peptides coded by the genome of a novel strain of SARS-associated coronavirus issued and a patent for

SARS-associated coronavirus diagnostics issued. H. Bourhy reported a patent to PCT/EP2022/058777 licensed (SpikImm) and a patent to PCT/IB2021/000314 issued. X. Montagutelli reported a patent to PCT/EP2022/058777 licensed (SpikImm). F.A. Rey reported a patent to PCT/EP2022/058777 licensed (SpikImm). O. Schwartz reported a patent to PCT/EP2022/058777 licensed (SpikImm). H. Mouquet reported grants from SpikImm and personal fees from SpikImm during the conduct of the study; in addition, H. Mouquet had a patent to PCT/EP2022/058777 licensed (SpikImm). No other disclosures were reported.

Submitted: 12 April 2022
Revised: 19 May 2022
Accepted: 20 May 2022

References

Andreano, E., E. Nicastri, I. Paciello, P. Pileri, N. Manganaro, G. Piccini, A. Manenti, E. Pantano, A. Kabanova, M. Troisi, et al. 2021. Extremely potent human monoclonal antibodies from COVID-19 convalescent patients. *Cell*. 184:1821–1835.e16. https://doi.org/10.1016/j.cell.2021.02.035

Anna, F., S. Goyard, A.I. Lalanne, F. Nevo, M. Gransagne, P. Souque, D. Louis, V. Gillon, I. Turbiez, F.C. Bidard, et al. 2021. High seroprevalence but short-lived immune response to SARS-CoV-2 infection in Paris. *Eur. J. Immunol.* 51:180–190. https://doi.org/10.1002/eji.202049058

Baer, A., and K. Kehn-Hall. 2014. Viral concentration determination through plaque assays: Using traditional and novel overlay systems. *J. Vis. Exp.* e52065. https://doi.org/10.3791/52065

Barnes, C.O., A.P. West, K.E. Huey-Tubman, M.A.G. Hoffmann, N.G. Sharaf, P.R. Hoffman, N. Koranda, H.B. Gristick, C. Gaebler, F. Muecksch, et al. 2020a. Structures of human antibodies bound to SARS-CoV-2 spike reveal common epitopes and Recurrent features of antibodies. *Cell*. 182:828–842.e16. https://doi.org/10.1016/j.cell.2020.06.025

Barnes, C.O., C.A. Jette, M.E. Abernathy, K.M.A. Dam, S.R. Esswein, H.B. Gristick, A.G. Malyutin, N.G. Sharaf, K.E. Huey-Tubman, Y.E. Lee, et al. 2020b. SARS-CoV-2 neutralizing antibody structures inform therapeutic strategies. *Nature*. 588:682–687. https://doi.org/10.1038/s41586-020-2852-1

Betton, M., M. Livrozet, D. Planas, A. Fayol, B. Monel, B. Védie, T. Bruel, E. Tartour, N. Robillard, J.-C. Manuguerra, et al. 2021. Sera neutralizing activities against severe acute respiratory syndrome coronavirus 2 and multiple variants 6 Months after hospitalization for Coronavirus disease 2019. *Clin. Infect. Dis.* 73:e1337–e1344. https://doi.org/10.1093/cid/ciab308

Brouwer, P.J.M., T.G. Caniels, K. van der Straten, J.L. Snitselaar, Y. Aldon, S. Bangaru, J.L. Torres, N.M.A. Okba, M. Claireaux, G. Kerster, et al. 2020. Potent neutralizing antibodies from COVID-19 patients define multiple targets of vulnerability. *Science*. 369:643–650. https://doi.org/10.1126/science.abc5902

Bruel, T., J. Hadjadj, P. Maes, D. Planas, A. Seve, I. Staropoli, F. Guivel-Benhassine, F. Porrot, W.-H. Bolland, Y. Nguyen, et al. 2022. Serum neutralization of SARS-CoV-2 Omicron sublineages BA.1 and BA.2 in patients receiving monoclonal antibodies. *Nat Med*. https://doi.org/10.1038/s41591-022-01792-5

Buchrieser, J., J. Dufloo, M. Hubert, B. Monel, D. Planas, M.M. Rajah, C. Planchais, F. Porrot, F. Guivel-Benhassine, S. Van der Werf, et al. 2020. Syncytia formation by SARS-CoV-2-infected cells. *EMBO J.* 39:e106267. https://doi.org/10.15252/embj.2020106267

Cameroni, E., J.E. Bowen, L.E. Rosen, C. Saliba, S.K. Zepeda, K. Culap, D. Pinto, L.A. VanBlargan, A. De Marco, J. di Iulio, et al. 2022. Broadly neutralizing antibodies overcome SARS-CoV-2 Omicron antigenic shift. *Nature*. 602:664–670. https://doi.org/10.1038/s41586-021-04386-2

Cao, Y., B. Su, X. Guo, W. Sun, Y. Deng, L. Bao, Q. Zhu, X. Zhang, Y. Zheng, C. Geng, et al. 2020. Potent neutralizing antibodies against SARS-CoV-2 identified by high-throughput single-cell sequencing of convalescent patients' B cells. *Cell*. 182:73–84.e16. https://doi.org/10.1016/j.cell.2020.05.025

Cao, Y., J. Wang, F. Jian, T. Xiao, W. Song, A. Yisimayi, W. Huang, Q. Li, P. Wang, R. An, et al. 2022a. Omicron escapes the majority of existing SARS-CoV-2 neutralizing antibodies. *Nature*. 602:657–663. https://doi.org/10.1038/s41586-021-04385-3

Cao, Y., A. Yisimayi, F. Jian, W. Song, T. Xiao, L. Wang, S. Du, J. Wang, Q. Li, X. Chen, et al. 2022b. BA.2.12.1, BA.4 and BA.5 escape antibodies elicited by Omicron BA.1 infection. *Res. Sq.* https://doi.org/10.21203/rs.3.rs-1611421/v1 (Preprint posted May 2, 2022)

Chen, E.C., P. Gilchuk, S.J. Zost, N. Suryadevara, E.S. Winkler, C.R. Cabel, E. Binshtein, R.E. Chen, R.E. Sutton, J. Rodriguez, et al. 2021. Convergent antibody responses to the SARS-CoV-2 spike protein in convalescent and vaccinated individuals. *Cell Rep.* 36:109604. https://doi.org/10.1016/j.celrep.2021.109604

Chertow, D., S. Stein, S. Ramelli, A. Grazioli, C. Winkler, J. Dickey, A. Platt, S. Pittaluga, D. Herr, and M. Mccurdy. 2021. SARS-CoV-2 Infection and Persistence throughout the Human Body and Brain National Institutes of Health. *Res. Square*. https://doi.org/10.21203/rs.3.rs-1139035/v1

Chi, X., R. Yan, J. Zhang, G. Zhang, Y. Zhang, M. Hao, Z. Zhang, P. Fan, Y. Dong, Y. Yang, et al. 2020. A neutralizing human antibody binds to the N-terminal domain of the Spike protein of SARS-CoV-2. *Science*. 369:650–655. https://doi.org/10.1126/science.abc6952

Corti, D., L.A. Purcell, G. Snell, and D. Veesler. 2021. Tackling COVID-19 with neutralizing monoclonal antibodies. *Cell*. 184:4593–4595. https://doi.org/10.1016/j.cell.2021.07.027

de Melo, G.D., F. Lazarini, F. Larrous, L. Feige, E. Kornobis, S. Levallois, A. Marchio, L. Kergoat, D. Hardy, T. Cokelaer, et al. 2021. Attenuation of clinical and immunological outcomes during SARS-CoV-2 infection by ivermectin. *EMBO Mol. Med.* 13:e14122. https://doi.org/10.15252/emmm.202114122

Dejnirattisai, W., D. Zhou, P. Supasa, C. Liu, A.J. Mentzer, H.M. Ginn, Y. Zhao, H.M.E. Duyvesteyn, A. Tuekprakhon, R. Nutalai, et al. 2021a. Antibody evasion by the P.1 strain of SARS-CoV-2. *Cell*. 184:2939–2954.e9. https://doi.org/10.1016/j.cell.2021.03.055

Dejnirattisai, W., D. Zhou, H.M. Ginn, H.M.E. Duyvesteyn, P. Supasa, J.B. Case, Y. Zhao, T.S. Walter, A.J. Mentzer, C. Liu, et al. 2021b. The antigenic anatomy of SARS-CoV-2 receptor binding domain. *Cell*. 184:2183–2200.e22. https://doi.org/10.1016/j.cell.2021.02.032

Dong, J., S.J. Zost, A.J. Greaney, T.N. Starr, A.S. Dingens, E.C. Chen, R.E. Chen, J.B. Case, R.E. Sutton, P. Gilchuk, et al. 2021. Genetic and structural basis for SARS-CoV-2 variant neutralization by a two-antibody cocktail. *Nat. Microbiol.* 6:1233–1244. https://doi.org/10.1038/s41564-021-00972-2

Dufloo, J., L. Grzelak, I. Staropoli, Y. Madec, L. Tondeur, F. Anna, S. Pelleau, A. Wiedemann, C. Planchais, J. Buchrieser, et al. 2021. Asymptomatic and symptomatic SARS-CoV-2 infections elicit polyfunctional antibodies. *Cell Rep. Med.* 2:100275. https://doi.org/10.1016/j.xcrm.2021.100275

Emsley, P., B. Lohkamp, W.G. Scott, and K. Cowtan. 2010. Features and development of Coot. *Acta Crystallogr. Sect. D Biol. Crystallogr.* 66:486–501. https://doi.org/10.1107/S0907444910007493

Gaebler, C., Z. Wang, J.C.C. Lorenzi, F. Muecksch, S. Finkin, M. Tokuyama, A. Cho, M. Jankovic, D. Schaefer-Babajew, T.Y. Oliveira, et al. 2021. Evolution of antibody immunity to SARS-CoV-2. *Nature*. 591:639–644. https://doi.org/10.1038/s41586-021-03207-w

Galson, J.D., S. Schaetzle, R.J.M. Bashford-Rogers, M.I.J. Raybould, A. Kovaltsuk, G.J. Kilpatrick, R. Minter, D.K. Finch, J. Dias, L.K. James, et al. 2020. Deep sequencing of B cell receptor repertoires from COVID-19 patients reveals strong convergent immune signatures. *Front. Immunol.* 11:605170. https://doi.org/10.3389/fimmu.2020.605170

Rappazzo, C.G., L.V. Tse, C.I. Kaku, D. Wrapp, M. Sakharkar, D. Huang, L.M. Deveau, T.J. Yockachonis, A.S. Herbert, M.B. Battles, et al. 2021. Broad and potent activity against SARS-like viruses by an engineered human monoclonal antibody. *Science*. 371:823–829. https://doi.org/10.1126/science.abf4830

Gentile, I., and N. Schiano Moriello. 2022. COVID-19 prophylaxis in immunosuppressed patients: Beyond vaccination. *PLoS Med.* 19:e1003917. https://doi.org/10.1371/journal.pmed.1003917

Gilbert, P.B., D.C. Montefiori, A.B. McDermott, Y. Fong, D. Benkeser, W. Deng, H. Zhou, C.R. Houchens, K. Martins, L. Jayashankar, et al. 2022. Immune correlates analysis of the mRNA-1273 COVID-19 vaccine efficacy clinical trial. *Science*. 375:43–50. https://doi.org/10.1126/science.abm3425

Greaney, A.J., T.N. Starr, P. Gilchuk, S.J. Zost, E. Binshtein, A.N. Loes, S.K. Hilton, J. Huddleston, R. Eguia, K.H.D. Crawford, et al. 2021. Complete mapping of mutations to the SARS-CoV-2 spike receptor-binding domain that escape antibody recognition. *Cell Host Microbe*. 29:44–57.e9. https://doi.org/10.1016/j.chom.2020.11.007

Gruell, H., K. Vanshylla, P. Tober-Lau, D. Hillus, P. Schommers, C. Lehmann, F. Kurth, L.E. Sander, and F. Klein. 2022. mRNA booster immunization

elicits potent neutralizing serum activity against the SARS-CoV-2 Omicron variant. *Nat. Med.* 28:477–480. https://doi.org/10.1038/s41591-021-01676-0

Grzelak, L., S. Temmam, C. Planchais, C. Demeret, L. Tondeur, C. Huon, F. Guivel-Benhassine, I. Staropoli, M. Chazal, J. Dufloo, et al. 2020. A comparison of four serological assays for detecting anti-SARS-CoV-2 antibodies in human serum samples from different populations. *Sci. Transl. Med.* 12:eabc3103. https://doi.org/10.1126/scitranslmed.abc3103

Han, P., C. Su, Y. Zhang, C. Bai, A. Zheng, C. Qiao, Q. Wang, S. Niu, Q. Chen, Y. Zhang, et al. 2021. Molecular insights into receptor binding of recent emerging SARS-CoV-2 variants. *Nat. Commun.* 12:6103. https://doi.org/10.1038/s41467-021-26401-w

Hansen, J., A. Baum, K.E. Pascal, V. Russo, S. Giordano, E. Wloga, B.O. Fulton, Y. Yan, K. Koon, K. Patel, et al. 2020. Studies in humanized mice and convalescent humans yield a SARS-CoV-2 antibody cocktail. *Science.* 369:1010–1014. https://doi.org/10.1126/science.abd0827

Hoffmann, M., H. Kleine-Weber, S. Schroeder, N. Krüger, T. Herrler, S. Erichsen, T.S. Schiergens, G. Herrler, N.H. Wu, A. Nitsche, et al. 2020. SARS-CoV-2 cell entry depends on ACE2 and TMPRSS2 and is blocked by a clinically proven protease inhibitor. *Cell.* 181:271–280.e8. https://doi.org/10.1016/j.cell.2020.02.052

Hsieh C.L., Goldsmith, J.A., Schaub, J.M., Divenere, A.M., Kuo H.C., Javanmardi, K., Le, K.C., Wrapp, D., Lee, A.G., Liu, Y., et al. 2020. Structure-based design of prefusion-stabilized SARS-CoV-2 spikes. *Science.* 369:1501–1505. https://doi.org/10.1126/science.abd0826

Imai, M., K. Iwatsuki-Horimoto, M. Hatta, S. Loeber, P.J. Halfmann, N. Nakajima, T. Watanabe, M. Ujie, K. Takahashi, M. Ito, et al. 2020. Syrian hamsters as a small animal model for SARS-CoV-2 infection and countermeasure development. *Proc. Natl. Acad. Sci. USA.* 117:16587–16595. https://doi.org/10.1073/pnas.2009799117

Isho, B., K.T. Abe, M. Zuo, A.J. Jamal, B. Rathod, J.H. Wang, Z. Li, G. Chao, O.L. Rojas, Y.M. Bang, et al. 2020. Persistence of serum and saliva antibody responses to SARS-CoV-2 spike antigens in COVID-19 patients. *Sci. Immunol.* 5:eabe5511. https://doi.org/10.1126/sciimmunol.abe5511

Jones, B.E., P.L. Brown-Augsburger, K.S. Corbett, K. Westendorf, J. Davies, T.P. Cujec, C.M. Wiethoff, J.L. Blackbourne, B.A. Heinz, D. Foster, et al. 2021. The neutralizing antibody, LY-CoV555, protects against SARS-CoV-2 infection in nonhuman primates. *Sci. Transl. Med.* 13:eabf1906. https://doi.org/10.1126/scitranslmed.abf1906

Ju, B., Q. Zhang, J. Ge, R. Wang, J. Sun, X. Ge, J. Yu, S. Shan, B. Zhou, S. Song, et al. 2020. Human neutralizing antibodies elicited by SARS-CoV-2 infection. *Nature.* 584:115–119. https://doi.org/10.1038/s41586-020-2380-z

Juno, J.A., H.X. Tan, W.S. Lee, A. Reynaldi, H.G. Kelly, K. Wragg, R. Esterbauer, H.E. Kent, C.J. Batten, F.L. Mordant, et al. 2020. Humoral and circulating follicular helper T cell responses in recovered patients with COVID-19. *Nat. Med.* 26:1428–1434. https://doi.org/10.1038/s41591-020-0995-0

Ke, Z., J. Oton, K. Qu, M. Cortese, V. Zila, L. McKeane, T. Nakane, J. Zivanov, C.J. Neufeldt, B. Cerikan, et al. 2020. Structures and distributions of SARS-CoV-2 spike proteins on intact virions. *Nature.* 588:498–502. https://doi.org/10.1038/s41586-020-2665-2

Kelley, B. 2020. Developing therapeutic monoclonal antibodies at pandemic pace. *Nat. Biotechnol.* 38:540–545. https://doi.org/10.1038/s41587-020-0512-5

Khoury, D.S., D. Cromer, A. Reynaldi, T.E. Schlub, A.K. Wheatley, J.A. Juno, K. Subbarao, S.J. Kent, J.A. Triccas, and M.P. Davenport. 2021. Neutralizing antibody levels are highly predictive of immune protection from symptomatic SARS-CoV-2 infection. *Nat. Med.* 27:1205–1211. https://doi.org/10.1038/s41591-021-01377-8

Kim, C., D.K. Ryu, J. Lee, Y. I Kim, J.M. Seo, Y.G. Kim, J.H. Jeong, M. Kim, J.I. Kim, P. Kim, et al. 2021. A therapeutic neutralizing antibody targeting receptor binding domain of SARS-CoV-2 spike protein. *Nat. Commun.* 12:288. https://doi.org/10.1038/s41467-020-20602-5

Koide, S. 2009. Engineering of recombinant crystallization chaperones. *Curr. Opin. Struct. Biol.* 19:449–457. https://doi.org/10.1016/j.sbi.2009.04.008

Krammer, F. 2021. A correlate of protection for SARS-CoV-2 vaccines is urgently needed. *Nat. Med.* 27:1147–1148. https://doi.org/10.1038/s41591-021-01432-4

Kreer, C., M. Zehner, T. Weber, M.S. Ercanoglu, L. Gieselmann, C. Rohde, S. Halwe, M. Korenkov, P. Schommers, K. Vanshylla, et al. 2020. Longitudinal isolation of potent near-germline SARS-CoV-2-neutralizing antibodies from COVID-19 patients. *Cell.* 182:1663–1673. https://doi.org/10.1016/j.cell.2020.08.046

Kreye, J., S.M. Reincke, H.-C. Kornau, E. Sánchez-Sendin, V.M. Corman, H. Liu, M. Yuan, N.C. Wu, X. Zhu, C.-C.D. Lee, et al. 2020. A therapeutic non-self-reactive SARS-CoV-2 antibody protects from Lung pathology in a COVID-19 hamster model. *Cell.* 183:1058–1069.e19. https://doi.org/10.1016/j.cell.2020.09.049

Krissinel, E., and K. Henrick. 2007. Inference of macromolecular assemblies from crystalline state. *J. Mol. Biol.* 372:774–797. https://doi.org/10.1016/j.jmb.2007.05.022

Kumar, S., A. Chandele, and A. Sharma. 2021. Current status of therapeutic monoclonal antibodies against SARS-CoV-2. *PLoS Pathog.* 17:e1009885. https://doi.org/10.1371/journal.ppat.1009885

Lan, J., J. Ge, J. Yu, S. Shan, H. Zhou, S. Fan, Q. Zhang, X. Shi, Q. Wang, L. Zhang, et al. 2020. Structure of the SARS-CoV-2 spike receptor-binding domain bound to the ACE2 receptor. *Nature.* 581:215–220. https://doi.org/10.1038/s41586-020-2180-5

Liebschner, D., P.V. Afonine, M.L. Baker, G. Bunkoczi, V.B. Chen, T.I. Croll, B. Hintze, L.W. Hung, S. Jain, A.J. McCoy, et al. 2019. Macromolecular structure determination using X-rays, neutrons and electrons: Recent developments in Phenix. *Acta Crystallogr. D. Struct. Biol.* 75:861–877. https://doi.org/10.1107/S2059798319011471

Liu, L., P. Wang, M.S. Nair, J. Yu, M. Rapp, Q. Wang, Y. Luo, J.F.-W. Chan, V. Sahi, A. Figueroa, et al. 2020. Potent neutralizing antibodies against multiple epitopes on SARS-CoV-2 spike. *Nature.* 584:450–456. https://doi.org/10.1038/s41586-020-2571-7

Locci, M., C. Havenar-Daughton, E. Landais, J. Wu, M.A. Kroenke, C.L. Arlehamn, L.F. Su, R. Cubas, M.M. Davis, A. Sette, et al. 2013. Human circulating PD-1+CXCR3−CXCR5+ memory Tfh cells are highly functional and correlate with broadly neutralizing HIV antibody responses. *Immunity.* 39:758–769. https://doi.org/10.1016/j.immuni.2013.08.031

Long, Q.X., B.Z. Liu, H.J. Deng, G.C. Wu, K. Deng, Y.K. Chen, P. Liao, J.F. Qiu, Y. Lin, X.F. Cai, et al. 2020. Antibody responses to SARS-CoV-2 in patients with COVID-19. *Nat. Med.* 26:845–848. https://doi.org/10.1038/s41591-020-0897-1

Lorin, V., and H. Mouquet. 2015. Efficient generation of human IgA monoclonal antibodies. *J. Immunol. Methods.* 422:102–110. https://doi.org/10.1016/j.jim.2015.04.010

Lorin, V., I. Fernández, G. Masse-Ranson, M. Bouvin-Pley, L.M. Molinos-Albert, C. Planchais, T. Hieu, G. Péhau-Arnaudet, D. Hrebík, G. Girelli-Zubani, et al. 2022. Epitope convergence of broadly HIV-1 neutralizing IgA and IgG antibody lineages in a viremic controller. *J. Exp. Med.* 219:e20212045. https://doi.org/10.1084/jem.20212045

Meffre, E., A. Schaefer, H. Wardemann, P. Wilson, E. Davis, and M.C. Nussenzweig. 2004. Surrogate light chain expressing human peripheral B cells produce self-reactive antibodies. *J. Exp. Med.* 199:145–150. https://doi.org/10.1084/jem.20031550

Morita, R., N. Schmitt, S.E. Bentebibel, R. Ranganathan, L. Bourdery, G. Zurawski, E. Foucat, M. Dullaers, S. Oh, N. Sabzghabaei, et al. 2011. Human blood CXCR5+CD4+ T cells are counterparts of T follicular cells and contain specific subsets that differentially support antibody secretion. *Immunity.* 34:108–121. https://doi.org/10.1016/j.immuni.2010.12.012

Mouquet, H., F. Klein, J.F. Scheid, M. Warncke, J. Pietzsch, T.Y.K. Oliveira, K. Velinzon, M.S. Seaman, and M.C. Nussenzweig. 2011. Memory B cell antibodies to HIV-1 gp140 cloned from individuals infected with clade A and B viruses. *PLoS One.* 6:e24078. https://doi.org/10.1371/journal.pone.0024078

Mouquet, H., L. Scharf, Z. Euler, Y. Liu, C. Eden, J.F. Scheid, A. Halper-Stromberg, P.N.P. Gnanapragasam, D.I.R. Spencer, M.S. Seaman, et al. 2012. Complex-type N-glycan recognition by potent broadly neutralizing HIV antibodies. *Proc. Natl. Acad. Sci. USA.* 109:E3268–E3277. https://doi.org/10.1073/pnas.1217207109

Nielsen, S.C.A., F. Yang, K.J.L. Jackson, R.A. Hoh, K. Röltgen, G.H. Jean, B.A. Stevens, J.-Y. Lee, A. Rustagi, A.J. Rogers, et al. 2020. Human B cell clonal expansion and convergent antibody responses to SARS-CoV-2. *Cell Host Microbe.* 28:516–525.e5. https://doi.org/10.1016/j.chom.2020.09.002

Noy-Porat, T., A. Mechaly, Y. Levy, E. Makdasi, R. Alcalay, D. Gur, M. Aftalion, R. Falach, S. Leviatan Ben-Arye, S. Lazar, et al. 2021. Therapeutic antibodies, targeting the SARS-CoV-2 spike N-terminal domain, protect lethally infected K18-hACE2 mice. *iScience.* 24:102479. https://doi.org/10.1016/j.isci.2021.102479

Pettersen, E.F., T.D. Goddard, C.C. Huang, G.S. Couch, D.M. Greenblatt, E.C. Meng, and T.E. Ferrin. 2004. UCSF Chimera; A visualization system for exploratory research and analysis. *J. Comput. Chem.* 25:1605–1612. https://doi.org/10.1002/jcc.20084

Pinto, D., Y.J. Park, M. Beltramello, A.C. Walls, M.A. Tortorici, S. Bianchi, S. Jaconi, K. Culap, F. Zatta, A. De Marco, et al. 2020. Cross-neutralization

of SARS-CoV-2 by a human monoclonal SARS-CoV antibody. *Nature*. 583:290–295. https://doi.org/10.1038/s41586-020-2349-y

Pinto, D., M.M. Sauer, N. Czudnochowski, J.S. Low, M.A. Tortorici, M.P. Housley, J. Noack, A.C. Walls, J.E. Bowen, B. Guarino, et al. 2021. Broad betacoronavirus neutralization by a stem helix–specific human antibody. *Science*. 373:1109–1116. https://doi.org/10.1126/science.abj3321

Planas, D., T. Bruel, L. Grzelak, F. Guivel-Benhassine, I. Staropoli, F. Porrot, C. Planchais, J. Buchrieser, M.M. Rajah, E. Bishop, et al. 2021a. Sensitivity of infectious SARS-CoV-2 B.1.1.7 and B.1.351 variants to neutralizing antibodies. *Nat. Med.* 27:917–924. https://doi.org/10.1038/s41591-021-01318-5

Planas, D., D. Veyer, A. Baidaliuk, I. Staropoli, F. Guivel-Benhassine, M.M. Rajah, C. Planchais, F. Porrot, N. Robillard, J. Puech, et al. 2021b. Reduced sensitivity of SARS-CoV-2 variant Delta to antibody neutralization. *Nature*. 596:276–280. https://doi.org/10.1038/s41586-021-03777-9

Planas, D., N. Saunders, P. Maes, F. Guivel-Benhassine, C. Planchais, J. Buchrieser, W.-H. Bolland, F. Porrot, I. Staropoli, F. Lemoine, et al. 2022. Considerable escape of SARS-CoV-2 Omicron to antibody neutralization. *Nature*. 602:671–675. https://doi.org/10.1038/s41586-021-04389-z

Planchais, C., A. Kök, A. Kanyavuz, V. Lorin, T. Bruel, F. Guivel-Benhassine, T. Rollenske, J. Prigent, T. Hieu, T. Prazuck, et al. 2019. HIV-1 envelope recognition by polyreactive and cross-reactive intestinal B cells. *Cell Rep.* 27:572–585.e7. https://doi.org/10.1016/j.celrep.2019.03.032

Prigent, J., V. Lorin, A. Kök, T. Hieu, S. Bourgeau, and H. Mouquet. 2016. Scarcity of autoreactive human blood IgA + memory B cells. *Eur. J. Immunol.* 46:2340–2351. https://doi.org/10.1002/eji.201646446

Punjani, A., J.L. Rubinstein, D.J. Fleet, and M.A. Brubaker. 2017. cryoSPARC: Algorithms for rapid unsupervised cryo-EM structure determination. *Nat. Methods*. 14:290–296. https://doi.org/10.1038/nmeth.4169

Punjani, A., H. Zhang, and D.J. Fleet. 2020. Non-uniform refinement: Adaptive regularization improves single-particle cryo-EM reconstruction. *Nat. Methods*. 17:1214–1221. https://doi.org/10.1038/s41592-020-00990-8

Radvak, P., H.-J. Kwon, M. Kosikova, U. Ortega-Rodriguez, R. Xiang, J.-N. Phue, R.-F. Shen, J. Rozzelle, N. Kapoor, T. Rabara, et al. 2021. SARS-CoV-2 B.1.1.7 (alpha) and B.1.351 (beta) variants induce pathogenic patterns in K18-hACE2 transgenic mice distinct from early strains. *Nat. Commun.* 12:6559. https://doi.org/10.1038/s41467-021-26803-w

Robbiani, D.F., C. Gaebler, F. Muecksch, J.C.C. Lorenzi, Z. Wang, A. Cho, M. Agudelo, C.O. Barnes, A. Gazumyan, S. Finkin, et al. 2020. Convergent antibody responses to SARS-CoV-2 in convalescent individuals. *Nature*. 584:437–442. https://doi.org/10.1038/s41586-020-2456-9

Rogers, T.F., F. Zhao, D. Huang, N. Beutler, A. Burns, W.-T. He, O. Limbo, C. Smith, G. Song, J. Woehl, et al. 2020. Isolation of potent SARS-CoV-2 neutralizing antibodies and protection from disease in a small animal model. *Science*. 369:956–963. https://doi.org/10.1126/science.abc7520

Rosenfeld, R., T. Noy-Porat, A. Mechaly, E. Makdasi, Y. Levy, R. Alcalay, R. Falach, M. Aftalion, E. Epstein, D. Gur, et al. 2021. Post-exposure protection of SARS-CoV-2 lethal infected K18-hACE2 transgenic mice by neutralizing human monoclonal antibody. *Nat. Commun.* 12:944. https://doi.org/10.1038/s41467-021-21239-8

Rujas, E., I. Kucharska, Y.Z. Tan, S. Benlekbir, H. Cui, T. Zhao, G.A. Wasney, P. Budylowski, F. Guvenc, J.C. Newton, et al. 2021. Multivalency transforms SARS-CoV-2 antibodies into ultrapotent neutralizers. *Nat. Commun.* 12:3661. https://doi.org/10.1038/s41467-021-23825-2

Schäfer, A., F. Muecksch, J.C.C. Lorenzi, S.R. Leist, M. Cipolla, S. Bournazos, F. Schmidt, R.M. Maison, A. Gazumyan, D.R. Martinez, et al. 2021. Antibody potency, effector function, and combinations in protection and therapy for SARS-CoV-2 infection in vivo. *J. Exp. Med.* 218:e20201993. https://doi.org/10.1084/jem.20201993

Schmidt, F., Y. Weisblum, M. Rutkowska, D. Poston, J. DaSilva, F. Zhang, E. Bednarski, A. Cho, D.J. Schaefer-Babajew, C. Gaebler, et al. 2021. High genetic barrier to SARS-CoV-2 polyclonal neutralizing antibody escape. *Nature*. 600:512–516. https://doi.org/10.1038/s41586-021-04005-0

Sette, A., and S. Crotty. 2021. Adaptive immunity to SARS-CoV-2 and COVID-19. *Cell*. 184:861–880. https://doi.org/10.1016/j.cell.2021.01.007

Shi, R., C. Shan, X. Duan, Z. Chen, P. Liu, J. Song, T. Song, X. Bi, C. Han, L. Wu, et al. 2020. A human neutralizing antibody targets the receptor-binding site of SARS-CoV-2. *Nature*. 584:120–124. https://doi.org/10.1038/s41586-020-2381-y

Sia, S.F., L.M. Yan, A.W.H. Chin, K. Fung, K.T. Choy, A.Y.L. Wong, P. Kaewpreedee, R.A.P.M. Perera, L.L.M. Poon, J.M. Nicholls, et al. 2020. Pathogenesis and transmission of SARS-CoV-2 in golden hamsters. *Nature*. 583:834–838. https://doi.org/10.1038/s41586-020-2342-5

Singh, D.D., A. Sharma, H.-J. Lee, and D.K. Yadav. 2022. SARS-CoV-2: Recent variants and clinical efficacy of antibody-based therapy. *Front. Cell. Infect. Microbiol.* 12:839170. https://doi.org/10.3389/fcimb.2022.839170

Smith, N., P. Goncalves, B. Charbit, L. Grzelak, M. Beretta, C. Planchais, T. Bruel, V. Rouilly, V. Bondet, J. Hadjadj, et al. 2021. Distinct systemic and mucosal immune responses during acute SARS-CoV-2 infection. *Nat. Immunol.* 22:1428–1439. https://doi.org/10.1038/s41590-021-01028-7

Sokal, A., P. Chappert, G. Barba-Spaeth, A. Roeser, S. Fourati, I. Azzaoui, A. Vandenberghe, I. Fernandez, A. Meola, M. Bouvier-Alias, et al. 2021. Maturation and persistence of the anti-SARS-CoV-2 memory B cell response. *Cell*. 184:1201–1213.e14. https://doi.org/10.1016/j.cell.2021.01.050

Starr, T.N., N. Czudnochowski, Z. Liu, F. Zatta, Y.J. Park, A. Addetia, D. Pinto, M. Beltramello, P. Hernandez, A.J. Greaney, et al. 2021. SARS-CoV-2 RBD antibodies that maximize breadth and resistance to escape. *Nature*. 597:97–102. https://doi.org/10.1038/s41586-021-03807-6

Sterlin, D., A. Mathian, M. Miyara, A. Mohr, F. Anna, L. Claër, P. Quentric, J. Fadlallah, H. Devilliers, P. Ghillani, et al. 2021. IgA dominates the early neutralizing antibody response to SARS-CoV-2. *Sci. Transl. Med.* 13: eabd2223. https://doi.org/10.1126/scitranslmed.abd2223

Sun, L., S. Kallolimath, R. Palt, K. Stiasny, P. Mayrhofer, D. Maresch, L. Eidenberger, and H. Steinkellner. 2021. Increased in vitro neutralizing activity of SARS-CoV-2 IgA1 dimers compared to monomers and IgG. *Proc. Natl. Acad. Sci. USA*. 118:e2107148118. https://doi.org/10.1073/pnas.2107148118

Tegally, H., M. Moir, J. Everatt, M. Giovanetti, C. Scheepers, E. Wilkinson, K. Subramoney, S. Moyo, D.G. Amoako, C. Baxter, et al. 2022. *Continued emergence and evolution of omicron in South Africa: New BA.4 and BA.5 lineages*. *MedRxiv*. https://doi.org/10.1101/2022.05.01.22274406 (Preprint posted May 2, 2022)

Ter Meulen, J., E.N. Van Den Brink, L.L.M. Poon, W.E. Marissen, C.S.W. Leung, F. Cox, C.Y. Cheung, A.Q. Bakker, J.A. Bogaards, E. Van Deventer, et al. 2006. Human monoclonal antibody combination against SARS coronavirus: Synergy and coverage of escape mutants. *PLoS Med.* 3:e237. https://doi.org/10.1371/journal.pmed.0030237

Tiller, T., E. Meffre, S. Yurasov, M. Tsuiji, M.C. Nussenzweig, and H. Wardemann. 2008. Efficient generation of monoclonal antibodies from single human B cells by single cell RT-PCR and expression vector cloning. *J. Immunol. Methods*. 329:112–124. https://doi.org/10.1016/j.jim.2007.09.017

Tortorici, M.A., M. Beltramello, F.A. Lempp, D. Pinto, H.V. Dang, L.E. Rosen, M. McCallum, J. Bowen, A. Minola, S. Jaconi, et al. 2020. Ultrapotent human antibodies protect against SARS-CoV-2 challenge via multiple mechanisms. *Science*. 370:950–957. https://doi.org/10.1126/science.abe3354

Vanshylla, K., C. Fan, M. Wunsch, N. Poopalasingam, M. Meijers, C. Kreer, F. Kleipass, D. Ruchnewitz, M.S. Ercanoglu, H. Gruell, et al. 2022. Discovery of ultrapotent broadly neutralizing antibodies from SARS-CoV-2 elite neutralizers. *Cell Host Microbe*. 30:69–82.e10. https://doi.org/10.1016/j.chom.2021.12.010

Walls, A.C., Y.-J. Park, M.A. Tortorici, A. Wall, A.T. McGuire, and D. Veesler. 2020. Structure, function, and antigenicity of the SARS-CoV-2 spike glycoprotein. *Cell*. 183:1735. https://doi.org/10.1016/j.cell.2020.11.032

Wang, L., T. Zhou, Y. Zhang, E.S. Yang, C.A. Schramm, W. Shi, A. Pegu, O.K. Oloniniyi, A.R. Henry, S. Darko, et al. 2021a. Ultrapotent antibodies against diverse and highly transmissible SARS-CoV-2 variants. *Science*. 373:eabh1766. https://doi.org/10.1126/science.abh1766

Wang, Z., J.C.C. Lorenzi, F. Muecksch, S. Finkin, C. Viant, C. Gaebler, M. Cipolla, H.H. Hoffmann, T.Y. Oliveira, D.A. Oren, et al. 2021b. Enhanced SARS-CoV-2 neutralization by dimeric IgA. *Sci. Transl. Med.* 13:eabf1555. https://doi.org/10.1126/scitranslmed.abf1555

Wang, Z., F. Muecksch, D. Schaefer-Babajew, S. Finkin, C. Viant, C. Gaebler, H.-H. Hoffmann, C.O. Barnes, M. Cipolla, V. Ramos, et al. 2021c. Naturally enhanced neutralizing breadth against SARS-CoV-2 one year after infection. *Nature*. 595:426–431. https://doi.org/10.1038/s41586-021-03696-9

Wardemann, H., S. Yurasov, A. Schaefer, J.W. Young, E. Meffre, and M.C. Nussenzweig. 2003. Predominant autoantibody production by early human B cell precursors. *Science*. 301:1374–1377. https://doi.org/10.1126/science.1086907

Wec, A.Z., D. Wrapp, A.S. Herbert, D.P. Maurer, D. Haslwanter, M. Sakharkar, R.K. Jangra, M.E. Dieterle, A. Lilov, D. Huang, et al. 2020. Broad neutralization of SARS-related viruses by human monoclonal antibodies. *Science*. 369:731–736:731. https://doi.org/10.1126/science.abc7424

Westendorf, K., S. Žentelis, L. Wang, D. Foster, P. Vaillancourt, M. Wiggin, E. Lovett, R. van der Lee, J. Hendle, A. Pustilnik, et al. 2022. LY-CoV1404 (bebtelovimab) potently neutralizes SARS-CoV-2 variants. *Cell Rep.* 39: 110812. https://doi.org/10.1016/j.celrep.2022.110812

WHO. 2022. *WHO Coronavirus (COVID-19) Dashboard*. https://covid19.who.int/ (accessed June 6, 2022)

Wibmer, C.K., F. Ayres, T. Hermanus, M. Madzivhandila, P. Kgagudi, B. Oosthuysen, B.E. Lambson, T. de Oliveira, M. Vermeulen, K. van der Berg, et al. 2021. SARS-CoV-2 501Y.V2 escapes neutralization by South African COVID-19 donor plasma. *Nat. Med.* 27:622–625. https://doi.org/10.1038/s41591-021-01285-x

Williams, C.J., J.J. Headd, N.W. Moriarty, M.G. Prisant, L.L. Videau, L.N. Deis, V. Verma, D.A. Keedy, B.J. Hintze, V.B. Chen, et al. 2018. MolProbity: More and better reference data for improved all-atom structure validation. *Protein Sci.* 27:293–315. https://doi.org/10.1002/pro.3330

Winkler, E.S., P. Gilchuk, J. Yu, A.L. Bailey, R.E. Chen, Z. Chong, S.J. Zost, H. Jang, Y. Huang, J.D. Allen, et al. 2021. Human neutralizing antibodies against SARS-CoV-2 require intact Fc effector functions for optimal therapeutic protection. *Cell*. 184:1804–1820.e16. https://doi.org/10.1016/j.cell.2021.02.026

Wrapp, D., N. Wang, K.S. Corbett, J.A. Goldsmith, C.-Lin. Hsieh, O. Abiona, B.S. Graham, and J.S. McLellan. 2020. Cryo-EM structure of the 2019-nCoV spike in the prefusion conformation. *Science*. 367:1260–1263. https://doi.org/10.1126/science.abb2507

Yan, R., Y. Zhang, Y. Li, L. Xia, Y. Guo, and Q. Zhou. 2020. Structural basis for the recognition of the SARS-CoV-2 by full-length human ACE2. *Science*. 367:1444–1448. https://doi.org/10.1126/science.abb2762

Yuan, M., H. Liu, N.C. Wu, C.C.D. Lee, X. Zhu, F. Zhao, D. Huang, W. Yu, Y. Hua, H. Tien, et al. 2020. Structural basis of a shared antibody response to SARS-CoV-2. *Science*. 369:1119–1123. https://doi.org/10.1126/science.abd2321

Yuan, M., D. Huang, C.C.D. Lee, N.C. Wu, A.M. Jackson, X. Zhu, H. Liu, L. Peng, M.J. van Gils, R.W. Sanders, et al. 2021. Structural and functional ramifications of antigenic drift in recent SARS-CoV-2 variants. *Science*. 373:818–823. https://doi.org/10.1126/science.abh1139

Zheng, S.Q., E. Palovcak, J.-P. Armache, K.A. Verba, Y. Cheng, and D.A. Agard. 2017. MotionCor2: Anisotropic correction of beam-induced motion for improved cryo-electron microscopy. *Nat. Methods*. 14:331–332. https://doi.org/10.1038/nmeth.4193

Zhou, D., W. Dejnirattisai, P. Supasa, C. Liu, A.J. Mentzer, H.M.E. Ginn, Y. Zhao, H.M.E. Duyvesteyn, A. Tuekprakhon, R. Nutalai, et al. 2021a. Evidence of escape of SARS-CoV-2 variant B.1.351 from natural and vaccine-induced sera. *Cell*. 184:2348–2361.e6. https://doi.org/10.1016/j.cell.2021.02.037

Zhou, Y., Z. Liu, S. Li, W. Xu, Q. Zhang, I.T. Silva, C. Li, Y. Wu, Q. Jiang, Z. Liu, et al. 2021b. Enhancement versus neutralization by SARS-CoV-2 antibodies from a convalescent donor associates with distinct epitopes on the RBD. *Cell Rep.* 34:108699. https://doi.org/10.1016/j.celrep.2021.108699

Zivanov, J., T. Nakane, B.O. Forsberg, D. Kimanius, W.J. Hagen, E. Lindahl, and S.H. Scheres. 2018. New tools for automated high-resolution cryo-EM structure determination in RELION-3. *Elife*. 7:e42166. https://doi.org/10.7554/eLife.42166

Zost, S.J., P. Gilchuk, R.E. Chen, J.B. Case, J.X. Reidy, A. Trivette, R.S. Nargi, R.E. Sutton, N. Suryadevara, E.C. Chen, et al. 2020a. Rapid isolation and profiling of a diverse panel of human monoclonal antibodies targeting the SARS-CoV-2 spike protein. *Nat. Med.* 26:1422–1427. https://doi.org/10.1038/s41591-020-0998-x

Zost, S.J., P. Gilchuk, J.B. Case, E. Binshtein, R.E. Chen, J.P. Nkolola, A. Schäfer, J.X. Reidy, A. Trivette, R.S. Nargi, et al. 2020b. Potently neutralizing and protective human antibodies against SARS-CoV-2. *Nature*. 584:443–449. https://doi.org/10.1038/s41586-020-2548-6

JEM

Supplemental material

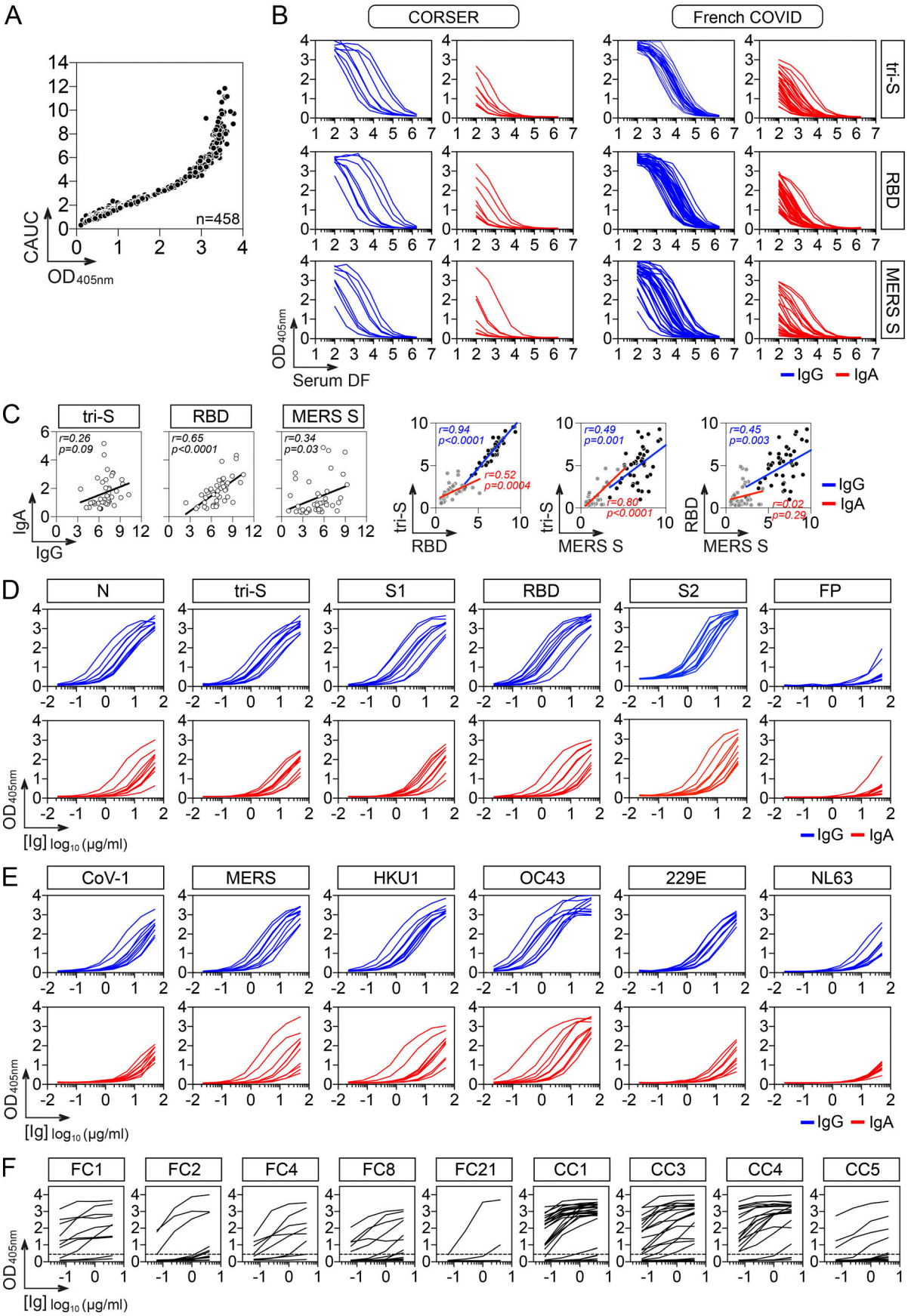

Figure S1. **SARS-CoV-2 reactivity of sera, purified polyclonal and mAbs from COVID-19 convalescents. (A)** Graph comparing the single-dilution OD measurements (1:400; x axis) and AUC values (y axis) measured with serially diluted sera from convalescent COVID-19 individuals in the CORSER (*n* = 212) and French COVID cohorts (*n* = 159), and pre-epidemic donors (*n* = 100) for the ELISA IgG antibody binding to SARS-CoV-2 tri-S as previously reported (Grzelak et al., 2020). **(B)** ELISA graphs showing the reactivity of serum IgG (blue) and IgA (red) antibodies from selected convalescent COVID-19 individuals in the CORSER (*n* = 8) and French COVID (*n* = 34) cohorts against SARS-CoV-2 tri-S and RBD proteins. Samples were also tested against MERS tri-S to assay for cross-reactivity against another β-coronavirus. Means of duplicate values are shown. DF, dilution factor. **(C)** Correlation plots comparing the AUC binding values of serum IgG and IgA antibodies to SARS-CoV-2 tri-S, MERS-CoV tri-S, and RBD proteins as determined in B. P values were calculated using two-tailed Pearson correlation test. **(D)** ELISA graphs showing the reactivity of purified IgG (blue) and IgA (red) serum antibodies from selected donors (*n* = 10) against SARS-CoV-2 protein and protein subunits. Means of duplicate values are shown. **(E)** Same as in D but for tri-S proteins from other coronaviruses. **(F)** ELISA graphs showing the reactivity of antibodies cloned from SARS-CoV-2 S–captured memory B cells (*n* = 133) against the SARS-CoV-2 tri-S protein. Means of duplicate values are shown.

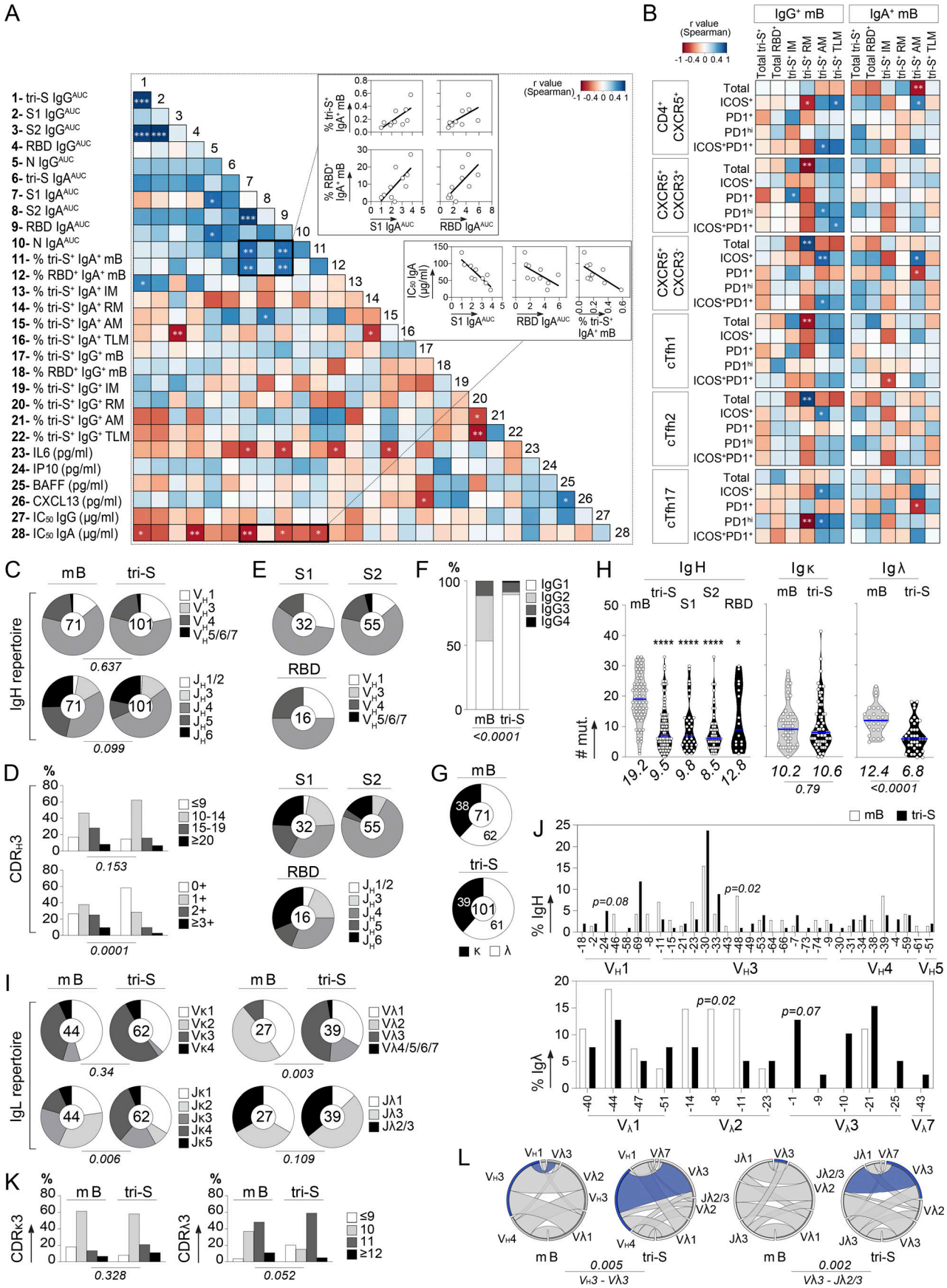

Figure S2. **Humoral immune features of COVID-19 convalescents and SARS-CoV-2 S–specific memory B cells. (A)** Correlograms showing the correlation analyses of the humoral immune parameters measured in COVID-19 convalescents including antibody titers, neutralizing activity, and memory B-cell subset frequencies. For each pair of compared parameters, Spearman correlation coefficients (color coded) with their corresponding P value are shown. ***, P < 0.001; **, P < 0.01; *, P < 0.05. **(B)** Heatmap showing the correlation analyses between the frequency of memory B-cell and cTfh cell subsets (%) measured in COVID-19 convalescents. Cells are color-coded according to the value of Spearman correlation coefficients with the corresponding P values indicated in the center. **, P < 0.01; *, P < 0.05. **(C)** Pie charts comparing the distribution of V_H/J_H gene usage of blood SARS-CoV-2 spike–specific IgG^+/IgA^+ memory B cells and IgG^+ memory B cells from SARS-CoV-2–unexposed healthy individuals (mB; Prigent et al., 2016). The number of antibody sequences analyzed is indicated in the center of each pie chart. Groups were compared using 2 × 5 Fisher's Exact test. **(D)** Bar graph comparing the distribution of CDR_H3 lengths (top) and positive charge numbers (bottom) between blood SARS-CoV-2 spike–specific IgG^+/IgA^+ memory B cells and IgG^+ memory B cells from unexposed individuals (mB; Prigent et al., 2016). Groups were compared using 2 × 5 Fisher's Exact test. **(E)** Same as in C but according to the anti-spike antibody specificity (S1, S2, or RBD). **(F)** Bar graph comparing the distribution of IgG subtypes between blood SARS-CoV-2 spike–specific IgG^+/IgA^+ memory B cells and IgG^+ memory B cells from unexposed individuals (mB; Prigent et al., 2016). Groups were compared using 2 × 5 Fisher's Exact test. **(G)** Pie charts showing the κ- vs. λ-Ig chain usage of blood SARS-CoV-2 spike–specific IgG^+/IgA^+ memory B cells and IgG^+ memory B cells from unexposed individuals (mB; Prigent et al., 2016). Groups were compared using 2 × 2 Fisher's Exact test. **(H)** Violin plots comparing the number of mutations in VH, Vκ, and Vλ genes in SARS-CoV-2 spike–, S1–, S2–, and RBD–specific and control memory B cells. Numbers of mutations were compared across groups of antibodies using the unpaired Student *t* test with Welch's correction. ****, P < 0.0001; *, P < 0.05. **(I)** Same as in C but for Vκ/Jκ and Vλ/Jλ gene usages. **(J)** Bar graphs comparing the distribution of single immunoglobulin genes, V_H (top) and V_L (bottom), expressed by SARS-CoV-2 spike–specific and control IgG^+ memory B cells. Groups were compared using 2 × 2 Fisher's Exact test. **(K)** Same as in D but for CDRκ3 and CDRλ3 lengths. **(L)** Circos plots comparing the $V_H(D_H)J_H$ and V_LJ_L rearrangement frequencies between SARS-CoV-2 spike–specific IgA^+/IgG^+ memory B cells and IgG^+ memory B cells from unexposed individuals (mB; Prigent et al., 2016). Groups were compared using 2 × 5 Fisher's Exact test.

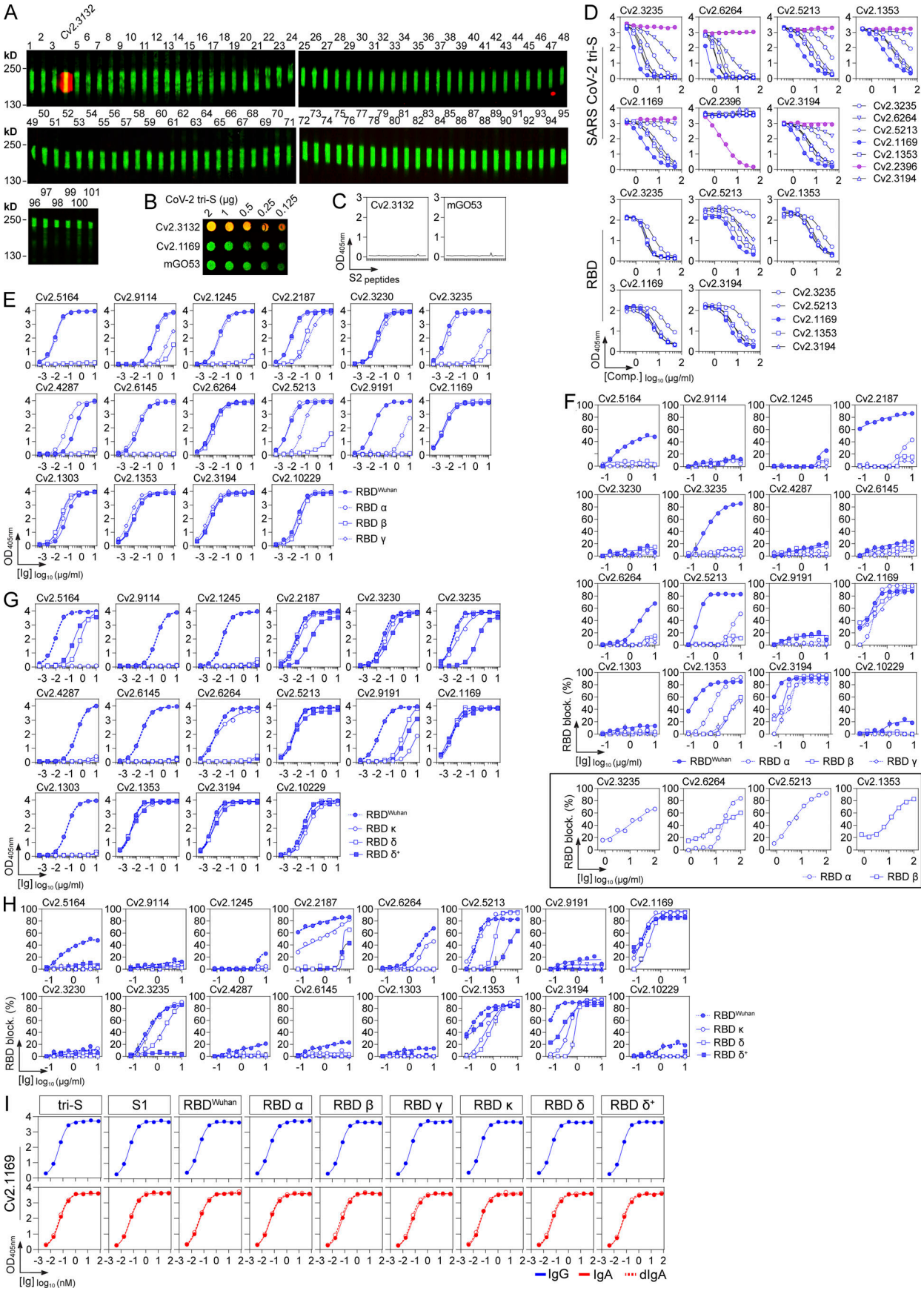

Figure S3. **Binding characteristics of potent anti-RBD antibody neutralizers. (A)** Infrared immunoblot showing the reactivity of SARS-CoV-2 S–specific IgG antibodies (*n* = 101) to denatured SARS-CoV-2 tri-S protein. Immunoreactive green bands correspond to denatured SARS-CoV-2 tri-S protein revealed with an anti-6xHis tag antibody. The red band (yellow when merged) indicates the SARS-CoV-2 antibody Cv2.3132 recognizing denatured tri-S protein. **(B)** Infrared dot blot showing the reactivity of Cv2.3132 antibody to denatured SARS-CoV-2 tri-S at various concentrations. mGO53 is a non–SARS-CoV-2 isotype control. Cv2.1169 was included for comparison. **(C)** Graphs showing the reactivity of Cv2.3132 IgG antibody against 5 amino acid–overlapping 15-mer S2 peptides (*n* = 52). mGO53 is a non–SARS-CoV-2 isotype control. Means ± SD of duplicate values are shown. **(D)** Competition ELISA graphs showing the IgG binding to SARS-CoV-2 tri-S (top) and RBD (bottom) of selected biotinylated SARS-CoV-2 S–specific antibodies in presence of the corresponding non-biotinylated IgG antibodies as potential competitors. Means ± SD of duplicate values are shown. **(E)** ELISA graphs showing the reactivity of SARS-CoV-2 RBD-specific IgG antibodies to RBD proteins from SARS-CoV-2 viral variants α, β, and γ. Means ± SD of duplicate values are shown. **(F)** Competition ELISA graphs showing the binding of biotinylated RBD proteins from SARS-CoV-2 and viral variants (α, β, and γ) to soluble ACE2 ectodomain in presence of SARS-CoV-2 S–specific IgG antibodies as potential competitors. Framed graphs show selected IgG competitors tested at a higher concentration against α and β RBD proteins. Means ± SD of duplicate values are shown. **(G)** Same as in E but for RBD proteins from SARS-CoV-2 viral variants κ, δ, and δ^+. **(H)** Same as in F but for RBD proteins from SARS-CoV-2 viral variants κ, δ, and δ^+. **(I)** ELISA graphs comparing the reactivity of the monomeric IgG/IgA and dimeric IgA (dIgA) antibody forms of Cv2.1169 to SARS-CoV-2 tri-S, S1, and RBD, and to RBD proteins from SARS-CoV-2 viral variants (α, β, γ, δ, δ^+, and κ). Means ± SD of duplicate values are shown.

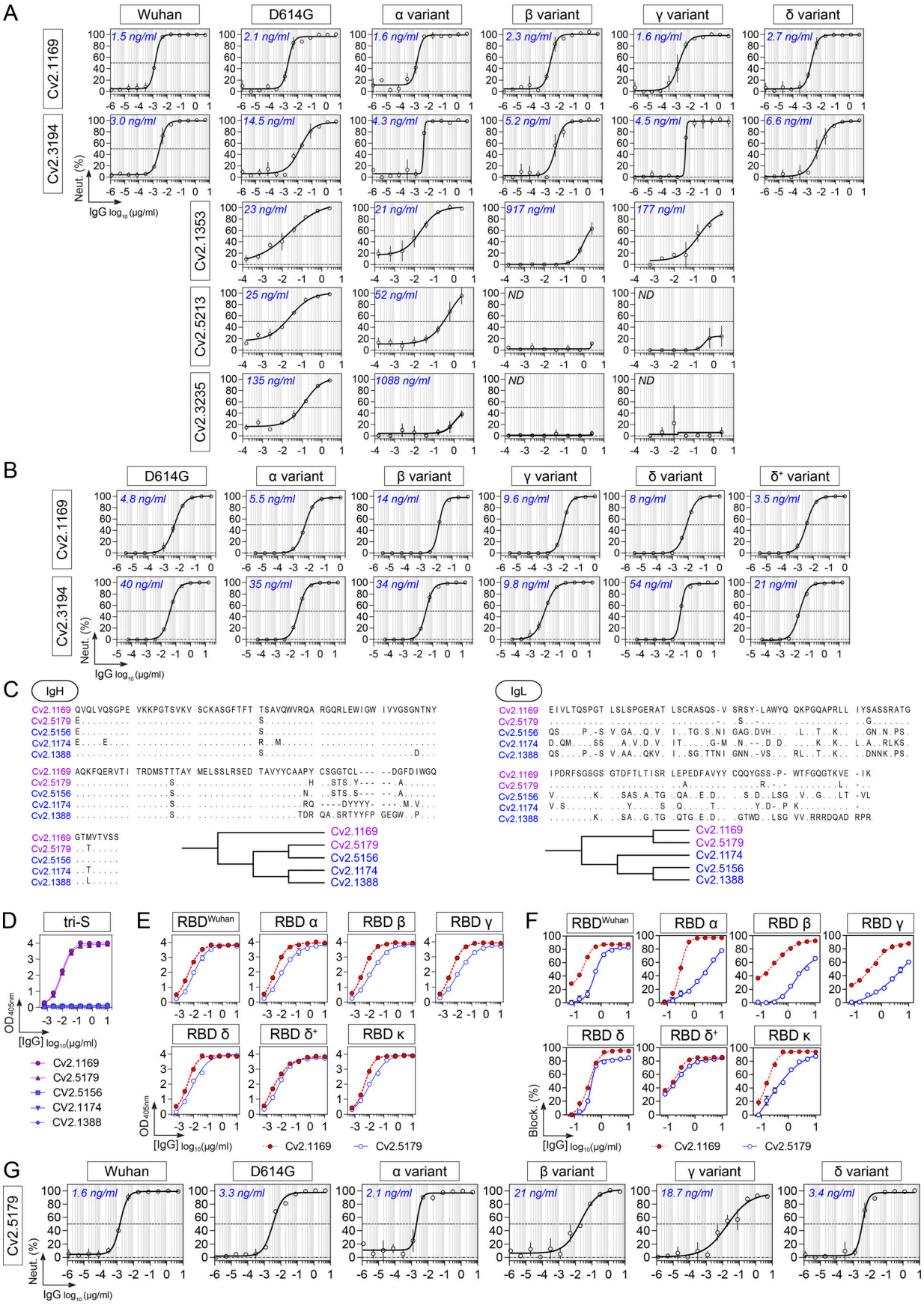

Figure S4. **Cross-neutralizing activity of potent SARS-CoV-2 neutralizers. (A)** Graphs showing the neutralization curves of SARS-CoV-2 and selected VOCs by potent anti-RBD IgG antibodies as determined with the S-Fuse neutralization assay. Error bars indicate the SD of duplicate values. IC_{50} values are indicated in the top left-hand corner (in blue). ND, not determined. **(B)** Graphs showing the neutralization curves of SARS-CoV-2 and selected VOCs by Cv2.1169 and Cv2.3194 IgG antibodies as determined with the pseudo-neutralization assay. Error bars indicate the SD of duplicate values. IC_{50} values are indicated in the top left-hand corner (in blue). **(C)** Amino acid alignment of the heavy chains (IgH, left) and light chains (IgL, right) of the V_H1-58–encoded human antibodies produced from SARS-CoV-2 spike–captured memory B-cell antibodies. Dendrograms showing the relationship between V_H1-58–encoded human antibodies generated from the IgH and IgL sequence alignments are shown at the bottom. **(D)** ELISA graphs showing the reactivity of V_H1-58–encoded antibodies against the SARS-CoV-2 tri-S protein. Means ± SD of duplicate values are shown. **(E)** ELISA graphs comparing the binding of Cv2.5179 and Cv2.1169 antibodies to RBD proteins. Means ± SD of duplicate values are shown. **(F)** Competition ELISA graphs showing the binding of biotinylated SARS-CoV-2 tri-S and RBD proteins to the immobilized soluble ACE2 ectodomain in presence of Cv2.5179 or Cv2.1169 antibody as a competitor. Means ± SD of duplicate values are shown. **(G)** Graphs showing the neutralization curves of SARS-CoV-2 and VOCs by Cv2.5179 IgG antibody as determined with the S-Fuse neutralization assay. Means ± SD of duplicate values are shown. IC_{50} values are indicated in the top left-hand corner (in blue).

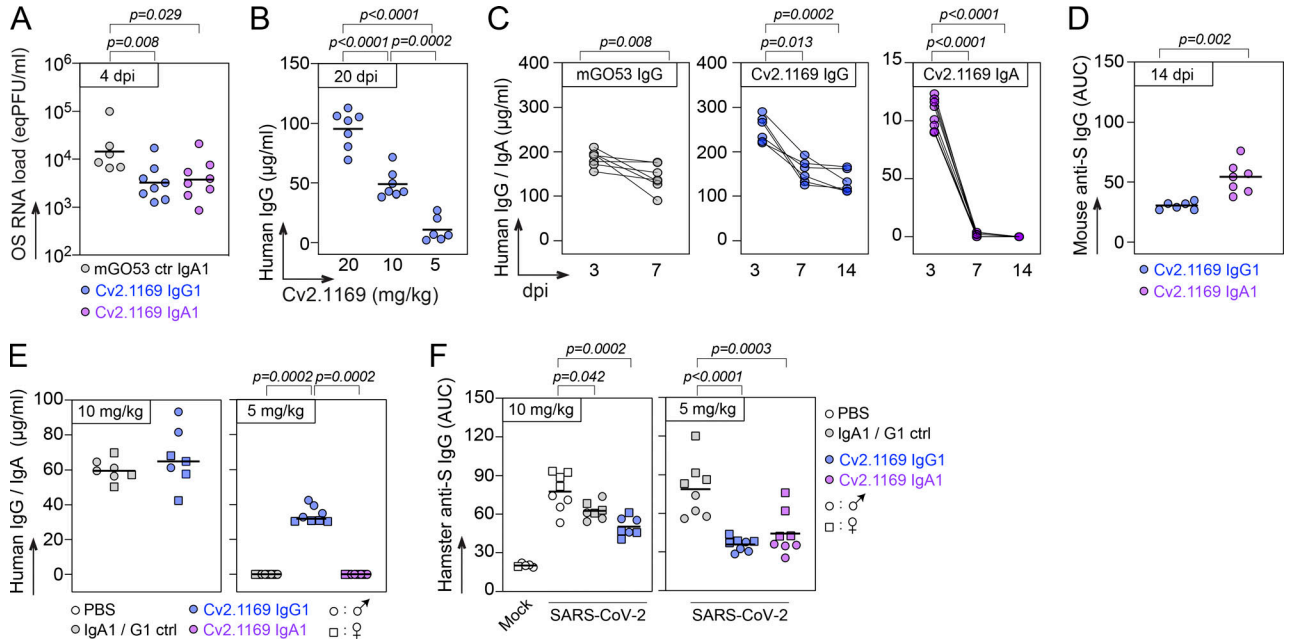

Figure S5. **Cv2.1169 antibody treatment in SARS-CoV-2–infected mice and hamsters. (A)** Dot plot comparing the SARS-CoV-2 RNA levels in the oral swabs (OS) of SARS-CoV-2–infected K18-hACE2 mice (at 4 dpi) treated with 5 mg/kg i.p. of Cv2.1169 IgG or IgA (n = 8/group) or mGO53 control (ctr) IgA antibody (n = 6) as shown in Fig. 10 C. Each dot corresponds to a mouse. Means of duplicate values are shown. **(B)** Dot plot comparing the human IgG concentrations in the serum of SARS-CoV-2–infected K18-hACE2 mice (at 20 dpi) receiving once 5, 10, or 20 mg/kg i.p. of antibody Cv2.1169 (n = 7/group) as shown in Fig. 10, A and C. Each dot corresponds to a mouse. Means of duplicate values are shown. **(C)** Dot plot comparing the human IgG and IgA concentrations in the serum of K18-hACE2 mice infected with the SARS-CoV-2 β variant, and pre-treated (IgA, n = 8) or treated (IgG, n = 6) with Cv2.1169, or with mGO53 IgG control (ctr, n = 7) as shown in Fig. 10 F. Each dot corresponds to a mouse. Means of duplicate values are shown. **(D)** Dot plot showing the ELISA SARS-CoV-2 tri-S binding of serum murine IgG antibodies in K18-hACE2 mice infected with the SARS-CoV-2 β variant, and pre-treated (IgA, n = 8) or treated (IgG, n = 6) with Cv2.1169 as shown in Fig. 10 F. Each dot corresponds to a mouse. Means of duplicate values are shown. **(E)** Dot plot comparing the human IgG and IgA concentrations in the serum of SARS-CoV-2–infected golden Syrian hamsters (at 5 dpi) treated once with Cv2.1169 or mGO53 control (5 mg/kg i.p., n = 8; or 10 mg/kg i.p., n = 7) as shown in Fig. 10, D and E (left and right, respectively). Each symbol corresponds to a mouse. Means of duplicate values are shown. **(F)** Dot plot showing the ELISA SARS-CoV-2 tri-S binding of serum hamster IgG antibodies in SARS-CoV-2–infected hamsters (at 5 dpi) treated once with Cv2.1169 or mGO53 control (5 mg/kg i.p., n = 8; or 10 mg/kg i.p., n = 7) as shown in Fig. 10, D and E (left and right, respectively). Each symbol corresponds to a mouse. Means of duplicate values are shown.

Provided online are Table S1, Table S2, Table S3, Table S4, Table S5, and Data S1. Table S1 provides details on the immunoglobulin gene repertoire, reactivity and antiviral functions of human SARS-CoV-2 spike memory B-cell antibodies cloned from Wuhan SARS-CoV-2 convalescents. Table S2 provides the affinity and neutralization activity values for Cv2.1169 and Cv2.3194 antibodies. Table S3 presents the data collection and refinement statistics of the RBD–Fab crystallized complexes. Table S4 provides the buried surface area at the RBD–antibody interface. Table S5 presents the polar contacts at the RBD–Fab interface for the different crystallized complexes. Data S1 shows cryo-EM data collection and processing of the Cv2.1169-S_6P complex. A micrograph with particles, selected two-dimensional class averages, a local resolution graphic, and a scheme with the steps followed to process the collected data (along with GSFSC resolution plot) are shown for the Cv2.1169-S_6P complex. Mic., micrographs; part., particles.

French COVID Cohort Study Group

Marie Bartoli[1], Alpha Diallo[1], Soizic Le Mestre[1], Christelle Paul[1], Ventzislava Petrov-Sanchez[1], Yazdan Yazdanpanah[1], Cécile Ficko[2], Catherine Chirouze[3], Claire Andrejak[4], Denis Malvy[5], François Goehringer[6], Patrick Rossignol[6], Tristan Gigante[6], Morgane Gilg[6], Bénédicte Rossignol[6], Manuel Etienne[7], Marine Beluze[8], Delphine Bachelet[9], Krishna Bhavsar[9], Lila Bouadma[9], Minerva Cervantes-Gonzalez[9], Anissa Chair[9], Charlotte Charpentier[9], Léo Chenard[9], Camille Couffignal[9], Marie-Pierre Debray[9], Diane Descamps[9], Xavier Duval[9], Philippine Eloy[9], Marina Esposito-Farese[9], Aline-Marie Florence[9], Jade Ghosn[9], Isabelle Hoffmann[9], Ouifiya Kafif[9], Antoine Khalil[9], Nadhem Lafhej[9], Cédric Laouénan[9], Samira Laribi[9], Minh Le[9], Quentin Le Hingrat[9], Sophie Letrou[9], France Mentré[9], Gilles Peytavin[9], Valentine Piquard[9], Carine Roy[9], Marion Schneider[9], Richa Su[9], Coralie Tardivon[9], Jean-François Timsit[9], Sarah Tubiana[9], Benoît Visseaux[9], Dominique Deplanque[10], Jean-Sébastien Hulot[11], Jean-Luc Diehl[11], Olivier Picone[12], François Angoulvant[13], Amal Abrous[14], Sandrine Couffin-Cadiergues[14], Fernanda Dias Da Silva[14], Hélène Esperou[14], Ikram Houas[14], Salma Jaafoura[14], Aurélie Papadopoulos[14], Alexandre Gaymard[15], Bruno Lina[15], Manuel Rosa-Calatrava[15], Céline Dorival[16], Jérémie Guedj[17], Guillaume Lingas[17], Nadège Neant[17], Laurent Abel[18], Victoria Manda[19], Sylvie Behillil[20], Vincent Enouf[20], Yves Levy[21] and Aurélie Wiedemann[21]

[1]Agence Nationale de Recherches sur le Sida et les Hépatites virales-Maladies Infectieuses Émergentes (ANRS-MIE), Paris, France

[2]Hôpital d'Instruction des Armées Bégin, Service des Maladies Infectieuses et Tropicales, Saint-Mandé, France

[3]Centre Hospitalier Régional Universitaire Jean Minjoz, Besançon, France

[4]Centre Hospitalier Universitaire, Amiens, France

[5]Centre Hospitalier Universitaire, Bordeaux, France

[6]Centre Hospitalier Régional Universitaire, Nancy, France

[7]Centre Hospitalier Universitaire, Rouen, France

[8]French Clinical Research Infrastructure Network (F-CRIN), Paris, France

[9]Hôpital Bichat, AP-HP, Paris, France

[10]Hopital Calmette, Lille, France

[11]Hôpital Européen Georges Pompidou, AP-HP, Paris, France

[12]Hôpital Louis Mourier, Colombes, France

[13]Hôpital Necker, AP-HP, Paris, France

[14]Institut National de la Santé et de la Recherche Médicale (INSERM), Paris, France

[15]INSERM UMR 1111, Lyon, France

[16]INSERM UMR 1136, Paris, France

[17]INSERM UMR 1137, Paris, France

[18]INSERM UMR 1163, Paris, France

[19]Hopital Lariboisière, AP-HP, Paris, France

[20]Institut Pasteur, Université Paris Cité, Molecular Genetics of RNA Viruses, Paris, France

[21]Institut de Recherche Vaccinale (VRI), INSERM UMR 955, Créteil, France

CORSER Study Group

Laurence Arowas[1], Blanca Liliana Perlaza[1], Louise Perrin de Facci[1], Sophie Chaouche[1], Linda Sangari[1], Charlotte Renaudat[1], Sandrine Fernandes Pellerin[2], Cassandre van Platen[2], Nathalie Jolly[2], Lucie Kuhmel[3], Valentine Garaud[3], Hantaniaina Rafanoson[3], Soazic Gardais[4], Nathalie de Parseval[5], Claire Dugast[5], Caroline Jannet[5], Sandrine Ropars[5], Fanny Momboisse[5], Isabelle Porteret[5], Isabelle Cailleau[6], Bruno Hoen[6], Laura Tondeur[7], Camille Besombes[7], Arnaud Fontanet[7]

[1]ICAReB platform (Clinical Investigation & Access to Research Bioresources) of the Center for Translational Science, Institut Pasteur, Paris, France

[2]Center for Translational Sciences, Institut Pasteur, Paris, France

[3]Medical Center of the Institut Pasteur, Institut Pasteur, Paris, France

[4]G5 Infectious Disease Epidemiology, Institut Pasteur, Paris, France

[5]Institut Pasteur, Paris, France

[6]Direction de la recherche médicale, Institut Pasteur, Paris, France

[7]Emerging Diseases Epidemiology Unit, Institut Pasteur, Paris, France